



National Library
of Canada

Bibliothèque nationale
du Canada

Canadian Theses Service

Service des thèses canadiennes

Ottawa, Canada
K1A 0N4

NOTICE

The quality of this microform is heavily dependent upon the quality of the original thesis submitted for microfilming. Every effort has been made to ensure the highest quality of reproduction possible.

If pages are missing, contact the university which granted the degree.

Some pages may have indistinct print especially if the original pages were typed with a poor typewriter ribbon or if the university sent us an inferior photocopy.

Reproduction in full or in part of this microform is governed by the Canadian Copyright Act, R.S.C. 1970, c. C-30, and subsequent amendments.

AVIS

La qualité de cette microforme dépend grandement de la qualité de la thèse soumise au microfilmage. Nous avons tout fait pour assurer une qualité supérieure de reproduction.

S'il manque des pages, veuillez communiquer avec l'université qui a conféré le grade.

La qualité d'impression de certaines pages peut laisser à désirer, surtout si les pages originales ont été dactylographiées à l'aide d'un ruban usé ou si l'université nous a fait parvenir une photocopie de qualité inférieure.

La reproduction, même partielle, de cette microforme est soumise à la Loi canadienne sur le droit d'auteur, SRC 1970, c. C-30, et ses amendements subséquents.

UNIVERSITY OF ALBERTA

**THIN FILM MANGANESE SILICIDES: MECHANISMS OF
FORMATION AND OPTICAL PROPERTIES**

by

Lin Zhang



A THESIS

SUBMITTED TO THE FACULTY OF GRADUATE STUDIES AND RESEARCH
IN PARTIAL FULFILLMENT OF THE REQUIREMENTS FOR THE DEGREE
OF MASTER OF SCIENCE

IN

METALLURGICAL ENGINEERING

DEPARTMENT OF MINING, METALLURGICAL AND PETROLEUM
ENGINEERING

EDMONTON, ALBERTA

FALL 1990



**National Library
of Canada**

**Bibliothèque nationale
du Canada**

Canadian Theses Service Service des thèses canadiennes

**Ottawa, Canada
K1A 0N4**

The author has granted an irrevocable non-exclusive licence allowing the National Library of Canada to reproduce, loan, distribute or sell copies of his/her thesis by any means and in any form or format, making this thesis available to interested persons.

The author retains ownership of the copyright in his/her thesis. Neither the thesis nor substantial extracts from it may be printed or otherwise reproduced without his/her permission.

L'auteur a accordé une licence irrévocable et non exclusive permettant à la Bibliothèque nationale du Canada de reproduire, prêter, distribuer ou vendre des copies de sa thèse de quelque manière et sous quelque forme que ce soit pour mettre des exemplaires de cette thèse à la disposition des personnes intéressées.

L'auteur conserve la propriété du droit d'auteur qui protège sa thèse. Ni la thèse ni des extraits substantiels de celle-ci ne doivent être imprimés ou autrement reproduits sans son autorisation.

ISBN 0-315-65068-0

UNIVERSITY OF ALBERTA

RELEASE FORM

NAME OF AUTHOR: Lin Zhang
TITLE OF THESIS: **THIN FILM MANGANESE SILICIDES:
MECHANISMS OF FORMATION AND
OPTICAL PROPERTIES**

DEGREE: Master of Science

YEAR THIS DEGREE GRANTED: Fall 1990

PERMISSION IS HEREBY GRANTED TO THE UNIVERSITY OF ALBERTA LIBRARY TO PRODUCE SINGLE COPIES OF THIS THESIS AND TO LEND OR SELL SUCH COPIES FOR PRIVATE, SCHOLARLY OR SCIENTIFIC RESEARCH PURPOSES ONLY.

THE AUTHOR RESERVES OTHER PUBLICATION RIGHTS, AND NEITHER THE THESIS NOR EXTENSIVE EXTRACTS FROM IT MAY BE PRINTED OR OTHERWISE REPRODUCED WITHOUT THE AUTHOR'S WRITTEN PERMISSION.

(SIGNED) Zhang, L.

PERMANENT ADDRESS:

C/O. Mr. Jian Xin


Building 5-2-403, Tuanjiehu Beitoufiao

Beijing, P. R. China

DATE: Aug. 30, 1990

UNIVERSITY OF ALBERTA
FACULTY OF GRADUATE STUDIES AND RESEARCH

THE UNDERSIGNED CERTIFY THEY HAVE READ, AND RECOMMEND TO THE
FACULTY OF GRADUATE STUDIES AND RESEARCH FOR ACCEPTANCE, A
THESIS ENTITLED, **THIN FILM MANGANESE SILICIDES:
MECHANISMS OF FORMATION AND OPTICAL PROPERTIES**
SUBMITTED BY LIN ZHANG
IN PARTIAL FULFILLMENT OF THE REQUIREMENTS FOR THE
DEGREE OF MASTER OF SCIENCE
IN METALLURGICAL ENGINEERING.



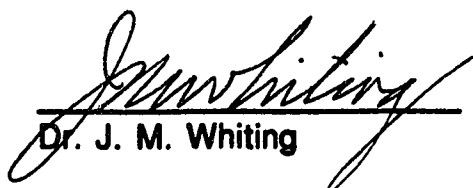
Dr. D. G. Ivey
Supervisor



Dr. M. L. Wayman



Dr. M. J. Brett



Dr. J. M. Whiting

Date: Aug. 30, 1990

ABSTRACT

Manganese silicide formation, by thermal reaction of Mn/Si thin film couples, has been systematically studied. Mn films (300 nm thick) were deposited onto <100> oriented single crystal Si substrates by thermal evaporation under a vacuum of 2×10^{-6} Torr. The as-deposited samples were annealed in a quartz tube furnace with flowing nitrogen at 380 to 570°C for different periods. The samples were examined by transmission electron microscopy (TEM), scanning transmission electron microscopy (with energy dispersive x-ray spectroscopy), and x-ray diffraction.

Three phases, i.e. Mn_3Si , Mn_5Si_3 , and MnSi , were formed through a layered growth process during low temperature annealing (380 to 430°C). The formation sequence for these silicides was Mn_3Si , MnSi , and then Mn_5Si_3 . The unusual phenomena of coexistence of these three phases and simultaneous growth of two phases (MnSi and Mn_5Si_3) were also observed. It was found that diffusion fluxes of Mn and Si in the silicides decreased with increasing annealing time, but the Mn flux decreased much faster than that of Si. These results, suggested a model for manganese silicide formation which could explain the formation sequence and the unusual phenomena quite well.

Two phases, i.e. MnSi and $\text{MnSi}_{1.73}$, were formed during high temperature annealing (485 to 570°C). $\text{MnSi}_{1.73}$ formed by an island growth process and this could be well explained by nucleation controlled theory.

A band gap value for $\text{MnSi}_{1.73}$ was optically determined using a spectrophotometer and a sample with a single $\text{MnSi}_{1.73}$ layer on a Si substrate. The determined value was between 0.78 and 0.83 eV.

ACKNOWLEDGEMENTS

I am deeply grateful to Dr. D. G. Ivey for his supervision, guidance, and encouragement extended throughout the course of this study. I am also indebted to Dr. M. J. Brett for his continued and valuable help and advice during the study of optical properties. Many thanks are also due to Dr. M. L. Wayman for his valuable comments on the model of manganese silicide formation.

I especially thank Mr. Barry Arnold who kindly made all the manganese thin film depositions for this study; Mr. Graham McKinnon, Mr. Ken Westra, and Mr. Alan Mitchell who ran the spectrophotometer for all optical property measurements; Dr. Saul Sheinin and Mr. John Malinski who provided access to an ion mill for TEM specimen preparation, and Dr. Maria Neuwirth of the Alberta Environmental Centre who provided access to a TEM/STEM.

I also wish to thank Ms. Tina Barker, Mr. Shiraz Merali and Mr. Bob Konzuk for their help in obtaining supplies, and Mr. Rob Stefaniuk for his help in computer related problems.

I am also grateful to the Natural Sciences and Engineering Research Council of Canada for the financial assistance which made this study possible.

TABLE OF CONTENTS

CHAPTER	PAGE
1. INTRODUCTION	1
2. LITERATURE REVIEW	4
2.1. Overview of Research on Transition Metal Silicides	4
2.2. Crystal Structures and Properties of Manganese Silicides	6
2.2.1. Crystal Structures of Manganese Silicides	6
2.2.2. Electrical Properties of Manganese Silicides	7
2.2.3. Band Gap Energy of $\text{MnSi}_{1.73}$	7
2.2.4. Thermodynamic Properties of Manganese Silicides	8
2.3. Kinetics and Mechanisms of Formation for Transition	9
2.3.1. General Character of Transition Metal Silicide Formation	9
2.3.1.1. Single Phase Growth in Thin-Film Couples	9
2.3.1.2. Formation Sequence of Silicides in Thin-Film Couples	11
2.3.1.3. Silicide Formation Temperatures	11
2.3.2. Other Experimental Phenomena Related to Transition Metal Silicide Formation	12
2.3.2.1. Competitive Growth	13
2.3.2.2. Silicide Formation in Lateral Diffusion Couples	14
2.3.2.3. Diffusion in Thin-Film Couples	15
2.3.2.4. Impurity Effects	16
2.3.2.5. Alloy Thin-Film Couples	17

2.3.3. Kinetics of Silicide Formation.....	18
2.3.3.1. Diffusion Controlled and Interface Reaction Controlled Processes.....	19
2.3.3.2. Nucleation Controlled Processes.....	25
2.3.4. Theories And Models For Growth Sequence During Silicide Formation.....	28
2.3.4.1. Kinetics Of Layered Growth In Bulk Couples	28
2.3.4.2. Theory for Predicting the Growth Sequence of Silicide Formation.....	32
2.3.4.3. Theory of Single Phase Growth in Thin-Film Couples.....	35
2.3.4.4. Model of Growth Sequence Determined by Interfacial Composition.....	39
3. EXPERIMENTAL METHODS	69
3.1. Deposition of Manganese Films	69
3.2. Annealing Procedure.....	69
3.3. X-Ray Diffraction Experiments	70
3.3.1. Equipment	70
3.3.2. Phase Identification	70
3.3.3. Monitoring Silicide Growth.....	71
3.4. Transmission Electron Microscopy (TEM) and Scanning Transmission Electron Microscopy (STEM).....	72
3.4.1. Specimen Preparation	72
3.4.2. Thickness Measurement Using Micrographs.....	73
3.4.3. Phase Identification	74
3.4.3.1. Convergent Beam Electron Diffraction.....	74
3.4.3.2. Energy Dispersive X-ray Spectroscopy (EDX).....	76

3.5. Optical Property Measurements.....	77
4. RESULTS	80
4.1. Interfacial Oxide.....	80
4.2. Anneal Reactions.....	81
4.2.1. Phase Identification	81
4.2.2. Formation Sequence and Growth Kinetics of Silicides at Low Temperatures	81
4.2.3. Growth Process of MnSi _{1.73} at High Temperatures	84
4.3. Calculation of Thermodynamic Quantities.....	85
4.4. Diffusion In Manganese Silicides	87
4.4.1. Determination of Major Diffusers	87
4.4.2. Changes in Diffusion Fluxes	88
4.5. Determination of Band Gap Value	90
5. DISCUSSION.....	127
5.1. Mechanisms Of Manganese Silicide Formation	127
5.2. Explanation of The Formation Sequence of Manganese Silicides	131
5.3. Comparison of Models.....	138
5.4. Explanation for Nucleation Controlled Process.....	142
6. CONCLUSIONS AND RECOMMENDATIONS.....	150
6.1. Conclusions	150
6.2. Recommendations.....	151
BIBLIOGRAPHY	153
Appendix 1. X-Ray Diffraction File Used to Identify Silicide Phases	159
Appendix 2. Procedure for Specimen Preparation	161

Appendix 3. Derivation of Equations for Evaluating Optical	
Constants.....	163
A.3.1. Modification of Brett's Model.....	163
A.3.2. Derivation of Equations 4-15, 4-16, and 4-17.....	165
Appendix 4. BASIC Program for Calculation of Optical	
Constants.....	168

LIST OF TABLES

TABLE	PAGE
2-1. Tabulation of Transition Metals and Their Silicides.....	45
2-2. Si-Rich Silicides and Their Properties.....	46
2-3. Crystallographic Data for Manganese Silicides	47
2-4. Schottky Barrier Height for Manganese Silicides	47
2-5. Electrical Resistivities of Manganese Silicides	48
2-6. Semiconductor Properties of $\text{MnSi}_{1.73}$	49
2-7a. Melting Point for Manganese Silicides.....	50
2-7b. Thermodynamic Data of Manganese Silicides	50
2-8. Formation Sequence of Transition Metal Silicides	51
2-9. Major Diffusers in Thin Silicide Films	53
2-10. Growth Kinetics of Transition Metal Silicides.....	54
2-11. Summary of Gösele and Tu's Analysis	55
3-1. Annealing Regimes	78
4-1. List for Composition Analysis of Manganese Silicides.....	95
4-2. Thickness of Silicides in Samples.....	95
4-3. X-Ray Diffracted Intensities from MnSi	96
4-4. X-Ray Diffracted Intensities from MnSi and $\text{MnSi}_{1.73}$	96
4-5. Reaction Equations and Standard Free Energy for Silicide Formation at 380°C	97
4-6. Calculations of Standard Free Energy for Mn_5Si_3 Formation.....	97
4-7. The Number of Atoms in Silicide Phases	98
4-8. Average Fluxes of Mn and Si in Diffusion Region.....	100

LIST OF FIGURES

FIGURE	PAGE
2-1. Binary Mn-Si Phase Diagram.....	56
2-2. Sketch of the Mn and Si Atoms Within One-Half a Unit Cell of $Mn_{15}Si_{26}$	57
2-3. Plot of Resistivity vs Temperature for $MnSi_{1.73}$	57
2-4a. Schematic of Formation Sequence of Nickel Silicides.....	58
2-4b. Binary Ni-Si Phase Diagram.....	58
2-5. Schematic of the Coverage Evolution of the Reacted Overlayer for Ti and Sc Metals on Si Substrate.	59
2-6. Schematic View of Competitive Growth.....	59
2-7. Plot of Growth Sequence in Ni-Si Lateral Diffusion Couples.....	60
2-8. Schematic View of Multiple Phase Growth in a Thin Film Couple with Relatively Thick Metal Film on Si Substrate.....	60
2-9a. Effect of Oxygen on the Formation of Platinum Silicide.....	61
2-9b. Effect of Oxygen on the Formation of Molybdenum Silicide.....	61
2-10. Schematic of Thin Film Reactions with Alloy Film on Si Substrate	62
2-11. Schematic Diagram Showing Different Growth Processes.....	62
2-12. Tu and Gösele's Diffusion Model.....	63
2-13. Schematic Binary Phase Diagram and Concentration Profile of Element A in a Bulk Diffusion Couple.....	64

2-14. Concentration Profile of A Atoms in Tu and Gösele's Competitive Growth Model.....	65
2-15. Schematic Summary of Gösele and Tu's Model.....	66
2-16. Schematic Thermodynamic Explanation for Ottaviani's Model.....	67
2-17. Schematic of Different Growth Processes in Bulk Diffusion Couple and Thin-Film Couple.....	68
3-1. A Sample X-Ray Diffraction Pattern from $\text{MnSi}_{1.73}$	79
4-1. TEM Micrograph of a Cross-Section Specimen Made from As-Deposited Sample.....	101
4-2a. TEM Micrograph of a Plan View Specimen Made from As-Deposited Sample.....	102
4-2b. SAD Pattern from Plan View Specimen.....	102
4-3. TEM Micrograph of a Cross-Section Specimen Annealed at 380°C for 10 min.....	103
4-4. TEM Micrograph of a Plan View Specimen Annealed at 380°C for 10 min.....	104
4-5. TEM Micrograph of a Cross-Section Specimen Annealed at 430°C for 30 min.....	105
4-6. Showing the Method used for Phase Identification in Cross-Section Specimens.....	106
4-7a. Indexed CBED Pattern from Mn_3Si	107
4-7b. Indexed CBED Pattern from Mn_5Si_3	108
4-7c. Indexed CBED Pattern from MnSi	109
4-7d. Indexed CBED Pattern from $\text{MnSi}_{1.73}$	110
4-8a and b. Formation Sequence of Manganese Silicides at 380°C	111

4-8c and d. Formation Sequence of Manganese Silicides at 380°C	112
4-9. Formation Sequence of Manganese Silicides at 430°C.....	113
4-10. Summary of Formation Sequence of Manganese Silicides.....	114
4-11a. Plot of Thickness of MnSi vs. (Annealing Time) ^{1/2}	115
4-11b. Plot of Thickness of MnSi vs. Annealing Time.....	115
4-12a. Plot of X-Ray Diffraction Intensity from MnSi vs. (Annealing Time) ^{1/2}	116
4-12b. Plot of X-Ray Diffraction Intensity from MnSi vs. Annealing Time.....	116
4-13. TEM Micrograph Showing Island Growth of MnSi _{1.73}	117
4-14. Schematic Process of MnSi _{1.73} Nucleation and Growth.....	118
4-15. Micrograph Showing MnSi/Si Interface.....	119
4-16. Micrographs Showing the Shapes of Interfaces.....	120
4-17. Micrograph Showing Growth Protrusions.....	121
4-18. Change in Average Diffusion Fluxes	122
4-19. Schematic Configuration Used in Optical Property Measurements.....	123
4-20a. Plot of Percent Reflectance vs. Photon Energy	124
4-20b. Plot of Percent Transmittance vs. Photon Energy.....	124
4-21a. Plot of Extinction Coefficient of MnSi _{1.73} vs. Photon Energy.....	125
4-21b. Plot of Refractive Index of MnSi _{1.73} vs. Photon Energy.....	125
4-22. Plot for Determination of Band Gap Value.....	126
5-1. Schematic Model for Manganese Silicide Formation.....	145
5-2. Stage I of Manganese Silicide Formation.....	145

5-3. Stage II of Manganese Silicide Formation.....	146
5-4. Stage III of Manganese Silicide Formation.....	147
5-5. Stage IV of Manganese Silicide Formation.....	149
A-1. Schematic Procedure for Preparing Cross-Section TEM Specimens.....	171
A-2a. Schematic Accounting for Energy Flow in Brett's Model.....	173
A-2b. Schematic Accounting for Energy Flow in MnSi _{1.73} /Si System.....	174
A-3. Accounting of Energy Flow when Multiple Reflection Takes Place in a Si Wafer.....	175
A-4a. Plot of Refractive Index of Si Wafer vs. Photon Energy.....	176
A-4b. Plot of Extinction Coefficient of Si Wafer vs. Photon Energy.....	176

Chapter 1. INTRODUCTION

Manganese silicides, like most silicides, were initially investigated as refractory materials [1-5]. The documented results, from earlier studies, included the thermodynamic properties [1, 5] and crystallographic data for these silicides [1, 3, 4]. About twenty years ago, the tremendous potential of transition metal silicides in electronic applications was discovered. Since then transition metal-silicon thin film systems have been investigated extensively, with emphasis placed on the utilization of metal silicides in integrated circuit applications, such as contacts, interconnects, gates, etc.

The properties of manganese silicides have been examined as well, although somewhat less extensively than other silicides [6-15]. A unique property of one of the manganese silicides, i.e. $\text{MnSi}_{1.73}$, discovered in the mid 1970's, is that it is a semiconductor [11, 12, 15]. Initially, the main consideration for the application of $\text{MnSi}_{1.73}$ was aimed at its large thermoelectric power [11, 12]. Initial measurements of the band gap were inconclusive, indicating a value ranging from 0.4-0.9 eV [11, 12, 15]. The most recent band gap measurements were made in 1987, by Bost and Mahan [16], using samples with polycrystalline $\text{MnSi}_{1.73}$ films on Si substrates. Their results showed that this material had a direct band gap with a value of 0.68 eV. If $\text{MnSi}_{1.73}$ is indeed a direct band gap semiconductor and if it can be epitaxially grown on Si, then it has promise for Si compatible optoelectronic applications such as components in optic fibre links and infrared detector arrays [16]. Thus, it is meaningful

to try and grow $\text{MnSi}_{1.73}$ epitaxially on Si and to determine its band gap energy.

In order to obtain epitaxial $\text{MnSi}_{1.73}$ on Si, a comprehensive understanding of the formation processes and growth kinetics for manganese silicides is necessary. Unfortunately, very little in this area is known at this time. The only documented systematic investigation of manganese silicide formation, using thin film couples, is that reported by Eizenberg and Tu [6]. They observed that two phases, MnSi and $\text{MnSi}_{1.73}$, were formed. MnSi growth started at 400°C and followed a layered growth process, while $\text{MnSi}_{1.73}$ began to nucleate only at temperatures higher than 500°C forming through an island growth process [6]. Because the techniques, i.e. x-ray diffraction and Rutherford backscattering (XRD and RBS), for Eizenberg and Tu's kinetic study have an in-depth resolution of 10 to 20 nm, some phases with thicknesses less than the resolution may not have been detected. As a result, there still is uncertainty concerning the formation process and the growth kinetics. Recently, a powerful analytical tool, cross-sectional transmission electron microscopy (TEM), which makes the identification of phases as thin as 1 to 2 nm possible, has been developed for thin film reaction studies. Thus far, this technique has proven to be successful in studying silicide formation processes and kinetics. Cross-sectional TEM can, therefore, be applied to the study of manganese silicide formation.

The objectives of this thesis are summarized below:

- 1) To use cross-sectional TEM, combined with x-ray diffraction, to monitor closely the growth process of manganese

silicides and to determine the formation sequence for these silicides.

2) To explore the mechanism of manganese silicide formation.

3) To grow single layer $\text{MnSi}_{1.73}$ films on Si and determine the band gap value by optical property measurement, to confirm the semiconducting behaviour of $\text{MnSi}_{1.73}$.

The main body of the thesis begins with a comprehensive literature review, which includes a brief summary of the properties and structures of manganese silicides and a comprehensive survey of published experimental results and theories of silicide formation in various transition metal/Si thin film couple systems. The experimental section outlines procedures used to deposit Mn on Si, react Mn with Si and characterize the reaction products. The results obtained are then discussed, with models proposed to explain the growth processes.

Chapter 2. LITERATURE REVIEW

2.1. Overview of Research on Transition Metal Silicides

During the last two decades, transition metal silicides have attracted tremendous interest and attention from scientists around the world. Some of these silicides have been widely used in very large scale integrated circuit (VLSI) technology because they have many advantages over other materials, and because they are compatible with existing Si integrated circuit technology. Many papers have been contributed to this area. These investigations can be grouped into the following major categories:

- a) Studies aimed at understanding the physical properties of the silicides in terms of the electronic and crystal structure of the elements and compounds [1, 2, 17].
- b) Studies aimed at understanding the kinetics and mechanisms of silicide formation [1, 2, 18-27].
- c) Studies of silicides as Schottky barriers and ohmic contacts [1, 2, 6, 28].
- d) Studies of silicides as low-resistivity metallizations for gates and interconnects [1, 2, 29-33].
- e) Studies of potential applications of semiconducting silicides in optoelectronic devices [16, 34-36].

The transition metal silicide family is listed in Table 2-1. Among them, Si-rich silicides are mainly of interest. This is because most of the silicides which have been used in VLSI circuits and will probably be used in other electronic devices are formed by

reacting a thin metal film with silicon substrates. At present device processing temperatures, Si-rich silicides are the most stable silicides. In Table 2-2, these silicides are listed in three groups, depending on their general properties and applications. The three groups are noble metal silicides, refractory metal silicides, and semiconducting silicides, respectively.

Of these three groups, the first two have been extensively investigated. Silicides in the first group have been used to make both ohmic and Schottky barrier contacts, while silicides in second group, such as TiSi_2 , TaSi_2 , and WSi_2 etc., have been used to make gate metallizations and interconnects in VLSI circuits. On the other hand, research on the applications of the semiconducting silicides is still very limited. Very little is known about the physical properties and the formation kinetics of these silicides (points a) and b) above). Recently, several papers [16, 34-36] concerning semiconducting silicides have been published. These semiconducting silicides are reported to be direct band gap semiconductors, making them attractive for optoelectronic applications as well as being compatible with existing Si integrated circuit technology. Therefore, these materials are very promising for applications in new optoelectronic devices.

Semiconducting manganese silicide i.e., $\text{MnSi}_{1.73}$, is the topic of this investigation. Very little information about this silicide is available and studies concerning the kinetics and mechanisms of manganese silicide formations have yet to be done, hence the rest of the literature review will concentrate on the following:

1) The crystal structures and properties of manganese silicides.

2) The kinetics and mechanisms of transition metal silicide formation.

2.2. Crystal Structures and Properties of Manganese Silicides

2.2.1. Crystal Structures of Manganese Silicides

A binary phase diagram of the Mn-Si system [7] is shown in Fig. 2-1. The stable manganese silicides are all shown, i.e., Mn_6Si , Mn_9Si_2 , Mn_3Si , Mn_5Si_2 , Mn_5Si_3 , MnSi , and $\text{Mn}_{11}\text{Si}_{19}$ (i.e. $\text{MnSi}_{1.73}$). Table 2-3 lists known crystallographic data for these silicides.

$\text{MnSi}_{1.73}$ has a quite complicated structure. So far, it has been reported as Mn_4Si_7 [8], $\text{Mn}_{11}\text{Si}_{19}$ [3], $\text{Mn}_{15}\text{Si}_{26}$ [4], and $\text{Mn}_{27}\text{Si}_{47}$ [9]. According to Ye and Amelinckx [10], this is because the material is a one-dimensional doubly periodic crystal, i.e. a crystal in which the sublattices of the two constituents have different periods along one common direction while the other two lattice parameters are equal. The manganese atoms form a β -tin like arrangement with a tetragonal subcell ($a=0.552$ nm; $c_{\text{Mn}}=0.437$ nm) (Fig. 2-2a). The silicon atoms adopt a double helical arrangement (Fig. 2-2b), with a period equal to the pitch of this helix, i.e. $c_{\text{Si}} \cong 4c_{\text{Mn}}$, filling the interstices left in the Mn sublattice. The resulting, approximately rationalized, c-period is the smallest common multiple of c_{Mn} and

c_{Si} . At the present time, what causes the changes in c_{Mn} or c_{Si} is still unknown.

2.2.2. Electrical Properties of Manganese Silicides

The electrical properties of some manganese silicides have been investigated by different groups [1, 6, 11-15]. The Schottky barrier height, ϕ_{B0} , for MnSi and MnSi_{1.73} on n-type silicon substrates have been determined [6, 14], and are listed in Table 2-4.

Electrical resistivities of manganese silicides at room temperature are listed in Table 2-5. From this table, it can be seen that although other manganese silicides show a metallic nature, MnSi_{1.73} may have a semiconductor nature. This semiconductor nature of MnSi_{1.73} has been established by past investigations [11-13, 15] of the electrical transport properties of both bulk and thin film samples. Fig. 2-3 shows the electrical resistivity ρ as a function of temperature for a thin film MnSi_{1.73} sample, which was reported by Krontiras et al [13]. The electron and hole concentrations (n , p) and Hall coefficient (R_H) for MnSi_{1.73} in the intrinsic region have been reported by different groups (Table 2-6).

According to Krontiras et al [13], the electron to hole mobility ratio of MnSi_{1.73} is about 0.36. This indicates that MnSi_{1.73} is a p-type semiconductor.

2.2.3. Band Gap Energy of MnSi_{1.73}

The band gap energy of MnSi_{1.73} can be evaluated from experimental data using the following formula:

$$\rho = \rho_0 \exp\left(-\frac{E_g}{2kT}\right) \quad (2-1);$$

where ρ is the electrical resistivity of this material, ρ_0 is a preexponential constant, E_g is the band gap energy, k is Boltzmann's constant, and T is the temperature. By this method, Nishida [12], Kawasumi and Sakata [11], and Samsonov [15] calculated the band gap value for bulk samples, and their values were 0.4, 0.703, and 0.9 eV respectively. Kroutiras et al [13] have also evaluated band gap values of 0.45 and 0.42 eV from both resistivity and Hall effect data. Recently, Bost and Mahan [16] have determined a band gap value of 0.68 eV by optical measurement. These authors [16] also pointed out that it was quite likely that MnSi_{1.73} has a direct band gap.

2.2.4. Thermodynamic Properties of Manganese Silicides

Available thermodynamic data for manganese silicides are listed in Table 2-7 [5].

2.3. Kinetics and Mechanisms of Formation for Transition Metal Silicides

2.3.1. General Character of Transition Metal Silicide Formation

Transition metal silicides are usually formed by reacting thin metal films with Si substrates [1, 2, 18, 20, 22-26]. This configuration, with a several hundred nm thick metal film on a Si substrate, could be considered as a thin film binary diffusion couple [25, 37]. It has been found that there are significant differences in silicide formations between thin-film couples and bulk couples (both components thicker than 1mm). Three important features of silicide formations in thin-film couples are single phase growth, special formation sequence, and very low reaction temperatures [22]. These features will be discussed below.

2.3.1.1. Single Phase Growth in Thin-Film Couples

As is well known, in a bulk couple, all the phases predicted by the equilibrium phase diagram will be observed to grow simultaneously, apart from some exceptional absences of individual compounds [38-41]. However, in a thin film couple, these phases tend to form sequentially, i.e. they grow one by one, instead of several or all of them growing together as in bulk couples. Moreover, some phases which can be observed in bulk couples do not show up in thin film couples [22, 25, 37, 42-44]. Because of different growth behaviour, the growth process in a bulk couple is

referred to as multiple phase growth and the growth process in a thin-film couple is called single phase growth [22, 25].

One typical example for single phase growth is the reaction of thin-film Ni with a Si substrate. According to experimental observations [20, 22, 25, 42, 43] (Fig. 2-4a), the first phase formed between the metal and Si is Ni_2Si . Ni_2Si grows until all the Ni is exhausted. The second phase, NiSi , begins to form and grow by consuming Ni_2Si , until all the Ni_2Si completely disappears. The last phase, NiSi_2 , is formed at even higher temperatures. The binary phase diagram for the Ni-Si system is shown in Fig. 2-4b. Comparing Fig. 2-4a with Fig. 2-4b, it is evident that one phase, i.e. Ni_3Si_2 , which exhibits the most extensive growth in bulk couples [43, 45], is absent.

There have been some doubts about the validity of single phase growth. These doubts have arisen because most of the thin-film single phase growth studies have been performed by XRD and RBS. Both techniques have an in-depth resolution of 10 to 20 nm. These techniques would not be able to resolve phases with layer thicknesses less than 10 nm. For this reason, cross-sectional TEM techniques have been applied to the study of the layered morphology of silicides and their planar interfaces (for example, CrSi_2 [46, 47] and RhSi [48]). Furthermore, high resolution electron microscopy (with 0.3 nm resolution) has also been used in the observation of NiSi_2/Si , NiSi/Si , and $\text{Pd}_2\text{Si}/\text{Si}$ interfaces (NiSi_2 , NiSi , and Pd_2Si were epitaxially grown on Si substrates) [43, 49, 50]. No other phases were found at these interfaces. Therefore, it is believed that

single phase growth is a general nature of silicide formation in thin-film couples.

2.3.1.2. Formation Sequence of Silicides in Thin-Film Couples

It has been found that the growth of silicides in thin-film couples follows special formation sequences, which depend on the type of silicides and the relevant amount of the two components in the thin-film couples [1, 20, 22, 24, 25]. Table 2-8 lists documented formation sequences for each family of transition metal silicides. The results in Table 2-8a have been obtained from the configuration of diffusion couples with thin metal films on silicon substrates and the results in Table 2-8b have been obtained from diffusion couples with thin Si films on metal substrates. For each family, the silicides are listed in order of their appearance during the annealing process, as indicated by the formation temperatures.

2.3.1.3. Silicide Formation Temperatures

A remarkable discovery from the studies of silicide formations in thin-film couples is that many silicides were observed to form at very low temperatures. From Table 2-8, Ni_2Si , Pd_2Si , and Pt_2Si can be formed at temperatures as low as 100 to 200°C. Furthermore, when very clean substrates (such as cleaved Si) and ultra high vacuum (UHV) are used during metal film deposition, silicide formation can occur at room temperature during the deposition process. This phenomenon has been reported for Pd-

Si [51], Ti-Si and Sc-Si [52] as well as other systems, and it has been widely accepted [17, 53]. Obviously, these reaction temperatures are much lower than those observed in bulk couples. This is, according to Tu [22], due to the cleanliness of the interface between thin films and substrates and highly defective microstructures in thin-film couples.

Giudice et al [52] have detected silicide formation during the deposition of metal at room temperature. It is interesting that multiple phase growth was found in this investigation. Fig. 2-5 shows these results. When the deposited Ti layer has a thickness less than or equal to one monolayer, a Si-rich phase grows. When the deposited and reacted overlayer is between one to four monolayers, TiSi is formed until the thickness of the overlayer reaches 11 monolayers. Following this, a TiSi_x ($5 < x < 15\%$) solid solution phase begins to grow and this final phase yields a metal overlayer. A similar result for the Sc-Si reaction at room temperature is also shown in Fig. 2-5.

2.3.2. Other Experimental Phenomena Related to Transition Metal Silicide Formation

In order to understand the reaction process of silicide formations better, some important experimental phenomena are briefly described below.

2.3.2.1. Competitive Growth

Fig. 2-6 shows schematically an experiment [25, 44] in which a thin Co layer was deposited onto a CoSi layer, previously formed on a Si substrate. When the specimen was annealed at 460°C, it was found that a Co₂Si layer began to grow between the Co layer and the CoSi layer and that the existing CoSi layer, instead of growing, began to shrink. Upon further annealing, the growth of Co₂Si dominated at the expense of CoSi and Co. Finally, CoSi vanished leaving a Si/Co₂Si/Co structure (Fig. 2-6). Then, with continued annealing, Co₂Si grew until all the Co was consumed. CoSi then reappeared between Si and Co₂Si, and CoSi grew by consuming Co₂Si and Si. The same phenomena were also observed when Co was replaced with Ni or Pt [24, 54].

This experiment is significant because it confirms that single layer growth of silicides in thin film couples is a competitive process. In this process, when a new phase starts to nucleate and grow, a phase that had already nucleated and grown could decrease in size and even disappear due to kinetic conditions. Thus, it is possible during initial stages of single phase growth for more than one phase to nucleate, however, only the kinetically preferred phase will grow. The kinetic conditions, suggested by Tu [25], include the diffusivities of the moving species in both phases and an interfacial reaction barrier (see section 2.3.4.3).

2.3.2.2. Silicide Formation in Lateral Diffusion Couples

Thin-film lateral diffusion couples have been investigated [45] in order to explore the difference in phase sequence behavior in thin-film and bulk planar couples. In this experiment, a Si film, 50 nm thick, was deposited onto a Al_2O_3 substrate, followed by deposition of a 120 nm thick Ni island ($400 \times 400 \mu\text{m}^2$). The samples were subjected to a preanneal and then were heat treated at different temperatures (400 to 800°C) for different periods. Fig. 2-7 shows a cross-section of this configuration from one of the annealed samples. It can be seen that at the beginning of the reaction, only one phase, i.e. Ni_2Si , was formed and that other phases did not show up until a critical thickness of Ni_2Si was reached. This experiment successfully demonstrated that both thin-film couples and bulk couples would only have one phase form at the beginning of the reaction and that the first phase formed in both configurations may be same. Moreover, this experiment demonstrated that the difference in formation sequence, after the first phase is formed, is produced by the source limitation of one component in the couple. If the source of one component is not enough for the first phase to grow over its critical thickness, a single phase growth sequence will occur. This can be confirmed by an experiment with a thick metal film on a Si substrate [24]. Fig. 2-8 shows the results of these experiments with Co and Rh films on Si. It is clear that three phases are present. Moreover, Co and Rh behave differently. With Co, CoSi grows on silicon, while for Rh,

Rh_2Si grows on the metal side. This is because for Co the metal is major diffuser, but for Rh the silicon is the major diffuser. According to Ottaviani [24], the Co film should be a few hundred nanometers thick in order to obtain such an effect.

2.3.2.3. Diffusion in Thin-Film Couples

Because of the difficulties in determining the concentration and hence the concentration gradient in thin-film couples, most of the experimental studies of diffusion in this area are limited to identification of the major diffusers [1, 20, 23, 24, 55-61]. These studies are very important in explaining the complicated phenomena in thin-film metal-silicon reactions. For instance, in the example of the simultaneous growth of two phases described above, the second phase that formed is CoSi in Co-Si system but Rh_3Si_2 in Rh-Si system. This difference is due to Co being the major diffuser in the former case, whereas Si is the major diffuser in the latter case.

The major diffusers in most transition metal silicides are well documented. Table 2-9 shows a summary of major diffusers determined from marker experiments [1, 20, 23, 24, 55-61]. It is notable, according to this table, that in V_3Si , Co_2Si , Ni_2Si , Pt_2Si , Ru_2Si_3 , Os_2Si_3 , Rh_4Si_5 , and most of the disilicides (with the exception of NiSi_2 and CoSi_2), the majority atoms are the most mobile. This phenomenon is called, by some authors [23, 62], an "ordered Cu_3Au effect". According to these authors [23], the majority atoms constitute a continuous network on which a vacancy can easily migrate. Conversely, the motion of minority atoms

requires either the coexistence of two vacancies (minority and majority) or a local destruction of the crystalline lattice. In either case the motion of the minority atoms will be characterized by an activation energy considerably larger than that for the majority atoms.

For monosilicides, such as NiSi, CoSi, PtSi, FeSi, IrSi, etc., there is no general rule for major diffusers. Even the silicides which are isostructural compounds may have different moving species. As an example, NiSi, CoSi, FeSi, and IrSi all have the FeSi-B20 structure, but, from Table 9, metal atoms are the moving species in NiSi while Si is the major diffuser in FeSi, IrSi, and CoSi.

2.3.2.4. Impurity Effects

Impurities are usually introduced for various reasons, such as impurities incorporated in the thin metal film during deposition, impurities implanted into substrates, and impurities diffusing into the thin film from the annealing environment.

The existence of impurities will have very important effects on the silicide formation process. It has been found that impurities can greatly decrease the diffusivity of the moving species. For instance, when a Pt-Si couple was annealed in a UHV system, the diffusion coefficient of Pt was about one order of magnitude higher than that for a Pt-Si couple annealed in the usual condition [20]. In another experiment with a Ni-Si thin-film couple, it was suggested that oxygen diffused through the Ni film to the silicide/metal interface and prevented Ni transport [20]. Unfortunately, the reason

for the decrease or the inhibition of metallic atom diffusion is still not clear. Further investigation is required.

What is more important about the impurity effects is how the changes in diffusivities of the moving species will affect the silicide formation sequence. Fig. 2-9 shows schematically the experimental results for Pt (Fig. 2-9a) and Mo (Fig. 2-9b) intentionally doped with oxygen. PtSi forms between Pt₂Si and Si in the presence of unreacted Pt [63], whereas usually it will not begin to form until all the Pt is consumed. Furthermore, Pt₂Si is consumed by PtSi growth before Pt is exhausted. From Fig. 2-9b, it can be seen that Mo₅Si₃ forms and grows between MoSi₂ and Mo until Mo is totally consumed [64]. It is worth noting that Pt is the major diffuser in Pt-Si couples and Si is the major diffuser in Mo-Si couples. The diffusivities of both moving species are decreased by oxygen. By comparing Fig. 2-9 with Fig. 2-8, the difference between these two types of silicide formation is evident. In Fig. 2-8, the diffusion flux of the moving species is changed by thickening of the silicide layer, whereas the flux change of the moving species is caused by the impurities (oxygen) in Fig. 2-9. On the other hand, one can also find the important common feature of both types of silicide formation, i.e. decreasing flux of the moving species induces the second phase to form.

2.3.2.5. Alloy Thin-Film Couples

A de-alloying process in alloy films of Pt with W or Cr has been reported [65-67]. It is shown schematically in Fig. 2-10. The

first phase to form is PtSi, instead of Pt₂Si which forms in a thin-film couple with pure Pt film on Si substrate. The growth kinetics of PtSi is proportional to the square root of time and the activation energy is around 193 kJ/mol, which is different from that found for Pt deposited onto silicon. Ottaviani [24] has pointed out that, in these cases, the release of the platinum atoms from the alloy is the rate-limiting step. These results imply that the rate for the diffuser to arrive at the interface may have an important effect on the formation of the first phase.

2.3.3. Kinetics of Silicide Formation

This topic has been extensively investigated and has been reviewed by many authors [1, 2, 20, 22-25]. In this section, kinetic phenomena and the current theories will be briefly reviewed.

Kinetic behaviour is determined by monitoring the silicide growth process. The most often used techniques in these investigations are RBS and XRD. The cross-sectional TEM technique is also adopted to investigate the kinetics. Although this technique has better in-depth resolution and, therefore, is more accurate and reliable, it is still not widely used in this area of research due to the complicated process of specimen preparation.

The kinetics of thin-film silicide formation can be classified into three types, i.e. diffusion controlled processes, interface reaction controlled processes, and nucleation controlled processes. The first two types of kinetics are used to describe the layered growth process of silicides. The information for determining these

two types of kinetics is the thickness change of the growing silicides with annealing time. The thicknesses are plotted vs. either the annealing time or the square root of the annealing time for each temperature at which the samples are annealed. If a straight line is obtained from the plot with the thickness vs square root of the time, this type of growth process is classified as a diffusion controlled process. If the experimental data fit a straight line in a thickness vs time plot, this process is named an interface reaction controlled process [1, 2, 20, 23].

The other type of kinetics is used to explain island growth of silicides. As is shown in Fig. 2-11, in layered growth processes, silicides nucleate almost simultaneously at the entire interface between metal and Si substrate and then grow in one dimension. However, in an island growth process, silicides nucleate first at some points of the interface and then grow in three dimensions [6, 23]. Therefore, this type of kinetics is a nucleation controlled process. Table 2-10 lists the current kinetic classifications for various silicide reactions from experimental observations [20, 23]. Each type of kinetics will be discussed below.

2.3.3.1. Diffusion Controlled and Interface Reaction Controlled Processes

Gösele and Tu [22, 25, 37] have derived an expression for diffusion flux involving interface controlled diffusion processes. The model used by them is illustrated in Fig. 2-12 . Schematic concentration profiles are shown of an element A across the entire

region of diffusion forming the $A_\beta B$ compound, with and without an interfacial reaction barrier between two saturated $A_\alpha B$ and $A_\gamma B$ phases. The subscripts $\alpha > \beta > \gamma$ indicate the number of A atoms per B atom in each phase. In Fig. 2-12, the concentration profile of component A in the absence of interfacial reaction barriers is indicated by a dashed line. The concentration of A at the interface is given by its corresponding equilibrium values $C_{\beta\alpha}^{eq}$ and $C_{\beta\gamma}^{eq}$. In the

presence of interfacial reaction barriers, the concentration gradient across the $A_\beta B$ layer is smaller, and the actual concentrations at the interfaces are $C_{\beta\alpha} < C_{\beta\alpha}^{eq}$ and $C_{\beta\gamma} > C_{\beta\gamma}^{eq}$. Gösele and Tu assumed that

the $A_\beta B$ layer may be characterized by an essentially constant chemical interdiffusion coefficient D_β^* , a steady state of diffusion fluxes, and compound formation only occurring at the interface. From this model and these assumptions the fluxes of A atoms at interfaces of α/β and β/γ are derived as follows:

$$\begin{aligned} J_\beta^A &= - D_\beta^* \left(\frac{dC_\beta^A}{dx} \right)_{\beta\alpha} = - D_\beta^* \left(\frac{dC_\beta^A}{dx} \right)_{\beta\gamma} \\ &= - D_\beta^* \frac{(C_{\beta\gamma} - C_{\beta\alpha})}{x_\beta} \end{aligned} \quad (2-2)^{**},$$

** In the original papers, there is a mistake in this equation, i.e.

$J_\beta = - D_\beta^* \frac{(C_{\beta\alpha} - C_{\beta\gamma})}{x_\beta}$. In order to make sure that the flux direction is down the concentration gradient, $(C_{\beta\alpha} - C_{\beta\gamma})$ has to be changed to $(C_{\beta\gamma} - C_{\beta\alpha})$.

in which $(\frac{dC_{\beta}^A}{dx})_{\beta\alpha}$ and $(\frac{dC_{\beta}^A}{dx})_{\beta\gamma}$ are the concentration gradients of A atoms at interfaces α/β and β/γ , respectively. According to Till [22], the flux J_{β}^A may also be expressed in terms of the reaction constants $\kappa_{\beta\alpha}$ and $\kappa_{\beta\gamma}$ at the two interfaces:

$$J_{\beta}^A = \kappa_{\beta\alpha}(C_{\beta\alpha}^{eq} - C_{\beta\alpha}) \quad (2-3)$$

$$\text{or } J_{\beta}^A = \kappa_{\beta\gamma}(C_{\beta\gamma} - C_{\beta\gamma}^{eq}) \quad (2-4).$$

By combining Eq. (2-3) and (2-4) into Eq. (2-2), they obtained the expression for flux J_{β}^A as:

$$J_{\beta}^A = \frac{\Delta C_{\beta}^{eq} k_{\beta}^{eff}}{(1 + x_{\beta} k_{\beta}^{eff}/D_{\beta}^*)} \quad (2-5);$$

where $\Delta C_{\beta}^{eq} = (C_{\beta\alpha}^{eq} - C_{\beta\gamma}^{eq})$ and $\frac{1}{k_{\beta}^{eff}} = \frac{1}{\kappa_{\beta\alpha}} + \frac{1}{\kappa_{\beta\gamma}}$; k_{β}^{eff} is called the effective interfacial reaction barrier for the $A_{\beta}B$ layer. Inserting Eq. 2-5 into Eq. 2-6, which represents the rate of the change in the layer thickness,

$$\frac{dx_{\beta}}{dt} = \left\{ \frac{1}{(C_{\beta\alpha}^{eq} - C_{\beta\alpha})} + \frac{1}{(C_{\beta\gamma} - C_{\beta\gamma}^{eq})} \right\} J_{\beta}^A \quad (2-6);$$

they obtained the following equation:

$$\frac{dx_\beta}{dt} = \frac{G_\beta \Delta C_\beta^{\text{eq}} k_\beta^{\text{eff}}}{(1 + x_\beta k_\beta^{\text{eff}} / D_\beta^*)} \quad (2-7).$$

G_β is a constant determined by the composition of the three phases $A_\alpha B$, $A_\beta B$, and $A_\gamma B$, i.e.

$$G_\beta = \Omega_0 (1 + \beta)^2 \left(\frac{1}{\alpha - \beta} + \frac{1}{\beta - \gamma} \right) \quad (2-8).$$

Ω_0 is the volume per A or B atom and the Ω_0 is assumed to be constant throughout the sample. A similar equation to Eq. 2-7 has been derived by other authors [68, 69].

From Eq. 2-7, a changeover thickness x_β^* can be defined by

$$x_\beta^* = \frac{D_\beta^*}{k_\beta^{\text{eff}}} \quad (2-9).$$

It can be seen that the growth kinetics described by Eq. 2-7 are different below and above the changeover thickness. It follows that

$$\frac{dx_\beta}{dt} \approx G_\beta \Delta C_\beta^{\text{eq}} k_\beta^{\text{eff}}, \text{ or } x_\beta \propto t, \text{ for } x_\beta \ll x_\beta^* \quad (2-10);$$

$$\frac{dx_{\beta}}{dt} = G_{\beta} \Delta C_{\beta}^{eq} \frac{D_{\beta}^*}{x_{\beta}}, \text{ or } x_{\beta} \propto \sqrt{t}, \text{ for } x_{\beta} \gg x_{\beta}^* \quad (2-11).$$

Eq. 2-10 and 2-11 indicate that the growth process is interface reaction controlled when $x_{\beta} < x_{\beta}^*$, whereas the growth process is diffusion-controlled when $x_{\beta} \gg x_{\beta}^*$. According to this theory, whenever planar growth of a compound takes place, it should pass through two stages. Initially, growth will follow interface controlled kinetics. After the layer has grown so that the condition $x_{\beta} \gg x_{\beta}^*$ is satisfied, the process will change over to diffusion controlled growth kinetics. This theory can explain many cases well where a thickness against time relationship has been experimentally established, such as WSi_2 , $MoSi_2$, and $TiSi_2$ etc. For these silicides, when bulk diffusion couples are used, the growth kinetics is diffusion controlled [1]. But, when thin-film couples are used, in most observed cases, the processes for the growth of WSi_2 , $MoSi_2$, and $TaSi_2$ etc. are interface controlled (Table 2-10, [20, 23]). The implication is that the thicknesses of the silicide layers obtained in thin film couples are smaller than the changeover thicknesses for these silicides.

On the other hand, this theory also has some problems. First of all, the theory does not describe the growth behaviour when x_{β} is close to x_{β}^* . Another problem is that the physical meaning of the term, "effective interface barrier", is still not very clear. A further

definition needs to be given to the term. Recently, from investigations of WSi_2 , it has been found that the so called interface barrier for WSi_2 formation is in fact an oxide layer which prevents Si atoms from penetrating the interface and therefore delays the WSi_2 reaction [70-72]. It is also reported that the formation of this oxide layer may be thermodynamically driven and that the layer can even appear at the original clean interface after W film deposition, if the diffusion of oxygen in the metal film is rapid enough [71]. After special techniques, such as ion beam mixing and rapid thermal annealing, are used to break down the oxide layer already formed, the growth of WSi_2 is found to follow diffusion controlled kinetic behaviour [71-73].

The other problem is that all the silicides, listed in the column of diffusion controlled kinetics in Table 2-10, are not reported to show any interface reaction controlled behaviour. Considering the limitation of the in-depth resolution of RBS and XRD, which were used for most kinetics investigations, it could be said that if there exists any changeover thickness x_p^* for all these silicides, then it must be less than 20 nm (the limit of resolution).

The questions arising from these problems are:

- 1) What is the interface barrier?
- 2) Is the interface barrier characteristic of the interface reaction during solid compound formation or does the barrier only arise from the impurity effects caused by specimen preparation and the annealing environment?

More studies need to be conducted to answer these questions.

2.3.3.2. Nucleation Controlled Processes

Nucleation controlled processes for silicide formation have been reviewed by d'Heurle and Gas [23]. They use classical nucleation theory to discuss the phenomena encountered in thin film reactions. According to the classical theory of nucleation, the activation energy ΔG^* for a new phase AB forming at an interface between two phases A and B, is proportional to $\frac{(\Delta\sigma)^3}{(\Delta G)^2}$. $\Delta\sigma$ indicates the increase in surface energy, because two interfaces A/AB and AB/B replace the original A/B interface during AB formation; ΔG is the change of free energy per unit volume of AB and is given below:

$$\Delta G = \Delta G_c - \Delta H_d \quad (2-12).$$

ΔG_c is the change in "chemical" free energy per unit volume of AB due to the formation of the new phase and ΔH_d is the deformation energy loss due to the volume change caused by phase transformation. Therefore, ΔG^* can be written as:

$$\Delta G^* \propto \frac{(\Delta\sigma)^3}{(\Delta G_c - \Delta H_d)^2} \quad (2-13).$$

According to d'Heurle and Gas [23], in general, when metals and silicon react with one another to form silicides, the absolute value of ΔG 's are large and the ΔG^* 's are small. As a result, nucleation is so easy and rapid that one can not isolate it and observe it

experimentally. There are, however, two types of silicide reactions whose nucleation processes are rather slow, so that the growth processes of these silicides show an island growth behaviour.

One example of these two reactions is rare earth metal (R.E.)-Si reactions to form silicides with a formula $(\text{R.E.})\text{Si}_{1.7}$ [74, 75]. In this type of reaction, the silicon atoms are very mobile [76] because they act like interstitials. The silicon sublattice contains 15% vacancies, since the structure is that of AB_2 but the composition is $\text{R.E.}\text{Si}_{1.7}$. The relatively high mobility of Si atoms allow the growth of silicides at low temperatures (about 300°C). On the other hand, the metal atoms in the silicides do not become mobile until extremely high temperatures, of the order of 1000°C . Therefore, when the silicides are formed at low temperatures (such as around 300°C), the deformation stress can not be relaxed easily. The result is a large ΔH_d and small $|\Delta G_c - \Delta H_d|$. Consequently, ΔG^* is large and the growth of these silicides is nucleation controlled.

The other type of nucleation controlled reaction is observed in the following silicides: $\text{Mn}_{11}\text{Si}_{19}$ [6], NiSi_2 [23], ZrSi_2 [23], Rh_4Si_5 [77], Rh_3Si_4 [77], PdSi [23], HfSi_2 [23], OsSi_2 [23], and IrSi_3 [23]. In this case, ΔG_c is very small and causes ΔG^* to be so large that the growth process becomes nucleation controlled. For example, in the formation of NiSi_2 [23], the reaction of Ni with Si results in diffusion controlled formation of Ni_2Si and NiSi at temperatures below 500°C . After total formation of NiSi (no Ni or Ni_2Si remaining), further heating does not cause any other change until about 800°C . Then, the sudden formation of NiSi_2 in islands is

observed. The islands spread through the whole thickness of the films. In this process, the equation for the reaction is



because the NiSi layer already exists on the Si substrate. Thus, the "chemical" free energy change for this reaction, instead of being the free energy of NiSi₂ formation, $\Delta G_{\text{NiSi}_2}^f$, should be the difference between $\Delta G_{\text{NiSi}_2}^f$ and the free energy of NiSi formation, ΔG_{NiSi}^f , i.e. $\Delta G_c = \Delta G_{\text{NiSi}_2}^f - \Delta G_{\text{NiSi}}^f$. Since these two quantities of free energy of formation are nearly equal, ΔG_c is close to zero. This causes ΔG^* to be large. At temperature T^* , where nucleation occurs, the diffusion coefficients are quite large so that growth of the nuclei is extremely rapid [23].

The theory of nucleation-controlled growth described above can qualitatively explain island growth in the two types of silicide formation quite well, although, according to d'Heurle and Gas [23], more work needs to be done for the model of R.E.Si_{1.7} formation.

2.3.4. Theories And Models For Growth Sequence During Silicide Formation

In this section, several general models intended to be applicable to all transition metal silicides are briefly introduced and discussed. Since this topic involves some basic diffusion theories, classical theory governing diffusion reactions in bulk couples is also reviewed.

2.3.4.1. Kinetics Of Layered Growth In Bulk Couples — Kidson Approach

Kidson [38] has treated the growth of diffusion layers of multiple phase systems in binary bulk couples. Fig. 2-13 shows schematically a profile of the concentration of element A in a bulk couple and a binary phase diagram of A and B. In Fig. 2-13, β and γ are two intermediate phases in the system. $x_{\alpha\beta}$ and $x_{\beta\gamma}$ indicate the positions of the interfaces of α/β and β/γ , respectively. $C_{\alpha\beta}$, $C_{\beta\alpha}$, $C_{\beta\gamma}$, and $C_{\gamma\beta}$ are the concentrations of element A at the interfaces. According to Kidson, the rate of advance of interface $x_{\alpha\beta}$ is given by

$$(C_{\alpha\beta} - C_{\beta\alpha}) \frac{dx_{\alpha\beta}}{dt} = J_{\alpha\beta} - J_{\beta\alpha} \quad (2-15);$$

where $J_{\alpha\beta}$ and $J_{\beta\alpha}$ are the fluxes of A at each side of interface $x_{\alpha\beta}$, separately. From Fick's first law,

$$J_{\alpha\beta} = -D \left(\frac{\partial C}{\partial x} \right)_{\alpha\beta} \quad (2-16);$$

$$J_{\beta\alpha} = -D \left(\frac{\partial C}{\partial x} \right)_{\beta\alpha} \quad (2-17).$$

Since the system under consideration fulfils the conditions required for the application of the Boltzmann theorem,

$$\frac{\partial C}{\partial x} = \frac{1}{\sqrt{t}} \frac{dC}{d\lambda} \quad (2-18),$$

where $\lambda = \frac{x}{\sqrt{t}}$ and $\frac{dC}{d\lambda} = K$ is a constant. By combining Eq. 2-16, 2-17, and 2-18 into Eq. 2-15, one obtains

$$\frac{dx_{\alpha\beta}}{dt} = \frac{(DK)_{\beta\alpha} - (DK)_{\alpha\beta}}{C_{\alpha\beta} - C_{\beta\alpha}} \frac{1}{\sqrt{t}} \quad (2-19),$$

or in integrated form

$$\begin{aligned} x_{\alpha\beta} &= 2 \frac{(DK)_{\beta\alpha} - (DK)_{\alpha\beta}}{C_{\alpha\beta} - C_{\beta\alpha}} \sqrt{t} \\ &= A_{\alpha\beta} \sqrt{t} \end{aligned} \quad (2-20).$$

A similar formula for interface $x_{\beta\gamma}$ can be obtained:

$$\begin{aligned} x_{\beta\gamma} &= 2 \frac{(DK)_{\gamma\beta} - (DK)_{\beta\gamma}}{C_{\beta\gamma} - C_{\gamma\beta}} \sqrt{t} \\ &= A_{\beta\gamma} \sqrt{t} \end{aligned} \quad (2-21).$$

Therefore, the thickness of the β phase layer, as a function of time, is

$$\begin{aligned}x_{\beta} &= x_{\beta\gamma} - x_{\alpha\beta} \\&= (A_{\beta\gamma} - A_{\alpha\beta}) \sqrt{t} \\&= B_{\beta} \sqrt{t}\end{aligned}\quad (2-22).$$

This is the well known parabolic growth law. This equation implies that in a multiple phase system, the thickness of any phase, as a function of time, depends only on the eight parameters (D and K) within that phase and its two immediately adjacent phases.

Kidson has discussed the physical meaning of B_{β} [38]. When $B_{\beta} > 0$, the rate of formation of the new β phase from the γ phase is larger than the transition of the β phase to the α phase and consequently, the thickness of the β increases with time. When $B_{\beta} < 0$, the rate of supply of A element from the α to β phase is so fast compared to the flow rate in the β phase that a "pile-up" of excess material occurs resulting in the direct transformation from the α to γ phase. In this case, no β phase would appear in the diffusion region. When $B_{\beta} = 0$, the situation is similar to $B_{\beta} < 0$, i.e. again no β phase appears. Therefore, it is possible for some phases to be absent from the diffusion region from a kinetic point of view. Kidson has, however, ruled out these latter two cases, i.e. $B_{\beta} \leq 0$. The situation where $B_{\beta} \leq 0$ would imply an infinite chemical potential gradient at the α/γ interface, which is contrary to the thermodynamic requirement that the chemical potential (μ_A) be continuous and monotonic throughout the bulk couple.

From results presented in the literature and particularly TEM observations of the interfaces in thin film couples, it has been shown that single phase growth is not impossible and is indeed the nature of silicide formation in thin film couples. Therefore, the parabolic growth law itself can not explain the phenomenon of single phase growth. In addition, Tu [22] also pointed out that, according to the parabolic law, the growth velocity is inversely proportional to the layer thickness. Thus, an existing phase can not vanish, since the velocity will become extremely large as the thickness approaches zero. But, from experimental observation (see 2.3.2.1. competitive growth), a phase already formed in a thin-film couple does vanish under certain conditions. It is obvious that a diffusion-controlled growth model can not explain the disappearance of phases, that have already nucleated and grown. As a result, a new theory has to be developed to explain the striking phenomena of diffusion reactions in thin-film couples. Any successful theory should be able, however, to explain the contradiction between the thermodynamic requirement of continuity of the chemical potential at the interface and the possible discontinuity of the chemical potential at the interface where a given phase is missing. From this literature survey, no theory, applicable to single phase growth, can explain this phenomenon.

2.3.4.2. Theory for Predicting the Growth Sequence of Silicide Formation

Walser and Bene [19] have suggested a rule for predicting the first phase to nucleate in transition metal silicon couples. The rule is as follows: "The first compound nucleated in planar binary (thin film) reaction couples is the most stable congruently melting compound adjacent to the lowest temperature eutectic on the bulk equilibrium phase diagram". This rule is based on the following facts and inferences.

Fact 1: For solid phase reactions involving silicide formation, binary couples are formed at temperatures far below the lowest eutectic and reactions are carried out in isothermal anneals at subeutectic ($T \approx \frac{1}{2} T_E$) temperatures.

Fact 2: Thin-film couples are prepared by evaporation or sputtering of the metal on a cold substrate of silicon.

Inference 1: The method of preparation of thin-film couples will result in the interface consisting essentially of a "metallic glass" with a concentration near the lowest-temperature eutectic in the binary system.

Inference 2: The nucleation process actually is a process of atomic rearrangement from liquidlike short-range order (SRO) to crystalline SRO. Since a higher energy barrier, associated with the large rearrangement, is required for noncongruent states than for congruent states at the same concentration, the nucleation process

would highly favor congruently melting states over noncongruent states.

Inference 3: If the concentration fluctuations driving nucleation are produced by a diffusion mechanism, the first phase that nucleates would be the congruent phase closest in concentration to the initial eutectic composition.

This rule appears to work in some cases, but it fails to predict the right phase for Ti-Si, Mn-Si, Hf-Si, and Mo-Si systems [2].

After examining phase diagrams and sequences of phase formation in several metal-silicon systems, Tsaur et al. [21] formulated this rule: "The second phase formed is the compound with the smallest ΔT that exists in the phase diagram between the composition of the first phase and the unreacted element". They defined ΔT as the temperature difference between the liquidus curve and the peritectic (or peritectoid) point for the system under consideration. In addition to the experimental results, this rule is based on the following theory. There exists an interface region between the silicide and pure element. The interfacial region has a width estimated to be $\leq 2\text{nm}$ and has a concentration profile with compositions ranging from the silicide to the pure element. Nucleation of compounds within this composition range can occur, but usually only one compound will nucleate and grow to a measurable amount. That is to say phase nucleation is a competitive process due to the variation of concentration in the interfacial region [21]. On the other hand, the larger the ΔT value for a peritectic phase, the larger the compositional difference between the solid peritectic compound and the liquidus phase at the

peritectic temperature. Therefore, a small difference in composition between the peritectic and liquid phase at the peritectic temperature yields a low-energy barrier for nucleation, because only small compositional fluctuations are required for nucleation. This rule for prediction of second phase formation in thin-film reactions can explain the formation sequences in Pd-Si, Pt-Si, Ni-Si, Co-Si, and some other systems.

It is noteworthy that both rules, mentioned above emphasize the effect of nucleation on the phase formation. But, they do not put much emphasis on the effect of diffusion on the formation sequence. For example, the first rule, in fact, implies that the phase which nucleates first is the phase which grows first. This is not true if the growth process involves diffusion. According to the competitive growth experiment (see section 2.3.2.1), a phase already nucleated, instead of continuing to grow, can be consumed by a new growing phase due to kinetic conditions such as diffusion. Therefore, in order to make sure that the phase nucleated first is the one grown first, this rule requires the "metallic glass" assumption at the interface to be valid for the entire first phase formation process. Again, this situation may not be true because, at the annealing temperature, the metallic glass is supposed to crystallize and its composition may be changed by diffusion. In addition, these theories can not explain why the configuration with an alloyed metal film on a Si substrate can form a different first phase from the usual thin-film couple (see 2.3.2.5. alloy thin-film couples), and why impurities can cause multiple phase growth (see 2.3.2.4; impurity effect).

2.3.4.3. Theory of Single Phase Growth in Thin-Film Couples

This theory was suggested by Gösele and Tu [22, 25, 37]. They adopted a competitive growth model of two phases in thin-film couples (as shown in Fig. 2-14). An almost identical model has been developed by d'Heurle and Gas [23] using a slightly different mathematical derivation. Because of the similarity of these two models, one of them, Gosele and Tu's model, is selected to be briefly reviewed. This model involves both interface reaction controlled and diffusion controlled processes. The flux of A atoms into the $A_\gamma B$ phase, J_γ^A , is derived in a similar manner to the flux of A atoms into the $A_\beta B$ phase (Eq. 2-5, Section 2.3.3.1), and can be given by the following:

$$J_\gamma^A = \frac{\Delta C_\gamma^{\text{eq}} k_\gamma^{\text{eff}}}{(1 + x_\gamma k_\gamma^{\text{eff}} / D_\gamma^*)} \quad (2-23).$$

$\Delta C_\gamma^{\text{eq}} = C_{\gamma\beta}^{\text{eq}} - C_{\gamma\delta}^{\text{eq}}$ is the difference in the equilibrium concentration of A atoms in $A_\gamma B$ phase, k_γ^{eff} and D_γ^* are the effective interfacial reaction barrier and chemical interdiffusion constant for the $A_\gamma B$ phase, respectively and x_γ indicates the thickness of $A_\gamma B$ phase. From Eq. 2-23, a changeover thickness x_γ^* can be defined for $A_\gamma B$:

$$x_Y^* = \frac{D_Y}{k_Y^{\text{eff}}} \quad (2-24).$$

According to Gösele and Tu [37], because of the nature of the competitive growth, the growth rate of the two phases, β and γ , should be

$$\frac{dx_\beta}{dt} = G_\beta J_\beta^A - G_{\beta\gamma} J_\gamma^A \quad (2-25),$$

$$\frac{dx_\gamma}{dt} = G_\gamma J_\gamma^A - G_{\gamma\beta} J_\beta^A \quad (2-26);$$

where G_β , G_γ , $G_{\beta\gamma}$, and $G_{\gamma\beta}$ are constants determined by the compositions of the compounds $A_\alpha B$, $A_\beta B$, $A_\gamma B$, and $A_\delta B$. Eq. 2-25 and 2-26 represent the growth conditions of the $A_\beta B$ and $A_\gamma B$ layers. If $\frac{dx_\beta}{dt} > 0$, the $A_\beta B$ layer will grow. From Eq. 2-25, this condition can also be expressed by

$$\frac{J_\beta^A}{J_\gamma^A} > \frac{G_{\beta\gamma}}{G_\beta} = r_1 \quad (2-27).$$

Similarly, the growth condition for the $A_\gamma B$ layer is

$$\frac{J_\beta^A}{J_\gamma^A} < \frac{G_\gamma}{G_{\beta\gamma}} = r_2 \quad (2-28).$$

In Eq. 2-27 and 2-28, r_1 and r_2 are constants, and it can be proven that

$$r_2 > r_1 \quad (2-29).$$

Based on these conditions, Gösele and Tu defined a convenient parameter for single phase growth kinetics, in terms of the flux ratio, i.e.

$$r = \frac{J_{\beta}^A}{J_{\gamma}^A} \quad (2-30).$$

Applying this parameter, r , combined with Eq. 2-10 and 2-11 (see section 2.3.3.1), they analysed and discussed various possibilities related to the thin-film diffusion couples as summarized in Table 2-11 and Fig. 2-15. In their analysis and explanation of single phase growth kinetics, the most important point is the critical thickness of phases (β and γ), x_{β}^c and x_{γ}^c . Below these thicknesses only single

phase ($A_{\beta}B$ or $A_{\gamma}B$) growth actually occurs whereas above these critical values simultaneous growth of two phases must result. This point has in fact become the basis of all explanations about these unique phenomena in thin-film reactions. These critical values can be derived from Table 2-11 at the conditions $r = r_1$ for x_{γ}^c and $r = r_2$ for x_{β}^c .

$$x_{\gamma}^c = \frac{G_{\beta\gamma} \Delta C_{\gamma}^{eq} D_{\gamma}^*}{G_{\beta} \Delta C_{\beta}^{eq} k_{\beta}^{eq}} \quad (2-31),$$

$$x_{\beta}^c = \frac{G_{\beta\gamma} \Delta C_{\beta}^{eq} D_{\beta}^*}{G_{\gamma} \Delta C_{\gamma}^{eq} k_{\gamma}^{eq}} \quad (2-32).$$

From Table 2-11 and Fig. 2-15, it can be seen that single layer growth can be explained as follows. If there is unlimited supply of A and B, sooner or later, $A_{\gamma}B$ (assuming it forms first) can grow and exceed x_{γ}^c . At this point, two compounds ($A_{\gamma}B$ and $A_{\beta}B$) grow at the same time. If the material supply, for example B, is consumed before $x_{\gamma} > x_{\gamma}^c$, the thickening process of $A_{\gamma}B$ will stop. After a short transition period a new steady-state diffusion situation will develop, which may approximately be described by $J_{\gamma}^A = 0$. Thus, Eq. 2-25 and 2-26 change into

$$\frac{dx_{\beta}}{dt} = G_{\beta} J_{\beta}^A > 0 \quad (2-33),$$

$$\frac{dx_{\gamma}}{dt} = -G_{\gamma\beta} J_{\beta}^A < 0 \quad (2-34);$$

which indicate that the $A_{\beta}B$ phase will form and grow whereas the $A_{\gamma}B$ will shrink. This theory has been used to explain the competitive growth of Co_2Si and $CoSi$, Ni_2Si and $NiSi$, as well as

Pt₂Si and PtSi. It is successful in proving that an existing phase can vanish due to kinetic reasons. It can also quantitatively explain some other cases where single phase growth takes place and is helpful in understanding the effects of diffusion on the growth sequence.

There are some problems which can not be explained by this theory. For example, as Tu [22, 25] pointed out, this theory states that only the phase with the fastest growth rate can form. This may not be true. In a Ni-Si lateral diffusion couple experiment (see section 2.3.2.2), after Ni₂Si forms the next phase to form is Ni₃Si₂ and the interface between Ni₂Si and Ni₃Si₂ moves opposite to the Ni flux. This indicates that $J_{\text{Ni}_3\text{Si}_2} \geq J_{\text{Ni}_2\text{Si}}$. From other investigations, Ni₃Si₂ has the largest thickness in bulk couples [43, 45], i.e. Ni₃Si₂ has the fastest growth rate. However, it is not the first phase appearing in the thin-film couple, and it does not appear in the single phase formation sequence.

2.3.4.4. Model of Growth Sequence Determined by Interfacial Composition

After examining different models and particular experiments, Ottaviani [24] suggested another model for the growth sequence in thin-film reactions. This model assumes that selective growth of a phase is mainly initiated by an interface composition that is governed, in turn, by the flux of the various elements to the interface. This model also suggests that the stabilities of the

phases influence which compound will be formed, but that not all possible compounds can grow.

According to this model, if several compounds, such as phases I, II, and III in Fig. 2-16, are thermodynamically possible to form at an interface, and if the composition at the interface is l , only phase I can be formed. When the composition in the interface is changed to m , only phase II can be formed. Using this model, Ottaviani [24] has explained the phenomena of single phase growth in thin-film couples, multiple phase growth in bulk couples, and multiple phase growth in thin-film couples with impurities. It appears that Ottaviani's model can explain many of the phenomena involving diffusion reactions in both thin-film couples and bulk couples more reasonably than other theories. However, this model is still very qualitative and much more work needs to be done to understand the physical processes which actually occur during the diffusion reactions.

The first problem which must be solved concerns the relationship between the diffusion fluxes and the composition at the interface, i.e. how the diffusion fluxes govern the composition at the interface.

The second problem is how much composition change is required to initialize new phase formation. The diffusion fluxes in bulk couples will continuously and gradually change, whereas the diffusion fluxes in thin-film couples with impurities can change abruptly and very rapidly. In the former case, the composition at the interface will change continuously and slowly. But, in the latter case, the composition will vary suddenly and rapidly. This may be

the reason that multiple phase growth in bulk couples can only be seen after long annealing (see section 2.3.2.2) periods at high temperatures, when each phase is relatively thick. However, in thin film couples, multiple phase growth can be seen after short annealing periods at lower temperatures compared with that for bulk couples, and when each phase has a thickness less than 100nm. There must, therefore, be some threshold composition change at which new phase formation is induced.

In this literature review, a number of general models and theories for silicide formation in thin-film couples have been briefly introduced and discussed. One common feature of most of these theories is that they consider the thin-film reaction as the initial stage of the diffusion reaction in bulk couples [22-26, 37]. In thin-film reaction processes involving multiple phase growth, which take place before any element (metal or silicon) is exhausted, this may be true. Otherwise, it is not true. Quite simply, the diffusion reaction process in a bulk couple is not the same as that in a thin-film couple. Fig. 2-17 shows the difference using as an example the Ni-Si couple. Initially, the reaction for both couples will be

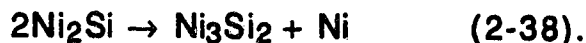


and Ni should diffuse through the growing new phase, Ni_2Si , to arrive at the interface between Ni_2Si and Si. There, the reaction described by Eq. 2-35 continues. Any further silicide formation will be different.

In the bulk couple, as soon as Ni_2Si exceeds a critical thickness, a new phase will begin to form according to the following reaction:



In the thin-film couple, however, as soon as the Ni is completely consumed, a new phase (for example, Ni_3Si_2) will start to form by one of the following reactions:



Which of these actually occurs depends on the standard free energy ΔG° of each reaction. Only reactions with $\Delta G^\circ < 0$ can occur. It is noteworthy that $|\Delta G^\circ|$ for reaction $3\text{Ni} + 2\text{Si} \rightarrow \text{Ni}_3\text{Si}_2$ will be much larger than that for either reaction in the thin-film couple. Therefore, that Ni_3Si_2 is absent in thin-film couples may simply be because the $|\Delta G^\circ|$ for reaction (Eq. 2-37) or (Eq. 2-38) is too small to nucleate Ni_3Si_2 at the $\text{Ni}_2\text{Si}/\text{Si}$ interface. Thus the next phase which can form is NiSi . It can only form through one of the following two reactions because the original Ni film is already exhausted.





From Fig. 2-17a (for bulk diffusion couples), it can be seen that as long as a thin second phase layer is formed, the reaction for the phase adjacent to Si is still occurring between the elements, but the reactions for the phases separated from Si are all of the following type described below (this is, of course, assuming that Ni is the diffusing species):



Thus, Ni atoms diffuse through each phase to supply Ni to each reacting interface. For thin-film couples (Fig. 2-17b), it can be seen that after a thin NiSi layer is formed, the growth of this layer can follow different paths. If the formation is through reaction (Eq. 2-39), the layer should grow towards the surface, i.e. the reacting interface is located at the $\text{Ni}_2\text{Si}/\text{NiSi}$ interface. Si has to diffuse through the growing layer. If the formation is through reaction (Eq. 2-40), the layer should grow on both sides of itself. Both the $\text{Ni}_2\text{Si}/\text{NiSi}$ and NiSi/Si interfaces are reacting interfaces. Reaction (Eq. 2-40a) occurs at the $\text{Ni}_2\text{Si}/\text{NiSi}$ interface and reaction (Eq. 2-40b) at the other interface. Ni has to diffuse through the NiSi layer. Both of the two paths (reaction (Eq. 2-39) or reaction (Eq. 2-40)) are definitely different from the reaction process in bulk couples.

It is obvious that the reaction process in thin-film couples is much more dependent on the standard free energy of each reaction

than is the case in bulk diffusion couples. The standard free energy for reactions can, in some cases, determine which reaction should occur and therefore determine the moving species. For example, during NiSi formation in thin-film couples, which reaction (reaction (Eq. 2-39) or (Eq. 2-40)) actually occurs will be mainly determined by the free energy of each reaction and not by the mobility of these two elements. If ΔG° for reaction (Eq. 2-39) is less than zero while ΔG° for reaction (Eq. 2-40) is larger than zero, only reaction (Eq. 2-39) can actually take place and hence Si will be the moving species, and vice versa. From these inferences, it is possible that some of the moving species observed in thin-film reactions are not necessarily the faster diffusers in bulk couples. Unfortunately, the thermodynamic data are far from complete to calculate the standard free energies for many metal-Si reactions. Thus, this point of view can not be directly verified. At least, it is in agreement with the basic concept of thermodynamics.

Since all the phenomena observed in thin-film metal-Si reactions can not be explained by the known theories and models, it is necessary to develop new models based on the difference between the reactions in bulk couples and in thin-film couples.

Table 2-1. Tabulation of Transition Metals and Their Silicides [1]

Sc	Ti	V	Cr	Mn	Fe	Co	Ni	Cu
Sc ₅ Si ₃	Ti ₃ Si	V ₃ Si	Cr ₃ Si	Mn ₆ Si	Fe ₃ Si	Co ₃ Si	Ni ₃ Si	Cu ₅ Si
ScSi	Ti ₅ Si ₃	V ₅ Si ₃	Cr ₂ Si	Mn ₉ Si ₂	Fe ₁₁ Si ₅	Co ₂ Si	Ni ₃₁ Si ₁₂	Cu ₃₁ Si
Sc ₂ Si ₃	Ti ₅ Si ₄	V ₅ Si ₄	Cr ₅ Si ₃	Mn ₃ Si	Fe ₂ Si	CoSi	Ni ₅ Si ₂	Cu ₁₅ Si ₄
Sc ₃ Si ₅	TiSi	V ₆ Si ₅	Cr ₃ Si ₂	Mn ₅ Si ₂	Fe ₅ Si ₃	CoSi ₂	Ni ₂ Si	Cu ₃ Si
	TiSi ₂	VSi ₂	CrSi	Mn ₅ Si ₃	FeSi		Ni ₃ Si ₂	
			CrSi ₂	MnSi	FeSi ₂		NiSi	
				Mn ₃ Si ₅			NiSi ₂	
				Mn ₁₁ Si ₁₉				
				Mn ₄ Si ₇				
				MnSi ₂				
Y	Zr	Nb	Mo	Tc	Ru	Rh	Pd	Ag
Y ₅ Si ₃	Zr ₄ Si	Nb ₄ Si	Mo ₃ Si		Ru ₂ Si	Rh ₂ Si	Pd ₅ Si	
Y ₅ Si ₄	Zr ₃ Si	Nb ₃ Si	Mo ₅ Si ₃		Ru ₅ Si ₃	Rh ₅ Si ₃	Pd ₉ Si ₂	
YSi	Zr ₂ Si	Nb ₅ Si ₃	Mo ₃ Si ₂		Ru ₄ Si ₃	Ru ₂₀ Si ₁₃	Pd ₄ Si	
Y ₃ Si ₅	Zr ₅ Si ₃	NiSi ₂	MoSi ₂		RuSi	Rh ₃ Si ₂	Pd ₃ Si	
YSi _{1.7}	Zr ₃ Si ₂				Ru ₂ Si ₃	Rh ₅₈ Si ₄₂	Pd ₉ Si ₄	
YSi ₂	Zr ₄ Si ₃					RhSi	Pd ₂ Si	
	Zr ₅ Si ₄					Rh ₄ Si ₅	PdSi	
	Zr ₆ Si ₅					Rh ₃ Si ₄		
	ZrSi					Rh ₂ Si ₃		
	ZrSi ₂					RhSi ₂		
La	Hf	Ta	W	Re	Os	Ir	Pt	Au
La ₅ Si ₃	Hf ₂ Si	Ta _{4.5} Si	W ₃ Si	Re ₃ Si	OsSi	Ir ₃ Si	Pt ₄ Si	
La ₅ Si ₄	Hf ₅ Si ₃	Ta ₃ Si	W ₅ Si ₃	Re ₅ Si ₃	Os ₂ Si ₃	Ir ₂ Si	Pt ₃ Si	
La ₃ Si ₂	Hf ₃ Si ₂	Ta ₃ Si	W ₃ Si ₂	ReSi	OsSi _{1.8}	Ir ₃ Si ₂	Pt ₅ Si ₂	
LaSi	Hf ₄ Si ₃	Ta ₂ Si	WSi ₂	ReSi ₂	OsSi ₂	IrSi	Pt ₁₂ Si ₅	
LaSi ₂	Hf ₅ Si ₄	Ta ₅ Si ₃			OsSi _{2.4}	Ir ₄ Si ₅	Pt ₇ Si ₃	
	HfSi	TaSi ₂			OsSi ₃	Ir ₃ Si ₄	Pt ₂ Si	
	HfSi ₂					Ir ₂ Si ₃	Pt ₆ Si ₅	
						IrSi _{1.75}	PtSi	
						IrSi ₂		
						IrSi ₃		

Table 2-2 Si-Rich Silicides and Their Properties [1, 2, 34, 36]

Group	Silicide	ρ ($\mu\Omega$-cm)	Schottky Barrier Height (eV)	High Temp. Stability	Applications
near noble metal silicides	CoSi ₂ NiSi ₂ PdSi PtSi	low, < 50	greater than half the Si band gap energy, increase with atomic no.	poor	Schottky barrier or ohmic contacts
refractory metal silicides	TiSi ₂ ZrSi ₂ VSi ₂ NbSi ₂ TaSi ₂ MoSi ₂ WSi ₂	low < 100	all have similar value around 0.55	good	1) Schottky barrier contacts 2) gate metallization, interconnects in VLSI -
semi- conductor silicides	FeSi ₂ CrSi ₂ MnSi _{1.73} ReSi _{1.73} IrSi _{1.73}	high > 250	various values	variable	promising in applications such as laser detectors, LEDs fibre communi- cation devices

Table 2-3 Crystallographic Data for Manganese Silicides [1, 9]

Silicide	Crystal system	Name of structure	Lattice constant a (nm)	constant b (nm)	of unit c (nm)	cell β	m_i^*	ρ_i^{**}
Mn ₆ Si	H	R phase	1.0874		1.9177			
Mn ₉ Si ₂		Mn ₉ Si ₂	1.3362	1.1645	0.8734	90.53		
Mn ₃ Si	C	BiF ₃	0.5722				4	2.135
Mn ₅ Si ₂	T	Mn ₅ Si ₂	0.8910		0.8716		8	1.156
Mn ₅ Si ₃	H	Mn ₅ Si ₃	0.6910		0.4814		2	1.00
MnSi	C	FeSi	0.4558				4	4.226
MnSi _{1.73}	T	Mn ₁₁ Si ₁₉	0.5518		4.8136		4	0.2729
		Mn ₁₅ Si ₂₆	0.5531		6.5311		4	
		Mn ₂₇ Si ₄₇	0.5530		11.79		4	
		Mn ₄ Si ₇	0.5525		1.7463		4	0.753

* m_i is the number of formula units per unit cell

** ρ_i is the number density of formula units per unit volume ($10^{22}/\text{cm}^3$)

Table 2-4 Schottky Barrier Height ϕ_{Bo} for MnSi and MnSi_{1.73} on n-type Si

Phases	ϕ_{Bo} (eV)	Reference
MnSi	0.65	[6]
	0.76	[14]
MnSi _{1.73}	0.67	[6]
	0.72	[14]

Table 2-5 Electrical Resistivities of Manganese Silicides

Silicide	Resistivities ρ ($\mu\Omega$ -cm)	Temp. (°K)	Ref.	Remark
Mn ₃ Si	160 \pm 3	293	[1]	
Mn ₅ Si ₃	257 \pm 14	293	[1]	
MnSi	259 \pm 12	293	[1]	
	220	RT	[6]	thin film, polycrystal
MnSi _{1.73}	1073	293	[1]	
	4550	293	[1]	
	1080	RT	[11]	bulk single crystal, along a axis
	5480	RT	[11]	bulk single crystal, along c axis
	4100	RT	[6]	thin film, polycrystal, formed at 595°C/20m
	30500	RT	[6]	thin film, formed at 700°C/30m
	103000	RT	[6]	thin film, formed at 800°C/30m

Table 2-5 Electrical Resistivities of Manganese Silicides

Silicide	Resistivities ρ ($\mu\Omega$-cm)	Temp. (°K)	Ref.	Remark
Mn₃Si	160 ± 3	293	[1]	
Mn₅Si₃	257 ± 14	293	[1]	
MnSi	259 ± 12	293	[1]	
	220	RT	[6]	thin film, polycrystal
MnSi_{1.73}	1073	293	[1]	
	4550	293	[1]	
	1080	RT	[11]	bulk single crystal, along a axis
	5480	RT	[11]	bulk single crystal, along c axis
	4100	RT	[6]	thin film, polycrystal,- formed at 595°C/20m
	30500	RT	[6]	thin film, formed at 700°C/30m
	103000	RT	[6]	thin film, formed at 800°C/30m

Table 2-6 Semiconductor Properties of MnSi_{1.73}

Temp. (°K)	p (cm ⁻³)	n (cm ⁻³)	R _{H0} (cm ³ C ⁻¹)	R _{Hc} (cm ³ C ⁻¹)	Remark	Ref.
1219	17×10 ²¹	15×10 ²¹	0.3		Sc along [100]	[11]
1174	13.3	11.2	0.38		Sc, along [100]	[11]
1128	9.39	7.3	0.59		Sc Along [001]	[11]
1088	7.39	5.23	0.80	0.83	Pc	[12]
1040	6.14	4.06	0.88		Sc along [001]	[11]
1020	6.92	4.84	0.88		Sc along [100]	[11]
1000	5.44	3.28	1.1	1.17	Pc	[12]
970	4.66	2.50	1.3	1.36	Pc	[12]
964	4.03	1.96	1.4		Sc, along [001]	[11] -
952	4.71	2.63	1.2		Sc, along [100]	[11]
910	4.02	1.86	1.6	1.58	Pc	[12]
848	2.2	1.5	2.3	1.7	Tf, Pc	[13]
770	1.7	0.93	3.1	2.4	Tf, Pc	[13]
665	0.78	0.73	7.7	7.4	Tf, Pc	[13]

Sc: Single crystal; Pc: Polycrystal; Tf: Thin film. R_{H0} and R_{Hc} are observed and calculated Hall coefficients respectively.

**Table 2-7a Melting Point or Transformation
Point of Manganese Silicides [5]**

Silicide	Melting or transformation points (°K)	Remark
Mn ₆ Si	1153	peritectic
Mn ₉ Si ₂	1333	
Mn ₃ Si	1303	incongruent
Mn ₅ Si ₃	1558	congruent
MnSi	1548	congruent
MnSi _{1.73}	1425	peritectic

Table 2-7b Thermodynamic Data of Manganese Silicides [5]

Silicide	ΔH_f^0 (kJ/mol.)	ΔS_f^0 (J/mol. °K)	C_p (J/mol.K)
Mn ₃ Si	-137.1	- 11.2±5.98	100.82 + 52.00x10 ⁻³ T - 14.71x10 ⁵ T ⁻²
Mn ₅ Si ₃	-230.74	+22.4 ±11.95	201.1 + 54.13x10 ⁻³ T - 19.56x10 ⁵ T ⁻²
MnSi	- 96.98	- 4.39±3.01	49.32 + 12.75x10 ⁻³ T - 6.40x10 ⁵ T ⁻²
MnSi _{1.73}	-75.62	- 7.83	71.89 + 4.62x10 ⁻³ T - 13.04x10 ⁵ T ⁻²

Table 2-8a Formation Sequence of Transition Metal Silicides With Metal Films On Si Substrates [1, 6, 20, 24]

Near Noble Metal Silicides				Refractory Metal Silicides	
Silicide	Formation Temp. (°C)	Silicide	Formation Temp. (°C)	Silicide	Formation Temp. (°C)
Co ₂ Si	350-500	FeSi	450-550	CrSi ₂	400-475
CoSi	375-500	FeSi ₂	550		
CoSi ₂	550				
Ni ₂ Si	200-350	HfSi	550-700	MoSi ₂	525
NiSi	350-750	HfSi ₂	750		
NiSi ₂	≤ 750				
Pd ₂ Si	100-300	IrSi	400-500	NbSi ₂	650
PdSi	800	IrSi _{1.75}	500-1000		
		IrSi ₃	1000		
Pt ₂ Si	200-500	MnSi	400	TaSi ₂	650
PtSi	300	MnSi ₂	500		
		RhSi	350-425	VSi ₂	600
		Rh ₄ Si ₅	825-850		
		Rh ₃ Si ₄	925		
		TiSi	500	WSi ₂	550
		TiSi ₂	600		
				ZrSi ₂	700

**Table 2-8b. Formation Sequence of Transition Metal Silicides
with Si Films on Metal Substrates [1, 20, 24]**

Near Noble Metal Silicides				Refractory Metal Silicides	
Silicide	Formation Temp. (°C)	Silicide	Formation Temp. (°C)	Silicide	Formation Temp. (°C)
Ni ₂ Si	200-300	FeSi	450-550		
Ni ₅ Si ₂	400	Fe ₃ Si			
Ni ₃ Si	450				
Pd ₂ Si	100-300	RhSi	350-425		
Pd ₃ Si	350	Rh ₂ Si	400		
Pd ₄ Si	400				
Pd ₅ Si	650				
Pt ₂ Si	200-500				
Pt ₃ Si	400				

**Table 2-9. Major Diffusers in Thin Silicide Films
[1,20,23,24,55-61]**

Silicide	Diffuser	Marker	Silicide	Diffuser	Marker
TiSi ₂	Si	Xe, Si	RhSi	Si	Ar
V ₃ Si	V	Xe	Rh ₄ Si ₅	Si	d
VSi ₂	Si	Xe, c	Rh ₃ Si ₄	Si	d
CrSi ₂	Si	Xe, Si	Pd ₂ Si	Pd and Si	O, W
FeSi	Si	Xe	PdSi	Pd and Si	W
Co ₂ Si	Co	W, Si, Xe	TbSi _{1.7}	Si	c, Kr, Ar
CoSi	Si, Co		ErSi _{1.7}	Si	c, Kr, Ar
CoSi ₂	Si, Co		HfSi	Si	Ar, Zr
Ni ₂ Si	Ni	Xe, Si	TaSi ₂	Si	Nb
NiSi	Ni	Xe	WSi ₂	Si	c, Mo, Ge
NiSi ₂	Ni	Xe	Os ₂ Si ₃	Si	c
YSi _{1.7}	Si	Tb, Er, Kr	IrSi	Si	Co, Rh
ZrSi ₂	Si	Si	IrSi _{1.75}	Si	Co, Rh
NbSi ₂	Si	c, V	Pt ₂ Si	Pt	Si
MoSi ₂	Si	c	PtSi	Pt	Si
Rh ₂ Si ₃	Si	W			

c: By analogy from isomorphous silicide studied in the same investigation.

d: Deduced from oxidation experiments.

Table 2-10. Growth Kinetics of Transition Metal Silicides [20, 23]

Diffusion Controlled	Interfacial Controlled	Nucleation Controlled
Co ₂ Si	CrSi ₂	HfSi ₂
CoSi	MoSi ₂	IrSi ₃
FeSi	NiSi ₂	MnSi _{1.73}
HfSi	TaSi ₂	NiSi ₂
IrSi	TiSi ₂	OsSi ₂
IrSi _{1.75}	VSi ₂	PdSi
MnSi	WSi ₂	R.E.Si _{1.7}
Ni ₂ Si		Rh ₄ Si ₅
NiSi		Rh ₃ Si ₄
Os ₂ Si ₃		ZrSi ₂
Pd ₂ Si		
Pt ₂ Si		
PtSi		
RhSi		
Ru ₂ Si ₃		

Table 2-11. Summary of Gösele and Tu's Analysis of Growth Kinetics

	Fig. 2-15a $x_{\beta} < x_{\beta}^*, x_{\gamma} < x_{\gamma}^*$	Fig. 2-15b $x_{\beta} < x_{\beta}^*, x_{\gamma} > x_{\gamma}^*$	Fig. 2-15c $x_{\beta} > x_{\beta}^*, x_{\gamma} < x_{\gamma}^*$
$r = \frac{J_{\beta}}{J_{\gamma}}$	$\frac{\Delta C_{\beta}^{\text{eq}} K_{\beta}^{\text{eff}}}{\Delta C_{\gamma}^{\text{eq}} K_{\gamma}^{\text{eff}}}$	$\frac{\Delta C_{\beta}^{\text{eq}} K_{\beta}^{\text{eff}} x_{\gamma}}{\Delta C_{\gamma}^{\text{eq}} D_{\gamma}^*}$	$\frac{\Delta C_{\beta}^{\text{eq}} D_{\beta}^*}{\Delta C_{\gamma}^{\text{eq}} K_{\gamma}^{\text{eff}} x_{\beta}}$
case I $r < r_1$	$A_{\beta}B$ shrinks $A_{\gamma}B$ grows	$A_{\beta}B$ shrinks, $A_{\gamma}B$ grows, until $r_1 \leq r$	$A_{\beta}B$ shrinks, $A_{\gamma}B$ grows, until $r_1 \leq r$
case II $r_1 < r < r_2$	$A_{\beta}B$ and $A_{\gamma}B$ grow	$A_{\beta}B$ and $A_{\gamma}B$ grow simultaneously until $r_2 = r$	$A_{\beta}B$ and $A_{\gamma}B$ grow simultaneously until $r_1 = r$
case III $r_2 < r$	$A_{\beta}B$ grows $A_{\gamma}B$ shrinks	$A_{\beta}B$ grows, $A_{\gamma}B$ shrinks, until $r \leq r_2$	$A_{\beta}B$ grows, $A_{\gamma}B$ shrinks, until $r \leq r_2$

Fig. 2-1 has been removed due to copyright restriction. Please refer to the literature [7].

Fig. 2-1. Binary Mn-Si phase diagram [7].

Figs. 2-2 and 2-3 have been removed due to copyright restriction. Please refer to the literature [4, 13].

Fig. 2-2. Sketch of the Mn and Si atoms within one-half a unit cell of $\text{Mn}_{15}\text{Si}_{26}$ showing stacking of (a) Mn subcells, (b) Si atom pairs about the central axis, (c) Mn and Si atoms. Solid circles: Mn; open circles: Si [4].

Fig. 2-3. Plot of resistivity vs temperature for $\text{MnSi}_{1.73}$ [13].

**Figs. 2-4a and 2-4b have been removed due to copyright restriction.
Please refer to the literature [1, 20].**

Fig. 2-4a. Schematic of formation sequence of nickel silicides [20].

Fig. 2-4b. Binary Ni-Si phase diagram [1].

Fig. 2-5 has been removed due to copyright restriction. Please refer to the literature [52].

Fig. 2-5. Schematic of the coverage evolution of the reacted overlayer for Ti and Sc metals on Si substrates. The reaction occurs during deposition of the metals at room temperature [52]. ML: monolayer. Θ : thickness of the reacted overlayer.

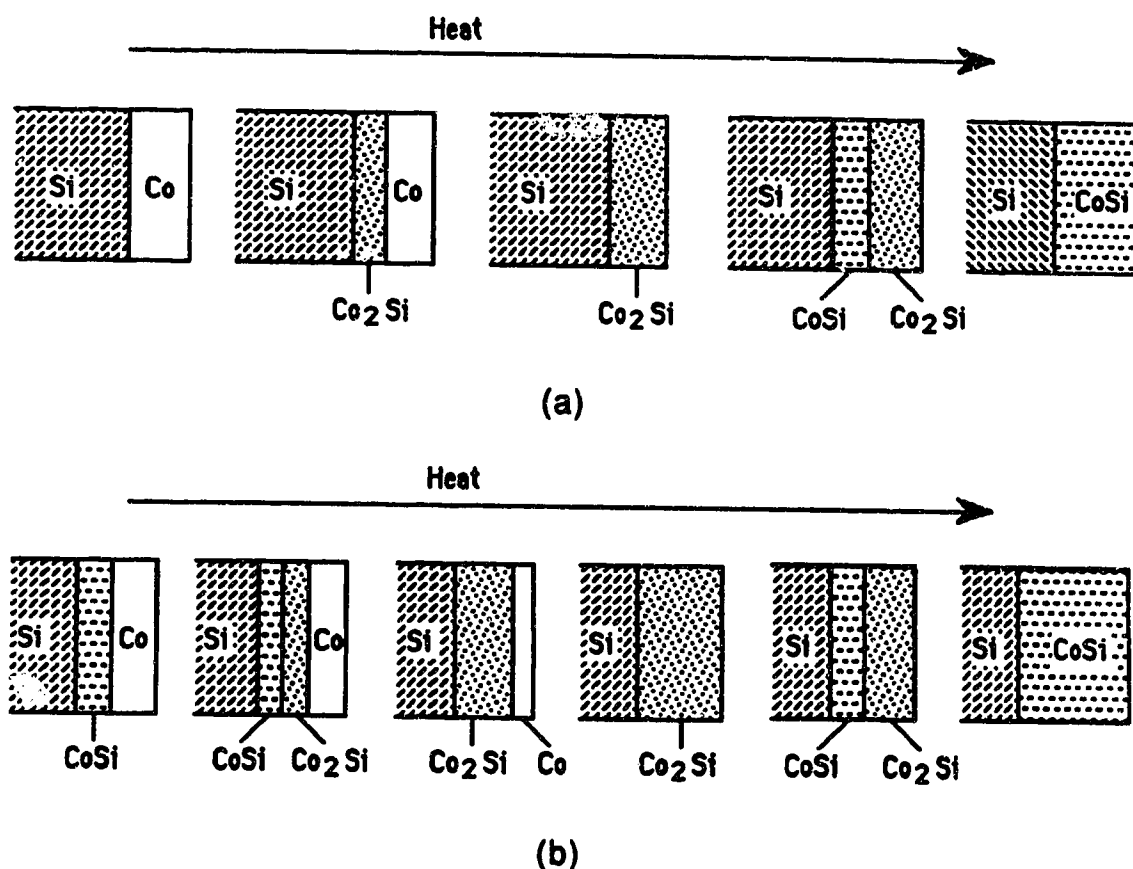


Fig. 2-6. Schematic view of competitive growth during cobalt silicide formation. (a) Co film is deposited on Si substrate. (b) Co is deposited on CoSi which was formed on Si substrate before the deposition.

Figs. 2-7 and 2-8 have been removed due to copyright restriction. Please refer to the literature [24, 45].

Fig. 2-7. Plot of the length of the individual phases vs annealing time at 600°C, showing the phase sequence in the lateral diffusion couples. Two things are noteworthy: 1) In first seven hours, only one phase (Ni_2Si) grows. 2) After Ni_3Si_2 and Ni_5Si_2 formation, Ni_2Si begins to contract [45].

Fig. 2-8. Schematic view of multiple phase growth in thin film couples with relatively thick metal films on Si substrates [24].

Figs. 2-9a and 2-9b have been removed due to copyright restriction. Please refer to the literature [24].

Fig. 2-9a. Effect of an impurity (oxygen) on the formation of platinum silicide. Oxygen diffuses to Pt/Pt₂Si interface, which decreases Pt flux and causes PtSi formation before Pt is completely consumed [24].

Fig. 2-9b. Effect of oxygen on the formation of molybdenum silicide. Oxygen at MoSi₂/Si interface delays Si diffusion, which induces Mo₅Si₃ formation before Mo is totally consumed [24].

Fig. 2-10 has been removed due to copyright restriction. Please refer to the literature [24].

Fig. 2-10. Schematic experimental results of thin film reactions with alloy films on Si substrates. (a) Pt-Cr alloy film on Si. (b) Pt-W alloy film on Si [24].

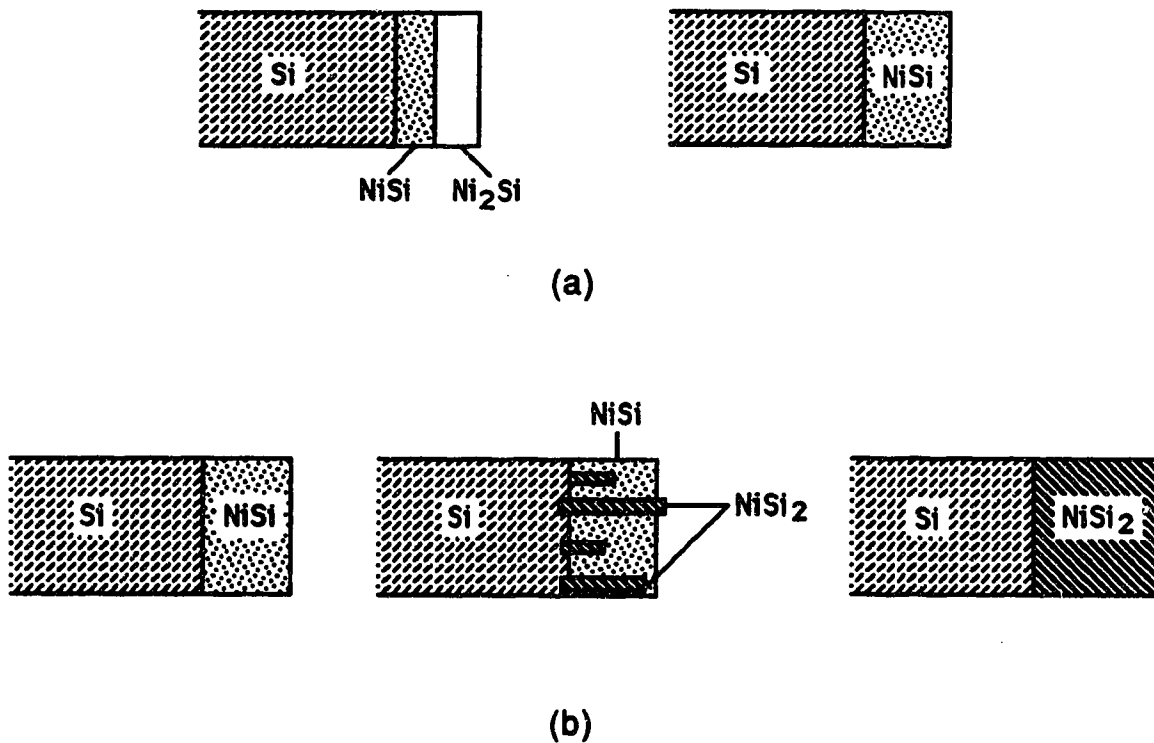


Fig. 2-11. Schematic diagram showing different growth processes. (a) Layered growth (one dimension growth) for diffusion and interfacial reaction controlled processes. (b) Island growth (three dimension growth) for nucleation controlled process.

Figs. 2-12 has been removed due to copyright restriction. Please refer to the literature [37].

Fig. 2-12. Tu and Gösele's diffusion model. Schematic of concentration profiles of A atoms across an $A_\alpha B/A_\beta B/A_\gamma B$ diffusion couple with or without interfacial reaction barriers [37].

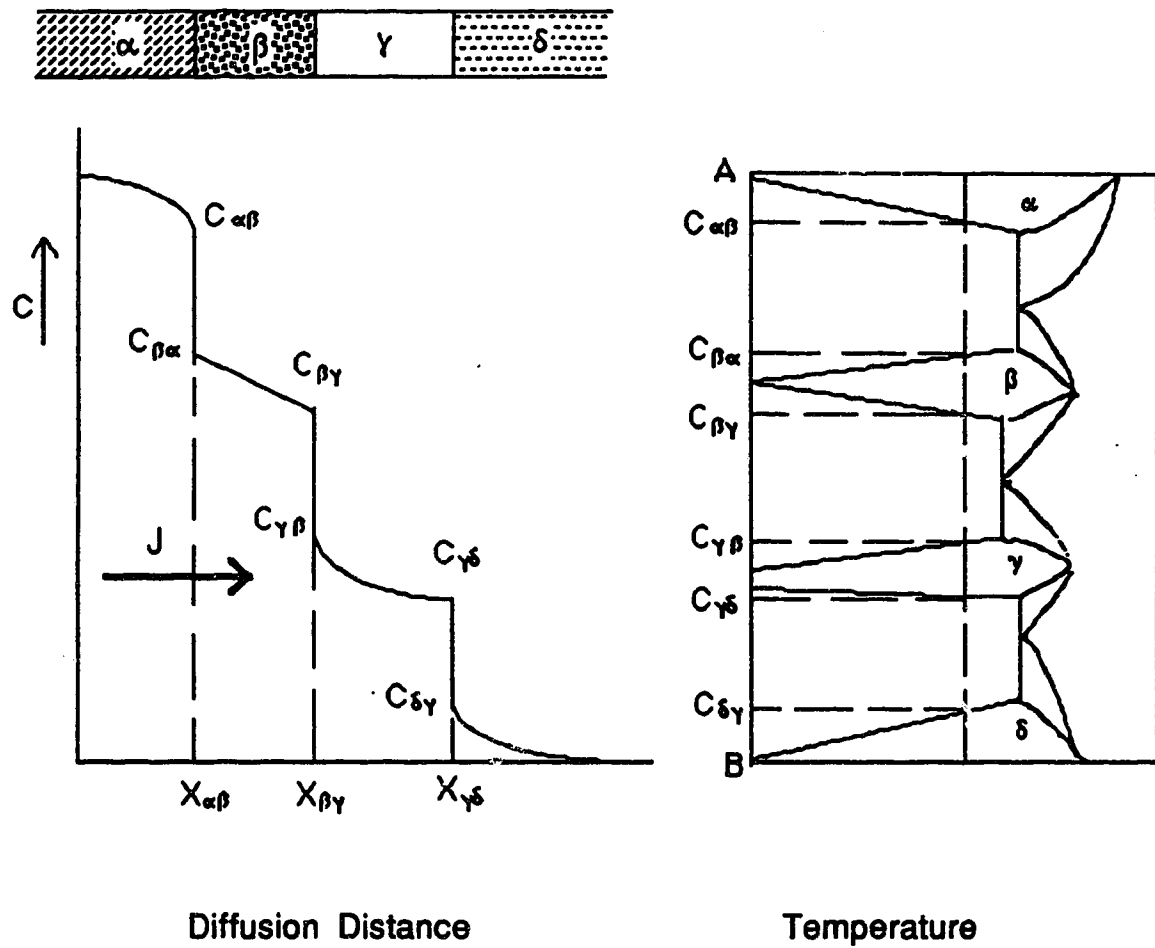


Fig. 2-13. Schematic binary phase diagram and concentration profile of element A during the growth of β and γ phases in a bulk diffusion couple.

Figs. 2-14 has been removed due to copyright restriction. Please refer to the literature [37].

Fig. 2-14. Concentration profile of A atoms in Tu and Gösele's competitive growth model [37].

Figs. 2-15 has been removed due to copyright restriction. Please refer to the literature [37].

(a) (b) (c)

Fig. 2-15. Schematic of growth/shrinkage behavior of the model system (Fig. 2-14) vs time. (a) It is assumed that the transport across both layers ($A_\beta B$ and $A_\gamma B$) is interface reaction controlled, $x_\beta \ll \dot{x}_\beta^*$ and $x_\gamma \ll \dot{x}_\gamma^*$. The flux ratio is independent of the layer thicknesses and is determined by $\kappa_\beta^{\text{eff}}$ and $\kappa_\gamma^{\text{eff}}$. (b) It is assumed that transport across the $A_\gamma B$ layer is diffusion controlled, whereas transport across the $A_\beta B$ layer is interface controlled. At time $t = t_1$, in case III, the growing $A_\gamma B$ layer has reached its critical thickness \dot{x}_γ^c . (c) It is assumed that transport across the $A_\beta B$ layer is diffusion controlled, whereas transport across $A_\gamma B$ layer is interfacial controlled. At time $t = t_2$, in case I, the growing $A_\beta B$ layer has reached its critical thickness \dot{x}_β^c [37].

Figs. 2-16 has been removed due to copyright restriction. Please refer to the literature [24].

Fig. 2-16. Schematic thermodynamic explanation for Ottaviani's model [24].

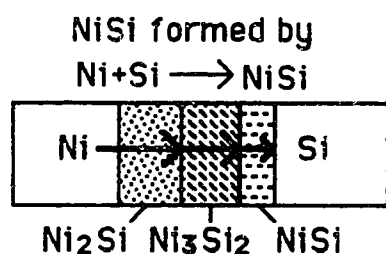
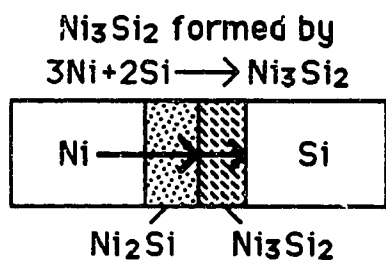
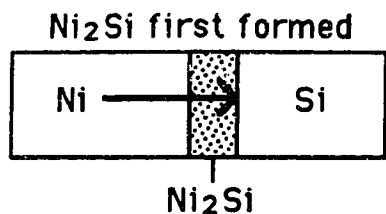
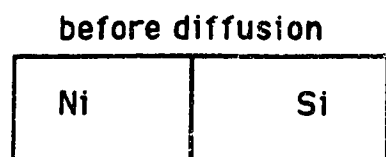
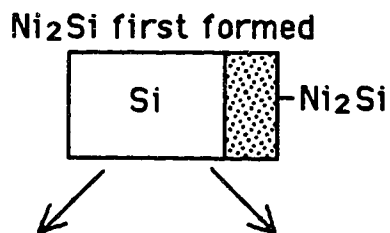
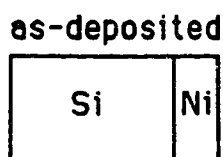
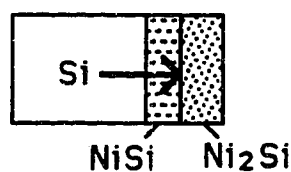


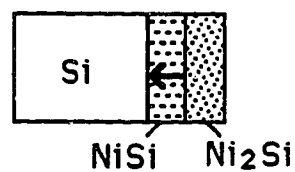
Fig. 2-17a. Schematic growth process in a bulk couple.



NiSi formed by
 $\text{Ni}_2\text{Si} + \text{Si} \rightarrow 2\text{NiSi}$



NiSi formed by
 $\text{Ni}_2\text{Si} \rightarrow \text{NiSi} + \text{Ni}$
 and
 $\text{Ni} + \text{Si} \rightarrow \text{NiSi}$



NiSi growth \rightarrow

NiSi growth in both directions

Fig. 2-17b. Schematic growth in a thin film couple (single layer growth).

Chapter 3. EXPERIMENTAL METHODS

3.1. Deposition of Manganese Films

Manganese was deposited onto Si wafers by thermal evaporation. $\langle 100 \rangle$ oriented, single crystal silicon wafers (n-type with a doping level between 2×10^{15} and $5 \times 10^{15} \text{ cm}^{-3}$), obtained from Alberta Microelectronic Center, and high purity manganese (99.98%), obtained from Chemonics Ltd., were used to prepare the samples. The manganese pieces were crushed into smaller pieces (1 to 2 mm) and loaded into a W boat in a deposition chamber. The silicon wafer was cleaned using buffered hydrofluoric acid (20 part water to 1 part HF), rinsed by deionized water, and dried with high purity Ar. After a Si wafer was loaded into the deposition chamber, the chamber was pumped down to a pressure of 2×10^{-6} Torr. The Mn source was heated, resistively, and evaporated atoms deposited onto the Si substrate, as well as the chamber walls. The thickness of the Mn film was measured using cross-sectional transmission electron microscopy (TEM) of as deposited specimens. The thickness was nominally 300nm.

3.2. Annealing Procedure

After Mn deposition, the Si wafers were cleaved along $\{110\}$ planes, using a diamond knife, into $1\text{cm} \times 1\text{cm}$ pieces and loaded individually into a quartz tube furnace. Annealing was done in

flowing nitrogen (purified nitrogen, 99.97%) at various temperatures. The annealing regime is listed in Table 3-1.

3.3. X-Ray Diffraction Experiments

3.3.1. Equipment

A Rigaku Geigerflex X-ray Diffractometer with a scintillation counter probe and a graphite single crystal monochromator was used to identify the phases in the silicide layers and to monitor the growth of the silicides. A Co target x-ray tube operating at 50 kV and 20 mA was used. The data were collected and recorded by a Digital PDP 11/23 Plus microcomputer system. The data were outputted to a plotter attached to the computer system and were plotted as intensity vs. 2θ , as shown in Fig. 3-1. The scale of the intensity axis was set by the maximum peak height; therefore, intensity information obtained from the plots is expressed in terms of peak heights.

3.3.2. Phase Identification

Phase identification and lattice parameter calculations were accomplished mainly through data from the JCPDS Powder Diffraction Files [78]. The x-ray data from reference [6] were also consulted, due to possible preferred orientations that can be encountered in thin film thermal reactions. Appendix 1 contains the diffraction cards relevant to this experiment, as well as a list of

the three most intense peaks for MnSi and Mn₁₅Si₂₆ from Eizenberg and Tu's results [6].

3.3.3. Monitoring Silicide Growth

The growth of MnSi and Mn₁₅Si₂₆ was monitored by x-ray diffraction experiments from a set of samples with different annealing regimes (see Table 3-1). Two additional silicides (Mn₃Si and Mn₅Si₃) were formed during annealing; their growth could not be monitored by x-ray diffraction methods, however, because some of their diffracted peaks overlapped with those from other phases. Other peaks were too weak for quantitative analysis.

The change in diffracted intensity of MnSi {210} and Mn₁₅Si₂₆ {1 1 30} peaks was monitored. These peaks were chosen because they were the most or second most intense peaks for each phase and because they did not overlap with peaks from other phases.

In order to minimize the experimental error, the following was done:

- 1) All the samples used for x-ray experiments had the same dimensions (1cm × 1cm).

- 2) A standard sample (single crystal silicon) was examined at the same operating conditions as for all other samples each experimental day, since the intensity can change from day to day. A peak from the (400) plane of the standard sample was recorded each day.

- 3) The intensities from MnSi {210} and Mn₁₅Si₂₆ {1 1 30} peaks were normalized using the following formula:

$$I_n = \frac{I_r \times I_s}{I_{se}} \quad (3-1);$$

where I_n is the normalized intensity, I_r is the intensity recorded from MnSi {210} or Mn₁₅Si₂₆ {1 1 30} reflections, I_{se} is the intensity recorded from the standard sample, i.e. the Si (400) peak at the same day as I_r was recorded, and I_s is one of the I_{se} peaks used to normalize all the intensity data.

3.4. Transmission Electron Microscopy (TEM) and Scanning Transmission Electron Microscopy (STEM)

3.4.1. Specimen Preparation

In this experiment, both plan view and cross-section TEM specimens were used. A standard procedure for specimen preparation, including gluing (cross-section specimens only), grinding, disc-cutting, dimpling, and sputtering, was followed. The procedure is described in Appendix 2 in detail. A Gatan ultrasonic disc cutter (Model 601), a Gatan dimple grinder (Model 656), and an ion mill (Ion Tech FAB 306A Atom Mill) were used for disc cutting, dimpling, and sputtering processes respectively during specimen preparation.

Plan view and cross-section specimens were examined by TEM and STEM. The TEMs used in this experiment were a Hitachi H-7000, with an accelerating voltage of 125 kV and a Philips 400 EM, with an accelerating voltage of 120 kV. The models of STEM used were a Hitachi H-600 TEM/STEM equipped with a Be window x-ray detector

and a VG HB5 dedicated STEM equipped with a Link system windowless x-ray detector.

The techniques applied to examine the specimens include bright field imaging, selected area diffraction (SAD), convergent beam electron diffraction (CBED), and energy dispersive x-ray spectroscopy (EDX).

3.4.2. Thickness Measurement Using Micrographs

Bright field images were used to examine the structure of silicide layers formed during the annealing process and to measure the thickness of these layers. The following method was adopted to measure the thickness. For each cross-section specimen, micrographs from three different areas were taken. Layer thicknesses were measured directly on the negatives with a ruler. The initial measuring point was selected randomly and every successive measuring point was chosen at a distance of 10 mm from the last point. Each negative was measured twice with different initial points so that about 30 readings were obtained from each negative and 90 readings from each specimen. Average layer thicknesses, \bar{T} , and standard deviations (σ) were evaluated from these readings (T_i) using the following formulas:

$$\bar{T} = \frac{\sum_{i=1}^n T_i}{n} \quad (3-2),$$

$$\sigma = \frac{\sum_{i=1}^n (\bar{T} - T_i)^2}{n - 1} \quad (3-3);$$

where n is the number of readings from one specimen.

3.4.3. Phase Identification

Since the grain sizes of all the silicides investigated were smaller than 1 μm and some silicide layers were thinner than 100 nm, different techniques, such as selected area diffraction (SAD), convergent beam electron diffraction (CBED), and x-ray spectroscopy (EDX), were combined together to identify the phases.

3.4.3.1. Convergent Beam Electron Diffraction

CBED patterns were obtained from both the H-7000 TEM and the Philips 400 EM. The second condenser lens apertures used were 150 μm in diameter in both cases, while the smallest incident beam size obtained was 300 nm in the H-7000 TEM and 40 nm in the Philips 400 respectively. An internal standard calibration method was adopted to minimize the systematic error. Since the crystal structure of Si is well known and large thin areas of Si were always available in cross-section samples, it was very convenient to use Si as the internal standard sample. Whenever a CBED diffraction pattern from a silicide was taken, a CBED pattern from Si was obtained at the same operating condition. The same method was also

applied to SAD patterns. Therefore, the camera constant could be exactly determined throughout all the experiments.

The CBED patterns were indexed using the following three steps [79, 80]:

1) The zero order Laue zone (zolz) was indexed by the same standard method as that used for indexing SAD patterns. From this information, the possible phase from which the CBED pattern was obtained and the zone axis $[uvw]$ of the pattern was tentatively determined.

2) The radius of first order Laue zone (folz) was measured so that the reciprocal planar spacing (H_m) between the zolz and folz, along the beam direction $[uvw]$, could be obtained from the following formulas [79]:

$$G = \frac{R}{\lambda L} \quad (3-4),$$

$$H_m = \frac{\lambda G^2}{2} \quad (3-5).$$

G is the radius of the folz in reciprocal space, R is the radius of the folz recorded on the negative, λ is the wavelength of the incident beam, and L is the camera length in the TEM.

3) The theoretical value of the reciprocal planar spacing was calculated using the formula below:

$$H_c = \frac{1}{(a^2u^2 + b^2v^2 + c^2w^2)^{1/2}} \quad (3-6)$$

where a , b , c , are the crystal lattice parameters and $[uvw]$ represents the zone axis determined from the CBED pattern. This formula was only applicable to cubic, tetragonal, and orthorhombic systems. If the values of lattice parameters and $[uvw]$, determined from step 1), were inserted into Eq. 3-6, and if the calculated H_c value was equal to $\frac{H_m}{n}$ (where n is 1 or some other integer depending on the crystal structure), the structure of the observed crystal could be verified.

3.4.3.2. Energy Dispersive X-ray Spectroscopy (EDX)

EDX was applied to analyze the compositions in the investigated silicide layers. The composition in a given phase can be determined by the following formula [79]:

$$\frac{X_{Si}}{X_{Mn}} = K_{Mn/Si} \frac{I_{Si} \times W_{Mn}}{I_{Mn} \times W_{Si}} \quad (3-7),$$

where X_{Si} and X_{Mn} are the concentrations (atomic percent) of Si and Mn, W_{Si} and W_{Mn} are the atomic weights of Si and Mn, I_{Si} and I_{Mn} are the intensities from Si and Mn in the EDX spectra from the phase of interest, and $K_{Mn/Si}$ is the proportionality constant, often referred to as the Cliff-Lorimer factor. This factor is independent of specimen composition and thickness, but dependent on instrumental conditions [79].

In this experiment, the factor $K_{Mn/Si}$ was determined by the following method. After annealing a sample at 485°C for 30 min., a

single MnSi layer was formed on the Si substrate. This was verified by x-ray diffraction from a 1cm \times 1cm sample and SAD from a plan view TEM specimen, which was sputtered until only the MnSi layer remained. Several x-ray spectra from this sample were recorded. Assuming $\frac{X_{Si}}{X_{Mn}} = 1$ and inserting I_{Si} and I_{Mn} from the recorded spectra, values of $K_{Mn/Si}$ were calculated. Average $K_{Mn/Si}$ values were obtained as 1.13 ± 0.01 and subsequently used for all other composition analyses.

3.5. Optical Property Measurements

The optical properties of a Mn_4Si_7 thin film were measured using a Cary 2300 UV-Visible-NIR Spectrophotometer. A sample with dimensions 2.5 cm \times 2.5 cm was used. The sample was annealed at 600°C for 90 min. to obtain a single $MnSi_{1.73}$ layer on a silicon wafer. The thickness of the $MnSi_{1.73}$ layer, measured by the cross-sectional TEM technique, was 550 nm.

The change in both transmission and reflection with wavelength was measured. The spectrophotometer was operated in a wavelength scanning mode with an upper wavelength of 2400 nm and a lower wavelength of 1300 nm. The wavelength interval was 1 nm and the scanning rate was 1.0 nm/sec. The data were collected and outputted to a microcomputer system attached to the spectrophotometer.

Table 3-1. Annealing Regimes

Sample No.	Temperatures* (°C)	Periods (Min)
K400-10	380°C	10
K400-40	380°C	40
K400-60	380°C	60
K400-120	380°C	120
K400-210	380°C	210
K425-30	403°C	30
K425-120	403°C	120
K425-185	403°C	185
K450-10	430°C	10
K450-30	430°C	30
K450-60	430°C	60
K500-30	485°C	30
K500-60	485°C	60
K500-90	485°C	90
K500-150	485°C	150
K500-196	485°C	196
K500-256	485°C	256
K550-10	540°C	10
K550-20	540°C	20
K550-30	540°C	30
K585-4	570°C	4
K585-8	570°C	8
K585-16	570°C	16
K600-90	600°C	90

* The temperature error is $\pm 5^{\circ}\text{C}$.

200335 10/13/88 S= 0.050 T= 1.000 MN/SI (ANNEALED)

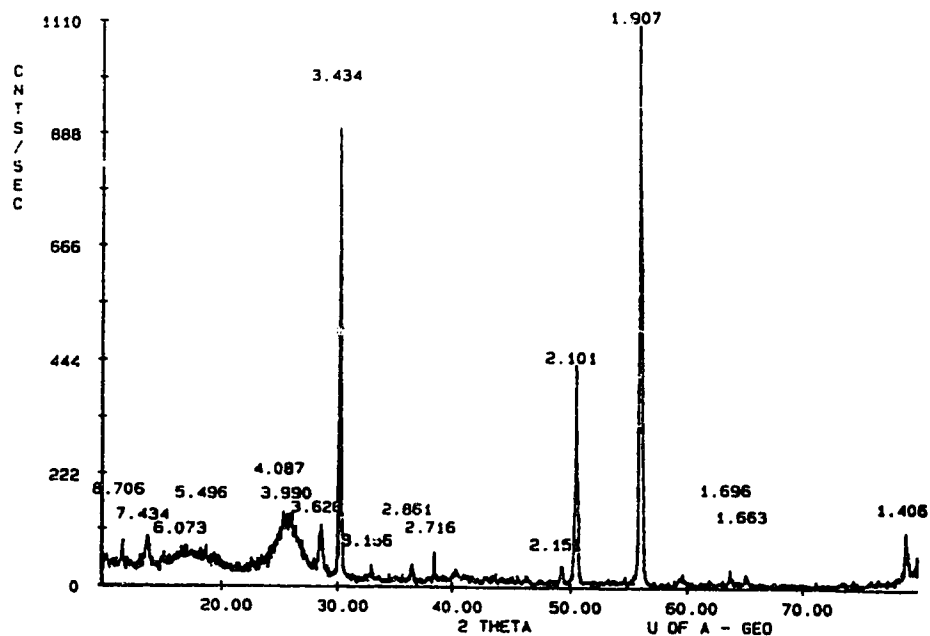


Fig. 3-1. A sample x-ray diffraction pattern from $\text{MnSi}_{1.73}$ (sample was annealed at 1000°C for 60 min.)

Chapter 4. RESULTS

4.1. Interfacial Oxide

Fig. 4-1 shows a cross-section TEM specimen made from the as-deposited sample. At the interface between the Mn layer and the Si substrate there is a thin layer (about 10 nm thick). The microstructure and the composition of this layer have been analyzed using a plan view TEM specimen. This specimen was prepared using a 4% nitric acid solution to remove manganese and by dimpling and ion milling from the silicon side. Fig. 4-2 shows the micrograph and SAD pattern of the thin layer. The diffuse ring pattern from SAD indicates that the structure of this layer is amorphous. Composition analysis by EDX shows that the layer is silicon oxide.

After annealing, the layer still existed, which could be confirmed from Figs. 4-3 and 4-4. The specimens shown in these figures were annealed at 380°C for 10 min. SAD and EDX analysis on the plan view specimen (Fig. 4-4) indicated that this layer was the same as that in the as-deposited sample. Fig. 4-5 is a micrograph from a cross-section specimen annealed at 430°C for 30 min. The oxide still exists but it seems to have recrystallized.

Since this oxide layer separates the deposited Mn layer from the Si substrate before annealing, and since it still exists after annealing, it can play the role of diffusion marker. From Fig. 4-3, it is evident that the Mn is the predominant diffuser in both the oxide layer and the first formed silicide layer (Mn_3Si).

4.2. Annealing Reactions

4.2.1. Phase Identification

Different techniques, such as XRD, SAD, CBED, and EDX, were combined to identify the phases formed during annealing. The procedure for phase identification was as follows: First, annealed samples (1cm × 1cm pieces) were analyzed by XRD. Both plan view and cross-section specimens were prepared from these samples and were examined, in more detail, by TEM and STEM. Fig. 4-6 shows how phases were identified in a cross-section specimen. For grain A, a CBED pattern was taken first and then composition information was collected by EDX.

In this experiment, three phases were identified in low-temperature (380°C to 430°C) annealed samples, i.e. Mn_3Si , Mn_5Si_3 , and MnSi . Two phases were identified in high-temperature (485°C to 570°C) annealed samples. They are MnSi and $\text{MnSi}_{1.73}$. Fig. 4-7 shows typical CBED patterns from all four manganese silicides as well as the zone axes for these patterns. The results of the composition analysis are listed in Table 4-1.

4.2.2. Formation Sequence and Growth Kinetics of Silicides (Low-Temperature Annealing at 380°C to 430°C)

The changes in thickness of the silicide layers were monitored by examining cross-section TEM specimens and XRD. The experimental results are listed in Table 4-2 and 4-3, respectively.

Figs. 4-8a, b, c, and d are micrographs from samples annealed at 380°C for 10, 40, 60 and 120 minutes, respectively. Fig. 4-9a, b, and c show the micrographs from specimens annealed at 430°C for 10, 30, and 60 minutes, respectively. A schematic summary for the formation sequence of the silicides is shown in Fig. 4-10. Mn_3Si forms first at the oxide/Si interface and grows towards the Si substrate. Next, MnSi forms at the Mn_3Si /Si interface and grows towards the surface (to be shown in Section 4.4.1). At the same time, the thickness of the Mn_3Si layer stops changing. Finally, Mn_5Si_3 begins to form and grow at the Mn_3Si / MnSi interface. Mn_5Si_3 grows by consuming Mn_3Si while MnSi grows by consuming Mn_5Si_3 , until all the Mn_3Si as well as Mn_5Si_3 are exhausted and only MnSi is left.

This growth process is unexpected. Thus far, many other types of silicides have been extensively investigated in the literature. Most silicide formation processes follow a single layer growth pattern (see 2.3.1.1). Generally, before the deposited thin metal layer is completely consumed, only one silicide layer exists and grows. After the metal is exhausted, a second silicide begins to grow by consuming the first silicide and so on. Even for a Mn/Si thin film couple system, the silicide formation process reported by Eizenberg and Tu [6] is different from the results observed in this experiment. According to Eizenberg and Tu [6], only one phase, i.e. MnSi , was formed by a single layer growth process during annealing at temperatures between 400 to 500°C. However, in the formation process of manganese silicide observed in this study, three silicide layers co-existed before the Mn layer was used up and at least two

of them grew at the same time. In addition, Mn_5Si_3 formation followed MnSi formation, which is also unusual.

There are two possible explanations for the difference between the results from this study and those from Eizenberg and Tu [6]. One is that Mn_3Si and Mn_5Si_3 were also present in Eizenberg and Tu's samples, but their thicknesses were too small (thinner than 20 nm) to be detected by RBS and XRD. The other explanation is that these two formation processes may be different, i.e. they occur through different mechanisms. No matter which explanation above is true, the formation process of manganese silicides observed in this study is unusual compared to the single layer growth process for most other silicides. The reasons and the mechanisms for these unexpected results will be explained later (see Chapter 5).

In order to determine the kinetics of MnSi growth, the data from thickness measurements (listed in Table 4-2) were plotted against the square root of annealing time (Fig. 4-11a). Usually, if linear, this type of growth process is called diffusion controlled growth. In Fig. 4-11b, the same thickness data were plotted against annealing time. A growth process having this linear relationship implies interfacial reaction controlled growth. By comparing Fig. 4-11a and b, one can find that the data fit both curves.

The data from x-ray diffraction were also used to determine the growth kinetics. These data (in Table 4-3) were plotted as x-ray intensity versus $(\text{annealing time})^{1/2}$ and intensity versus annealing time as well (Fig. 4-12a and b). Again, the data fit both types of curves. A diffusion controlled process is more likely because,

according to experimental observation, MnSi formation has to have an incubation period (Fig. 4-8 and Fig. 4-10).

The activation energy for this process (diffusion controlled process) has been estimated from the data of thickness measurement. The evaluated activation energy is 124 kJ/mol. Again, it was found this value was significantly different from that reported by Eizenberg and Tu [6] (183 kJ/mol). Two factors could be responsible for this difference. One of them is that the value of 124 kJ/mol was evaluated using the data from only two annealing temperatures, which could introduce a relatively large error to the resulting value. The other factor is that the two studied processes, which correspond to the different activation energies, may differ from each other. However, at this time, it is impossible to determine if the latter case is true, due to the difference in experimental conditions and the difference in analysis methods between the two experiments.

4.2.3. Growth Process of $\text{MnSi}_{1.73}$ at High Temperatures (485°C to 570°C)

The growth process for $\text{MnSi}_{1.73}$ was also monitored by XRD. Some of the annealed specimens were also examined by TEM and STEM. The data from XRD are listed in Table 4-4. From this table, it is evident that the growth process is different from that of other manganese silicides appearing at low-temperature annealing. For example, $\text{MnSi}_{1.73}$ did not start to form until the samples were annealed at least one hour at 485°C. Furthermore, TEM showed that

unlike other silicides, $\text{MnSi}_{1.73}$ nucleates and grows in islands instead of a layered growth manner. Fig. 4-13 shows evidence of this different growth process. This micrograph is from a plan view specimen annealed at 485°C for 60 minutes. In this specimen, many islands with big grains were surrounded by larger areas with small grains. From SAD, CBED, and EDX analysis, it can be determined that the small grains are MnSi and the large grains are $\text{MnSi}_{1.73}$. The growth process of $\text{MnSi}_{1.73}$ can be shown schematically in Fig. 4-14. $\text{MnSi}_{1.73}$ nucleated preferentially at some positions on the MnSi/Si interface, and then grew in three dimensions. As mentioned in section 2.3.3.2, this type of growth process is nucleation controlled. The reason that $\text{MnSi}_{1.73}$ follows a nucleation controlled process will be discussed in Chap. 5.

4.3. Calculation of Thermodynamic Quantities

In order to understand and explain the unusual silicide formation process, the calculation of standard Gibbs free energy, ΔG° , has been conducted using the following equations (for example, the reaction $\text{A}+\text{B}=\text{AB}$):

$$\Delta C_p = C_p^{AB} - C_p^A - C_p^B \quad (4-1),$$

$$\Delta H_T^\circ = \Delta H_{298}^\circ + \int_{298}^T \Delta C_p dT \quad (4-2),$$

$$\Delta S_T^{\circ} = \Delta S_{298}^{\circ} + \int_{298}^T \frac{\Delta C_P}{T} dT \quad (4-3),$$

$$\Delta G_T^{\circ} = \Delta H_T^{\circ} - T\Delta S_T^{\circ} \quad (4-4).$$

C_P^{AB} is the heat capacity of the product AB; C_P^A and C_P^B are the heat capacities of the reactants, A and B; ΔH_{298}° and ΔS_{298}° are the standard heat of formation and entropy of formation at 298°C respectively; ΔH_T° , ΔS_T° , and ΔG_T° are the heat of formation, the entropy of formation, and the standard free energy of formation at temperature T. Fortunately, the data for ΔH_{298}° , ΔS_{298}° , and C_P for Mn_3Si , Mn_5Si_3 , $MnSi$, $MnSi_{1.7}$, Si and Mn are available (see Chap. 2 and [5, 81]). The ΔG_T° values for various reactions, involving these silicides during 380°C annealing, have been calculated from the equations above and are listed with their respective reaction equations in Table 4-5.

4.4. Diffusion In Manganese Silicides

4.4.1. Determination of Major Diffusers

As mentioned before, the oxide layer can act as a diffusion marker (see section 4.1). By comparing Fig. 4-1 with Fig. 4-3, it is obvious that Mn_3Si begins to form at the oxide/Si interface and it grows towards Si. This indicates that Mn diffusion predominates in both the oxide and the Mn_3Si phase.

By examining carefully the shape of the interfaces between the silicide phases, one can determine that Si is the major diffuser in the MnSi phase. Evidence supporting this claim is listed below:

1) The MnSi layer (Fig. 4-15) consists of many small columnar grains, and an undulating envelope outlines the interface between MnSi and Si. At this interface, it is notable that neither growth protrusions nor columnar growth can be seen, and that the wavelength of the undulation is longer than the diameters of the columnar grains. These features were present after annealing at different temperatures and longer times. Therefore, the growth of MnSi does not occur at this interface.

2) From Fig. 4-16, it is evident that the shape of the undulation along the MnSi/Si interface follows virtually the same pattern as the $\text{Mn}_3\text{Si}/\text{MnSi}$ interface. According to this observation and (1) above, it is reasonable to assert that this position of MnSi/Si interface is the position of the previous $\text{Mn}_3\text{Si}/\text{Si}$ boundary.

3) At the MnSi/Mn₃Si interface, many tiny protrusions were found from MnSi into Mn₃Si (Fig. 4-17). This indicates that the MnSi growth is taking place at this interface and, hence, that Si diffusion is predominant in MnSi phase.

4) Other indirect support comes from free energy calculations of Mn₅Si₃ formation. Table 4-6 lists possible reactions for Mn₅Si₃ formation at the Mn₃Si/MnSi interface. Of the reactions, only the first reaction is thermodynamically allowed. This reaction requires Si diffusion through MnSi layer. Since the Mn₅Si₃ formation did occur, and since only the reaction that is thermodynamically allowed may actually happen, Si must diffuse through the MnSi layer.

4.4.2. Changes in Diffusion Fluxes

In order to have a better understanding of the growth processes of manganese silicides, the changes in diffusion fluxes have to be taken into account. Since the most important diffusion takes place in the region which includes all the silicides formed during annealing and whose boundaries are the oxide layer and the interface between silicide and Si, we define this region as diffusion region. The average diffusion fluxes of Mn and Si into this region can be estimated by the following method. First, N_i , the number of formula units of the i th silicide layer per unit area (formula units.cm⁻²), is estimated by

$$N_i = T_i \times \rho_i \quad (4-5);$$

where T_i indicates the thickness of i th silicide in a given sample, and ρ_i is the number density, i.e the number of the formula units of i th silicide in a unit volume (formula units.cm⁻³). Secondly, the total atom number of Mn or Si in the diffusion region can be calculated by

$$N_{Mn} = \sum_{i=1}^3 n_{i Mn} N_i \quad (4-6),$$

$$N_{Si} = \sum_{i=1}^3 n_{i Si} N_i \quad (4-7);$$

where N_{Mn} and N_{Si} are the total atom numbers of Mn and Si in the diffusion region (atoms.cm⁻²), $n_{i Mn}$ and $n_{i Si}$ are respectively the atom numbers of Mn and Si in one formula unit of i th silicide. Table 4-7 lists all these calculations for N_i , N_{Mn} , and N_{Si} .

Thirdly, using these data and considering that Mn is the major diffuser in Mn₃Si but Si predominates in MnSi, the average flux of Mn atoms into the diffusion region can be evaluated by following formula:

$$\overline{J}_{Mn} = \frac{N_{Mn(k+1)} - N_{Mn(k)}}{t_{(k+1)} - t_{(k)}} \quad (4-8);$$

where $N_{Mn(k+1)}$ and $N_{Mn(k)}$ are the total numbers of Mn atoms in the diffusion region at certain annealing times (see Table 4-7) and $t_{(k+1)}$ and $t_{(k)}$ indicate the relevant annealing times. Similarly, we have the following formula for Si:

$$\overline{J_{Si}} = \frac{N_{Si(k+1)} - N_{Si(k)}}{t_{(k+1)} - t_{(k)}} \quad (4-9).$$

Table 4-8 lists the calculated results for the samples annealed at 380°C. From these data and Fig. 4-18, it is evident that both $\overline{J_{Mn}}$ and $\overline{J_{Si}}$ decrease, but, $\overline{J_{Mn}}$ decreases faster than $\overline{J_{Si}}$. The change in the diffusion flux \overline{J} have a decisive effect on silicide formation. This will be discussed in Ch. 5.

4.5. Determination of Band Gap Value

The configuration for measuring the reflection (R) and transmission (T) spectra is shown in Fig. 4-19a. It is a $MnSi_{1.73}$ film of complex refractive index $n-ik$ on a Si substrate of complex refractive index n_s-ik_s , surrounded by air of refractive index $n_0=1$. Reflection and transmission spectra measured from this configuration using a Cary 2300 UV-Visible-NIR spectrophotometer are shown in Fig. 4-20a and b, respectively. Theoretically, from these data, the optical constants for $MnSi_{1.73}$, i.e. refractive index, n , and extinction coefficient, k , can be calculated. The absorption coefficient then can be obtained from the following equation

$$\alpha = \frac{4\pi k}{\lambda} \quad (4-10)$$

where α is the absorption coefficient and λ is the wavelength of incident light used in the measurement. The band gap was then determined by plotting α^2 vs E (the photon energy corresponding to λ)

and extrapolating the linear section of the plot to the intercept with the E axis. The value of the interception point, E_g , is the value of the band gap.

However, for the configuration used in this experiment, the effect of multiple internal reflection on the reflection and transmission spectra have to be taken into account. Fig. 4-19b schematically shows this complicated process. The internal multiple reflections make the exact expressions for transmitted and reflected light intensity from this configuration cumbersome and difficult to solve. In order to evaluate the optical constants, a model and an iterating procedure, developed by Brett [82], were adopted in this investigation. This model is suitable to a structure with an absorbing film on a transparent substrate. Although Si is transparent in the range of wavelength used, the absorption of the Si substrate has to be taken into account due to the relatively large thickness of the substrate. Therefore, a modification was introduced to Brett's iterative procedure. After this modification, the equations, which were used in the procedure below, have the following forms:

$$T = \exp\left(-\frac{4\pi kd}{\lambda}\right) \exp\left(-\frac{4\pi k_s d_s}{\lambda}\right) (1-r_o)(1-r)(1-r_s) \quad (4-11),$$

$$R = r_o + \exp\left(-\frac{8\pi kd}{\lambda}\right) \{ (1-r_o)^2 r + \exp\left(-\frac{8\pi k_s d_s}{\lambda}\right) (1-r_o)^2 (1-r)^2 r_s \} \quad (4-12),$$

$$r_o = \frac{(n-1)^2 + k^2}{(n+1)^2 + k^2} \quad (4-13),$$

$$r = \frac{(n - n_s)^2 + (k - k_s)^2}{(n + n_s)^2 + (k + k_s)^2} \quad (4-14).$$

T and R are the measured transmission and reflection respectively; n and k are the refractive index and extinction coefficient of the MnSi_{1.73} film; n_s and k_s are the refractive index and extinction coefficient of the Si substrate; λ is the wavelength of the incident light; r₀, r, and r_s are the reflectivity at each interface indicated in Fig. 4-19a. Modifications to Eq. 4-11 and Eq. 4-12 from Brett's model are shown in Appendix 3. Among these variables, T, R, λ, d, and d_s can be experimentally determined. n_s and k_s must be evaluated using measurements from a bare Si wafer and using the following equations. The derivation of these equations is shown in Appendix 3:

$$r_s = \frac{-(R_s^2 - 2R_s - 1 - T_s^2) + \sqrt{(R_s^2 - 2R_s - 1 - T_s^2)^2 - 4(2 - R_s)R_s}}{2(2 - R_s)} \quad (4-15),$$

$$n_s = \frac{1 + \sqrt{r_s}}{1 - \sqrt{r_s}} \quad (4-16),$$

$$k_s = -\frac{1}{2} \log \left[\frac{R_s - r_s}{R_s^2 + r_s - r_s^2} \right] \times \frac{\lambda}{4\pi d_s} \quad (4-17).$$

R_s and T_s are the reflection and transmission measured from a bare Si sample, which is cut from the same wafer as that for a sample with a $\text{MnSi}_{1.73}$ film. After n_s and k_s are determined, n and k for $\text{MnSi}_{1.73}$ can be determined by the following iterative procedure [82]:

- 1) Measure R , T , and d ;
- 2) Calculate r_s from Eq. 4-15 (λ is known);
- 3) Initialize $r_0 = R$ and $r = 0$;
- 4) Evaluate k using Eq. 4-11;
- 5) Evaluate r_0 using Eq. 4-12;
- 6) Evaluate n using Eq. 4-13 from r_0 and k ;
- 7) Calculate r using Eq. 4-14 from the new n and k values;
- 8) Repeat steps 4) through 7).

Convergence to four figure agreement of successive n and k values was obtained for all the experimental data of $R(\lambda)$, $T(\lambda)$, and λ .

The optical constants of $\text{MnSi}_{1.73}$, i.e. $k(E)$ and $n(E)$, in the photon energy range of $E > 0.7$ eV have been evaluated using this iterative procedure. The optical constants corresponding to the energy range $E < 0.7$ eV can not be evaluated by this method. This is because Brett's model is valid only for absorbing films (i.e. k for the film is large), whereas, from Fig. 20, the $\text{MnSi}_{1.73}$ film is transparent in this photon energy range.

The calculated results of k and n are shown in Fig. 4-21a and b, respectively. From the values of $k(E)$, the absorption coefficient of $\text{MnSi}_{1.73}$, α , was calculated using Eq. 4-10. A plot with α^2 vs photon energy ($E = \frac{hc}{\lambda}$) is shown in Fig. 4-22. In this figure, an extrapolated straight line was obtained by curve fitting the data represented by

the closed squares. It can be seen that the data do not follow a straight line relationship exactly so that the intercepts of the extrapolated line with the energy axis may be in a range, instead of one point. Therefore, the value of band gap determined from this figure is between 0.78 and 0.83 eV. These values are higher than that was reported by Bost and Mahan [16], but still in the range of the values calculated by other researchers (0.4-0.9 eV) [11-14].

It has been found, by direct observation of cross-section TEM specimens, that the thickness of the silicide layer is not uniform due to the polycrystal growth process. The change in thickness, and therefore the non-planar nature of the $\text{MnSi}_{1.73}/\text{Si}$ interface, will affect optical measurements in this experiment. This may be the main reason for a poor curve fit in Fig. 4-22.

Table 4-1. Composition Analysis of Manganese Silicides

	Mn ₃ Si	Mn ₅ Si ₃	MnSi	MnSi _{1.73}
Average atomic ratio of Si to Mn, $\bar{R} = \frac{X_{Si}}{X_{Mn}}$	0.33±0.02	0.60±0.01	1.00±0.01	1.73±0.02
Average concentration of Si, \bar{X}_{Si} (at. %)	0.25±0.01	0.625±0.005	0.50±0.005	0.634±0.005
Average concentration of Mn, \bar{X}_{Mn} (at. %)	0.75±0.01	0.375±0.005	0.50±0.005	0.364±0.005

Table 4-2. Thickness of Silicides in Samples Annealed at Low Temperatures

Temperatures (°C)	Time (min)	Mn ₃ Si (nm)	Mn ₅ Si ₃ (nm)	MnSi (nm)
380 ± 5	10	79 ± 8	0	0
	40	85 ± 8	0	39 ± 4
	60	76 ± 8	7 ± 1	64 ± 7
	120	46 ± 6	19 ± 2	111 ± 13
403 ± 5	30	73 ± 6	22 ± 4	82 ± 10
430 ± 5	10	69 ± 8	14 ± 2	72 ± 7
	30	36 ± 4	26 ± 4	146 ± 13
	60	0	0	230 ± 22

**Table 4-3. X-Ray Diffracted Intensities from
{200} Reflection of MnSi**

Annealing Temperature (°C)	Annealing Time (min)	Intensity (peak height)
380 ± 5	60	44.3
	120	57.4
	210	79.0
403 ± 5	30	58.0
	120	91.3
	185	124.4
430 ± 5	10	68.5
	30	122.6
	60	172.6

**Table 4-4. X-Ray Diffracted Intensities from
{200}MnSi and {1 1 30}MnSi_{1.73} Reflections**

Annealing Temperature (°C)	Annealing Time (min)	XRD Intensities From {200}MnSi	XRD Intensities From {1 1 30}MnSi_{1.73}
485 ± 5	10	276	
	30	276	
	60	233.4	83.7
	90	201.6	98.2
	150	131.9	149.9
	196	74.5	237.5
	256	39.5	271.5
540 ± 5	10	241.5	42.6
	20	186	119.3
	30	118	182
	60		234.6
570 ± 5	5	294.5	51.6
	8	164.7	173.6
	16	75	244

Table 4-5. Reaction Equations and Standard Free Energy for Manganese Silicide Formation (380°C)

Reaction Equations	Standard Free Energy ΔG° (kJ)
$3\text{Mn} + \text{Si} = \text{Mn}_3\text{Si}$	- 130.5
$\text{Mn} + \text{Si} = \text{MnSi}$	- 94.1
$\frac{5}{3}\text{Mn} + \text{Si} = \frac{1}{3}\text{Mn}_5\text{Si}_3$	- 81.8
$\frac{1}{1.7}\text{Mn} + \text{Si} = \frac{1}{1.7}\text{MnSi}_{1.7}$	- 58.6
$\text{Mn}_3\text{Si} + \frac{4}{5}\text{Si} = \frac{3}{5}\text{Mn}_5\text{Si}_3$	- 16.8
$\text{Mn}_3\text{Si} + 2\text{Si} = 3\text{MnSi}$	- 151.7
$\frac{3}{5}\text{Mn}_5\text{Si}_3 + \frac{6}{5}\text{Si} = 3\text{MnSi}$	- 134.8
$\text{Mn}_3\text{Si} = 2\text{Mn} + \text{MnSi}$	+ 36.4
$\text{Mn}_3\text{Si} = \frac{1}{3}\text{Mn}_5\text{Si}_3 + \frac{4}{3}\text{Mn}$	+ 47.5
$\text{Mn}_3\text{Si} + 2\text{MnSi} = \text{Mn}_5\text{Si}_3$	+ 73.1
$\text{Mn}_3\text{Si} + \frac{1}{2}\text{Si} = \frac{1}{2}\text{Mn}_5\text{Si}_3 + \frac{1}{2}\text{Mn}$	+ 7.7

Table 4-6. Calculations of Standard Free Energy for Mn_5Si_3 Formation

$\text{Mn}_3\text{Si} + \frac{4}{5}\text{Si} = \frac{3}{5}\text{Mn}_5\text{Si}_3$	$\Delta G_{653}^\circ = -16.8 \text{ kJ}$
$\text{Mn}_3\text{Si} + \frac{1}{2}\text{Si} = \frac{1}{2}\text{Mn}_5\text{Si}_3 + \frac{1}{2}\text{Mn}$	$\Delta G_{653}^\circ = +7.7 \text{ kJ}$
$\text{Mn}_3\text{Si} + 2\text{MnSi} = \text{Mn}_5\text{Si}_3$	$\Delta G_{653}^\circ = +73.1 \text{ kJ}$
$\text{Mn}_3\text{Si} = \frac{1}{3}\text{Mn}_5\text{Si}_3 + \frac{4}{3}\text{Mn}$	$\Delta G_{653}^\circ = +47.5 \text{ kJ}$

**Table 4-7. The Number of Atoms in Phases
for Samples Annealed at 380°C**

Table 4-7a. Annealed for 10 min.

	Mn₃Si	Total
ρ^* (units/cm³)	2.135×10^{22}	
T (nm)	79	
N_i (units/cm²)	1.69×10^{17}	
N_{Mn} (at./cm²)	5.06×10^{17}	5.06×10^{17}
N_{Si} (at./cm²)	1.69×10^{17}	1.69×10^{17}

Table 4-7b. Annealed for 40min.

	Mn₃Si	MnSi	Total
ρ^* (units/cm³)	2.135×10^{22}	4.226×10^{22}	
T (nm)	85.0	39.0	
N_i (units/cm²)	1.81×10^{17}	1.65×10^{17}	
N_{Mn} (at./cm²)	5.44×10^{17}	1.65×10^{17}	7.09×10^{17}
N_{Si} (at./cm²)	1.81×10^{17}	1.65×10^{17}	3.46×10^{17}

Table 4-7c. Annealed for 60 min.

	Mn ₃ Si	Mn ₅ Si ₃	MnSi	Total
ρ^* (units/cm ³)	2.135×10^{22}	1.00×10^{22}	4.226×10^{22}	
T (nm)	76.0	7.0	64.0	
N_{unit} (units/cm ²)	1.62×10^{17}	7.0×10^{15}	2.70×10^{17}	
N_{Mn} (at./cm ²)	4.87×10^{17}	3.5×10^{16}	2.70×10^{17}	7.92×10^{17}
N_{Si} (at./cm ²)	1.62×10^{17}	2.1×10^{16}	2.70×10^{17}	4.53×10^{17}

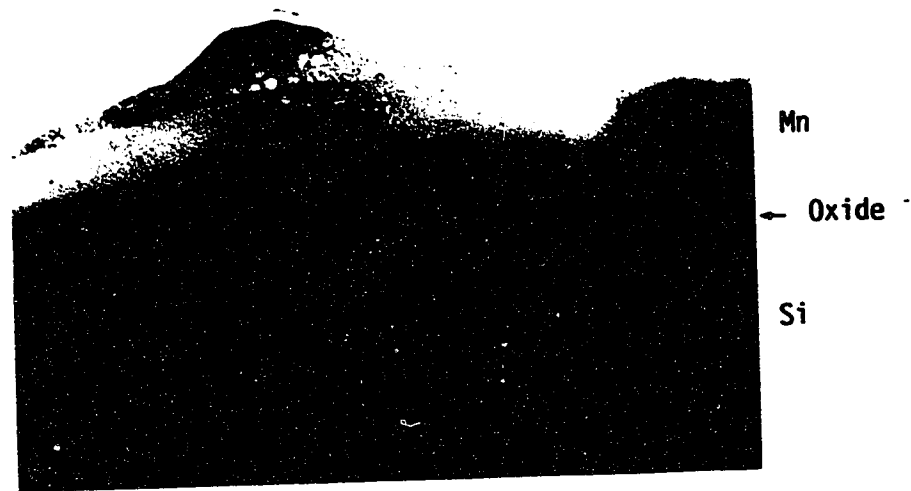
Table 4-7d. Annealed for 120 min

	Mn ₃ Si	Mn ₅ Si ₃	MnSi	Total
ρ^* (units/cm ³)	2.135×10^{22}	1.00×10^{22}	4.226×10^{22}	
T (nm)	46.0	19.0	111.0	
N_{unit} (units/cm ²)	9.82×10^{16}	1.90×10^{16}	4.69×10^{17}	
N_{Mn} (at./cm ²)	2.95×10^{17}	9.50×10^{16}	4.69×10^{17}	8.59×10^{17}
N_{Si} (at./cm ²)	9.82×10^{16}	5.70×10^{16}	4.69×10^{17}	6.24×10^{17}

* Reference [1]

Table 4-8. Average Fluxes of Mn and Si in Diffusion Region

Period (min.)	Δt (s)	J_{Mn} (at./s·cm²)	J_{Si} (at./s·cm²)
0 → 10	600	8.43×10^{14}	
10 → 40	1800	1.13×10^{14}	9.83×10^{13}
40 → 60	1200	6.92×10^{13}	8.9×10^{13}
60 → 120	3600	1.86×10^{13}	4.75×10^{13}



240 nm

Fig. 4-1. TEM micrograph of a cross-section specimen made from the as deposited sample.

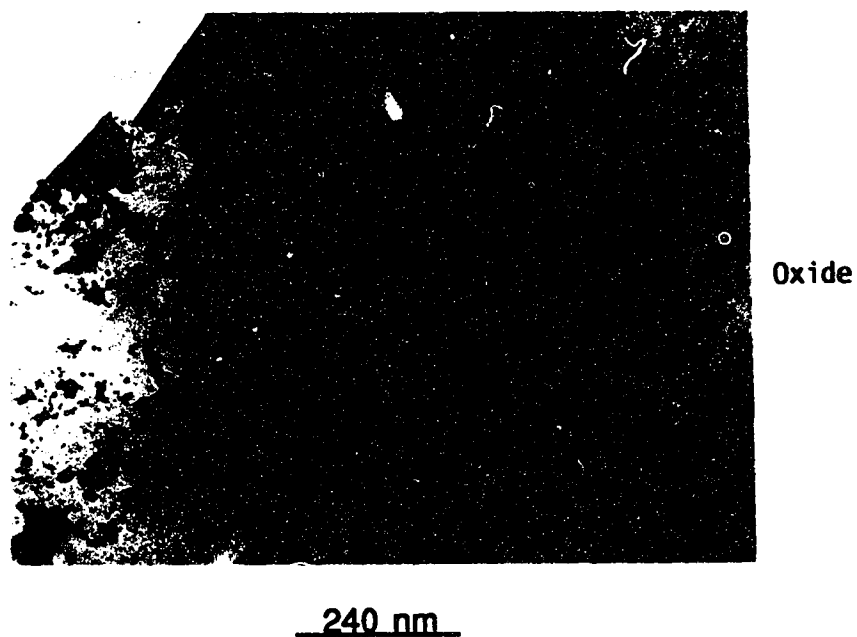


Fig. 4-2a. TEM micrograph of a plan view specimen made from the as-deposited sample (same as the one in Fig. 4-1).

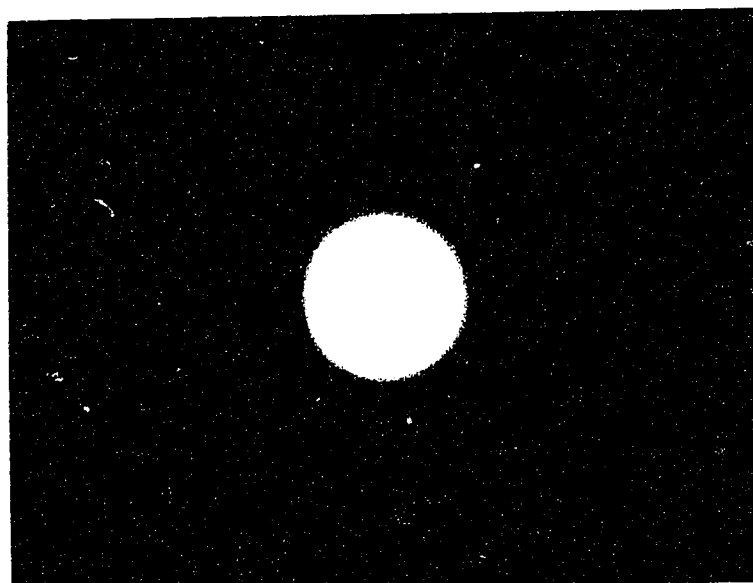


Fig. 4-2b. SAD pattern from the plan view specimen above.

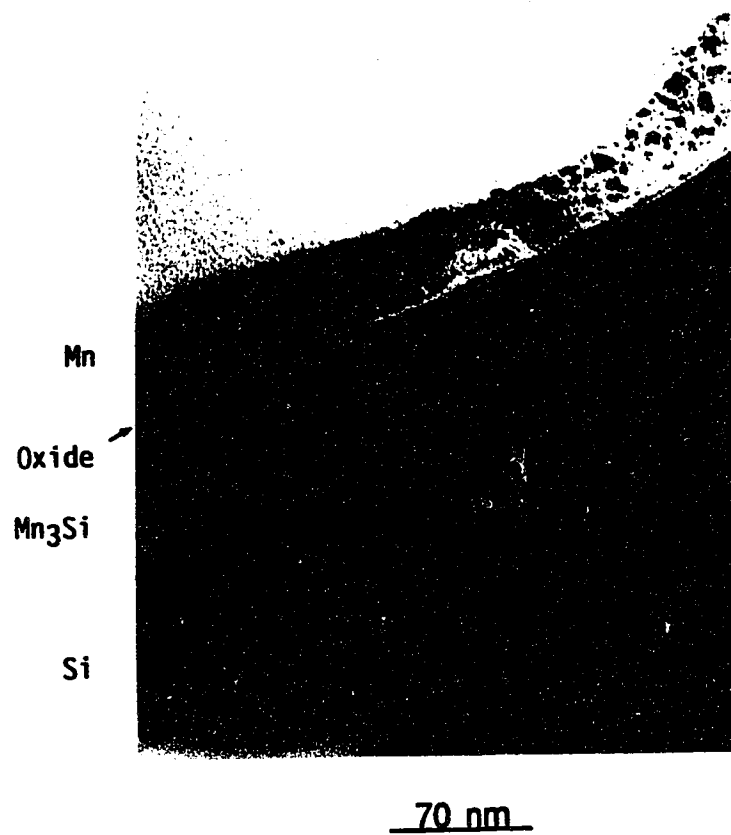


Fig. 4-3. TEM micrograph of a cross-section specimen prepared from the sample annealed at 380°C for 10 min.

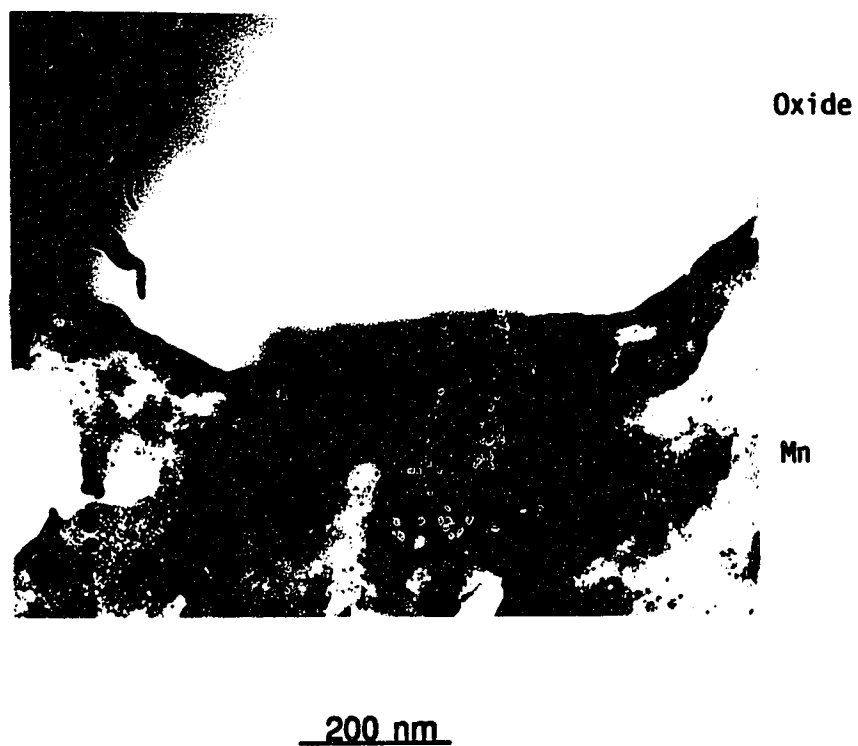


Fig. 4-4. TEM micrograph of a plan view specimen annealed at 380°C for 10 min.

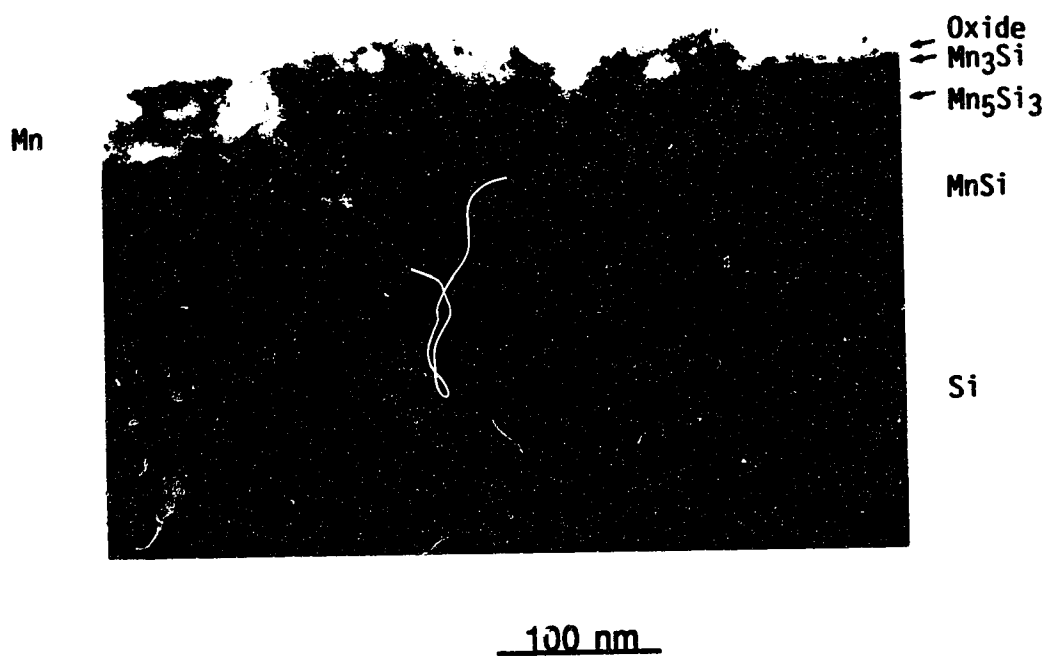


Fig. 4-5. TEM micrograph of a cross-section specimen annealed at 430°C for 30 min.

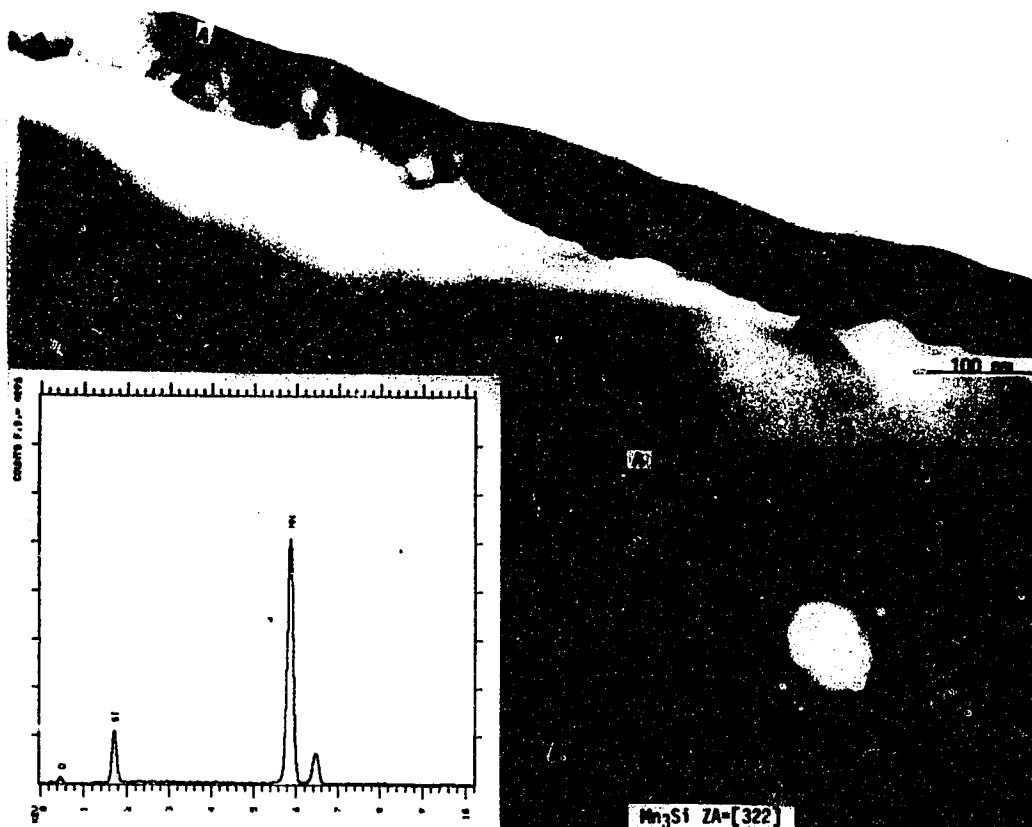


Fig. 4-6. TEM micrograph, EDX pattern, and CBED pattern, showing the method used for phase identification in cross-section specimens.

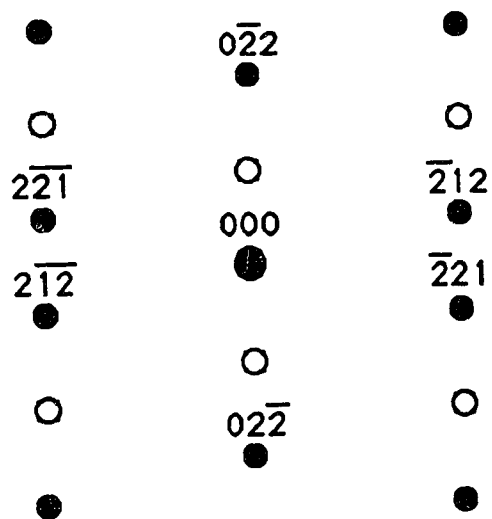


Fig. 4-7a. Indexed CBED pattern from Mn_3Si . Open circles represent double diffraction spots. From Table 2-3, Mn_3Si has a cubic BiF_3 structure and its lattice parameter is $a = 0.5722 \text{ nm}$. This CBED pattern has been indexed as $\text{ZA} = [322]$. $H_c = 0.424 \text{ nm}^{-1}$ and $H_m = 0.408 \text{ nm}^{-1}$.

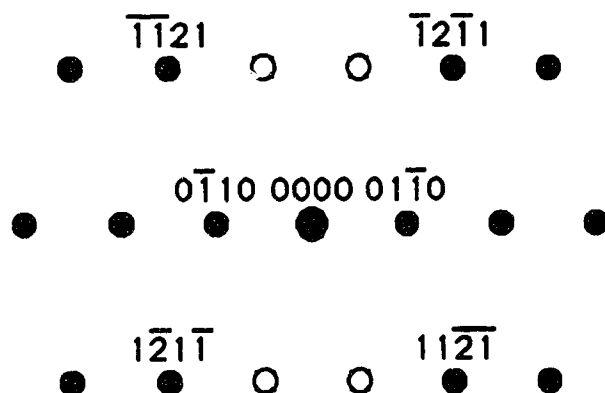
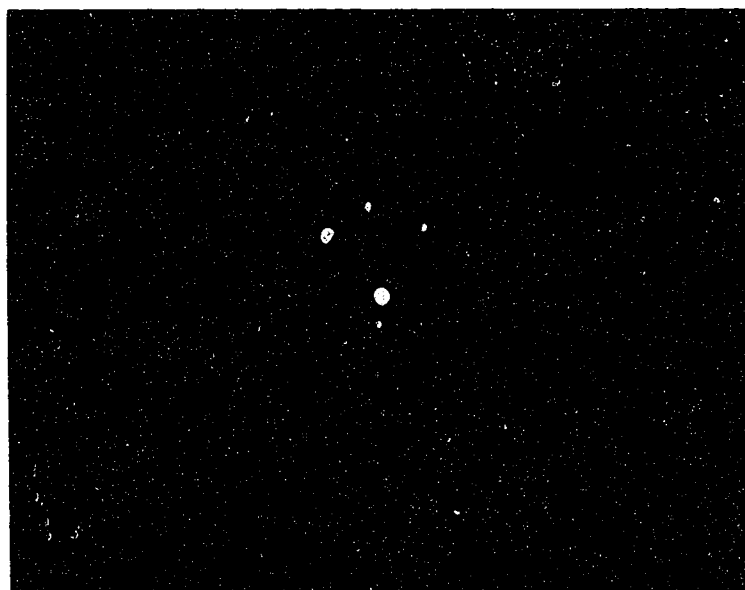


Fig. 4-7b. Indexed CBED pattern from Mn_5Si_3 . Open circles indicate double diffraction. From Table 2-3, Mn_5Si_3 has a hexagonal structure with lattice parameters of $a = 0.691 \text{ nm}$ and $c = 0.481 \text{ nm}$. This CBED pattern has been indexed as $\text{ZA} = [2\bar{1}\bar{1}3]$. $H_c = 1.19 \text{ nm}^{-1}$ and $H_m = 1.16 \text{ nm}^{-1}$.

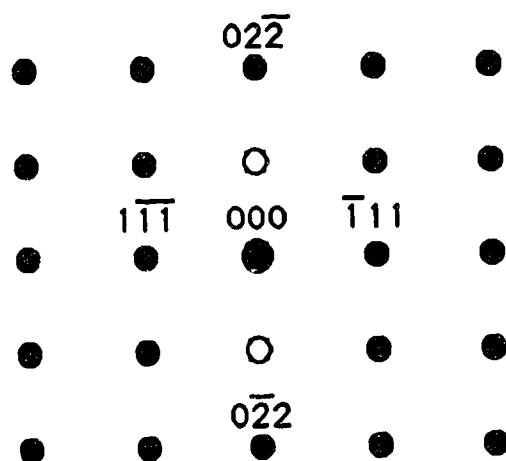
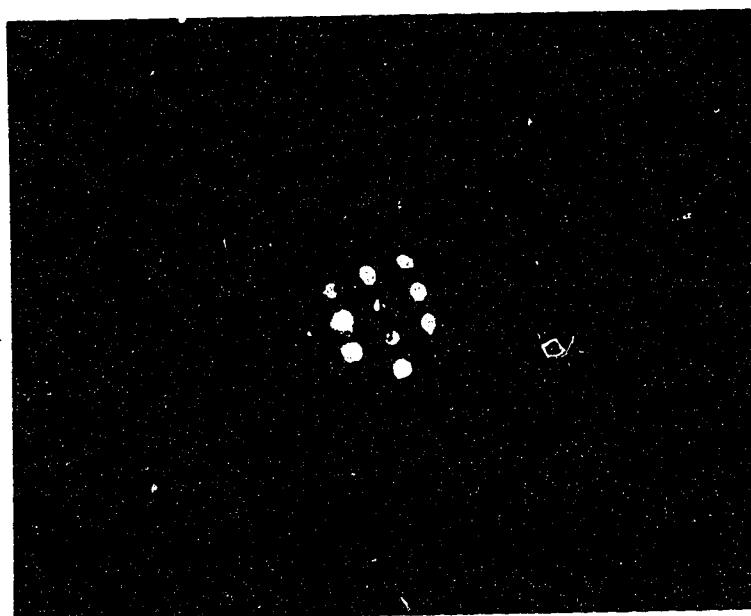


Fig. 4-7c. Indexed CBED patterns from MnSi. Open circles represent double diffraction spots. From Table 2-3, MnSi has a cubic FeSi structure and its lattice parameter is $a = 0.4558 \text{ nm}$. This CBED pattern has been indexed as $ZA = [211]$. $H_c = 0.896 \text{ nm}^{-1}$ and $H_m = 0.842 \text{ nm}^{-1}$.

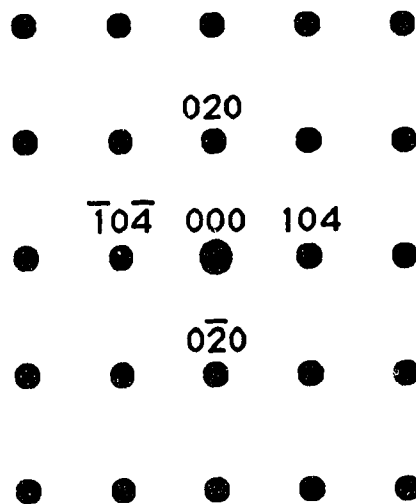
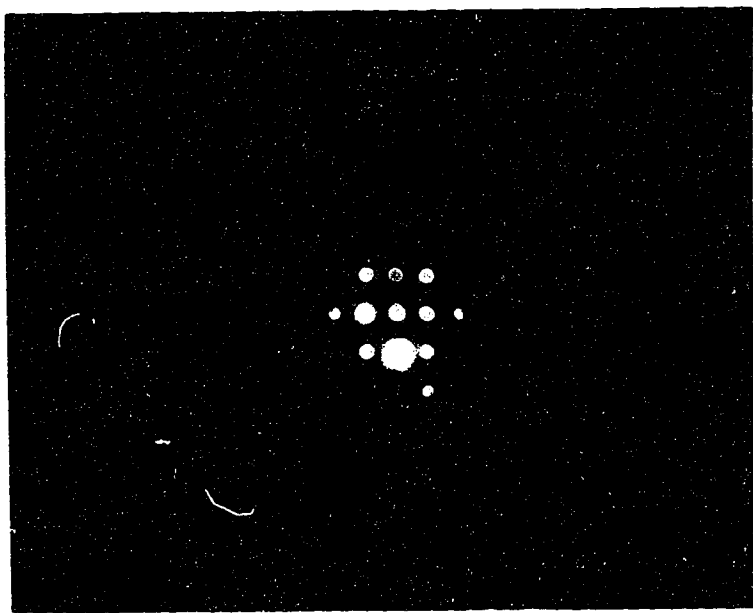
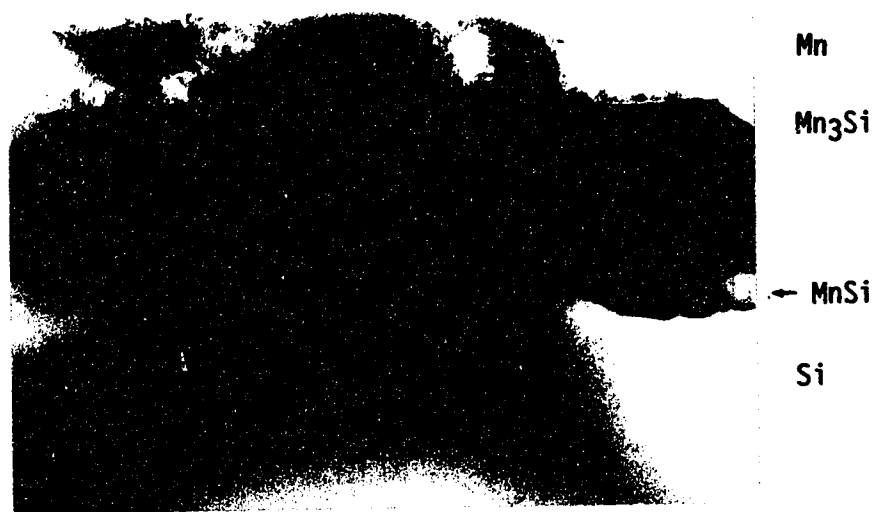


Fig. 4-7d. Indexed CBED patterns from $\text{MnSi}_{1.73}$. From section 2.2. and Table 2-3, different structures for $\text{MnSi}_{1.73}$ have been documented. CBED patterns from the $\text{MnSi}_{1.73}$ examined in this study can match the structure of Mn_4Si_7 best. Its lattice parameters are $a = 0.5525$ and $c = 1.7465$. This CBED pattern has been indexed as $\text{ZA} = [401]$. $H_c = 0.3558 \text{ nm}^{-1}$, and $H_m = 0.6813 \text{ nm}^{-1}$ ($H_m \cong 2H_c$).



(a)



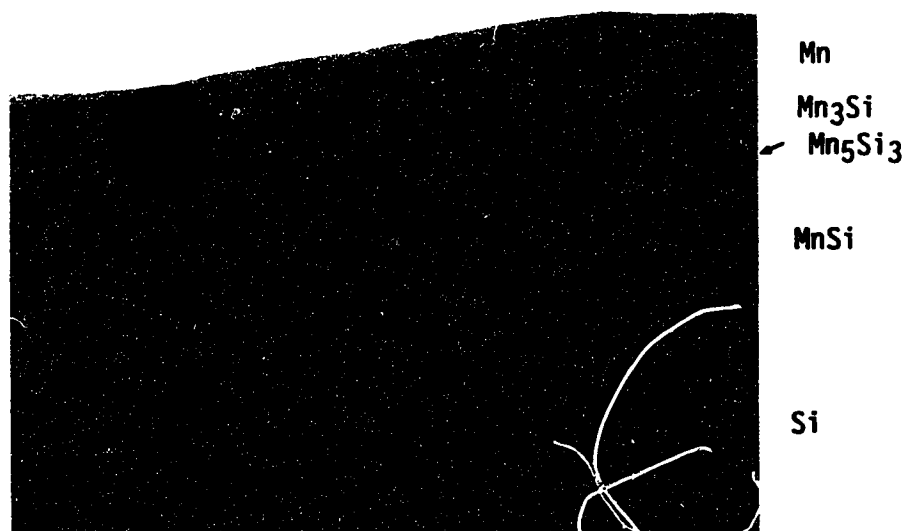
(b)

100 nm

Fig. 4-8a and b. Formation sequence of manganese silicides at 380°C.
(a) Annealing for 10 min. (b) Annealing for 40 min.



(c)



(d)

100 nm

Fig. 4-8c and d. Formation sequence of manganese silicides at 380°C. (c) Annealing for 60 min. (d) Annealing for 120 min.

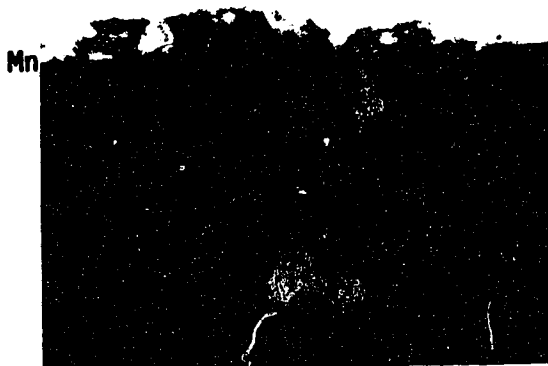
Fig. 4-9. Formation sequence of manganese silicides at 430°C.



Mn_3Si
 MnSi Mn_5Si_3

Si

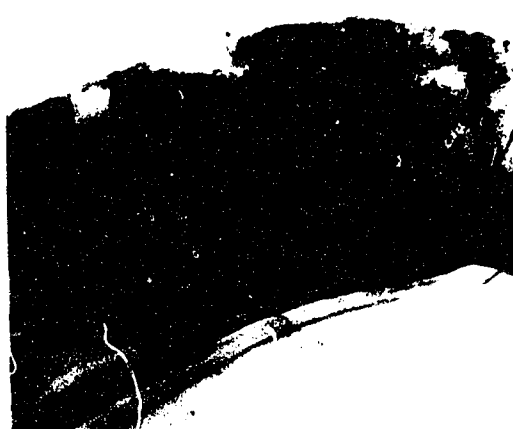
(a) Annealing for 10 min.



Mn_3Si
 Mn_5Si_3
 MnSi

Si

(b) Annealing for 30 min.



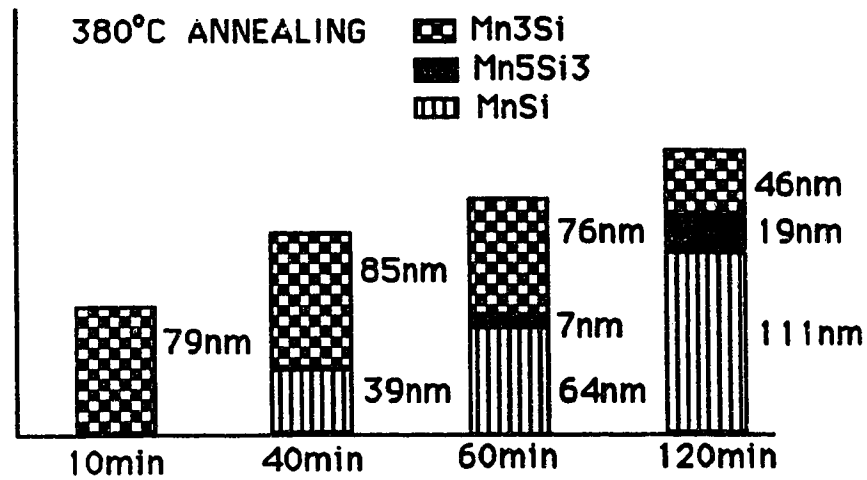
Mn

MnSi

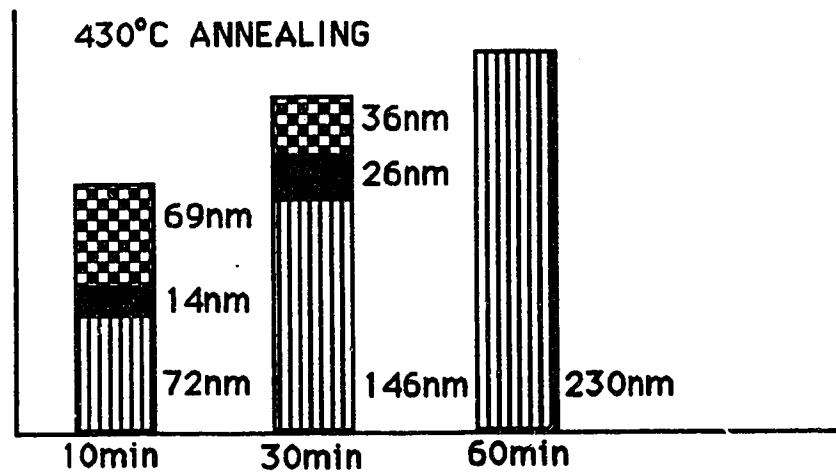
Si

(c) Annealing for 60 min.

200 nm



(a)



(b)

Fig. 4-10. Summary of formation sequence of manganese silicides.

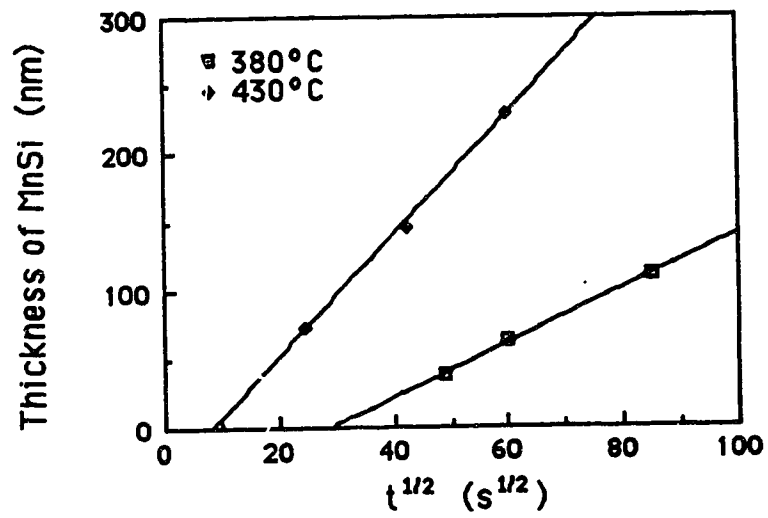


Fig. 4-11a. Plot of thickness of MnSi vs. (annealing time)^{1/2}

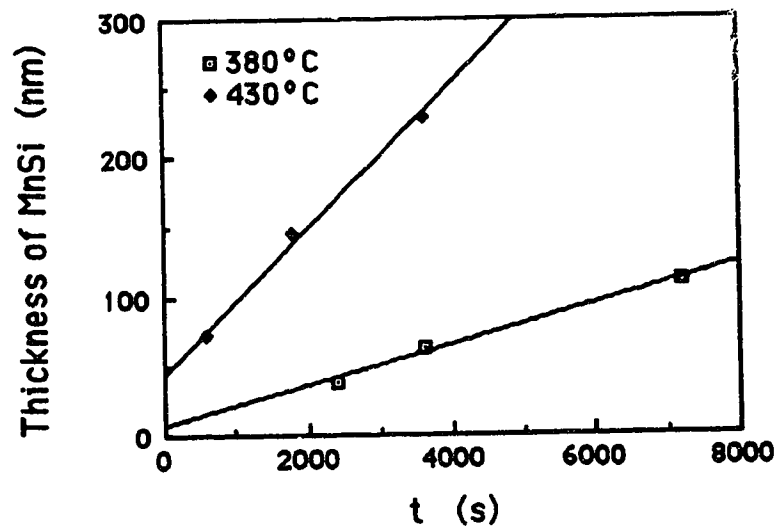


Fig. 4-11b. Plot of thickness of MnSi vs. annealing time.

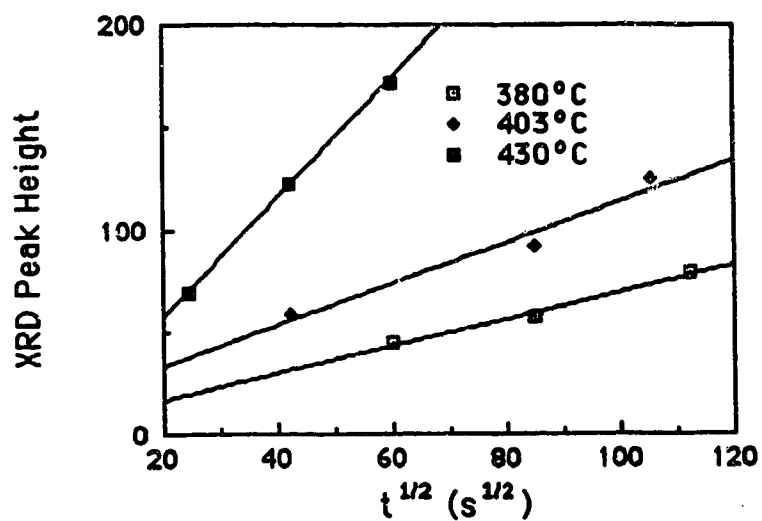


Fig. 4-12a. Plot of X-ray diffraction intensity from {200} reflection of MnSi vs. (annealing time)^{1/2}.

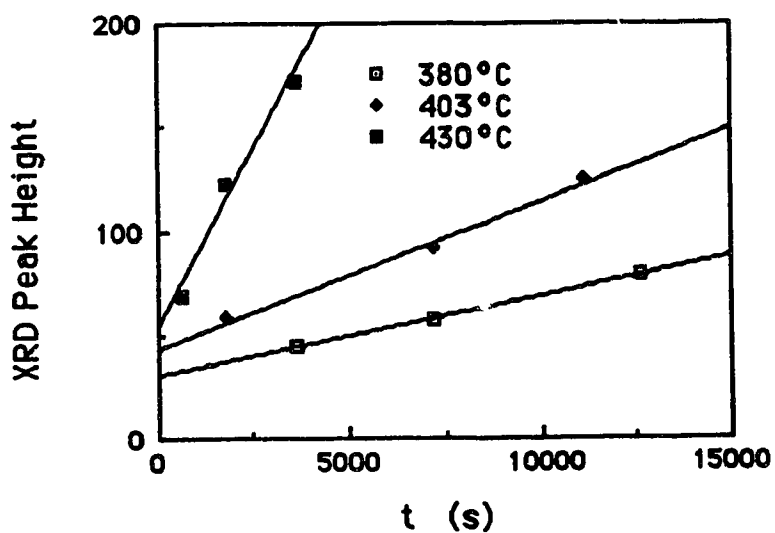


Fig. 4-12b. Plot of x-ray diffraction intensity from {200} reflection of MnSi vs. annealing time.

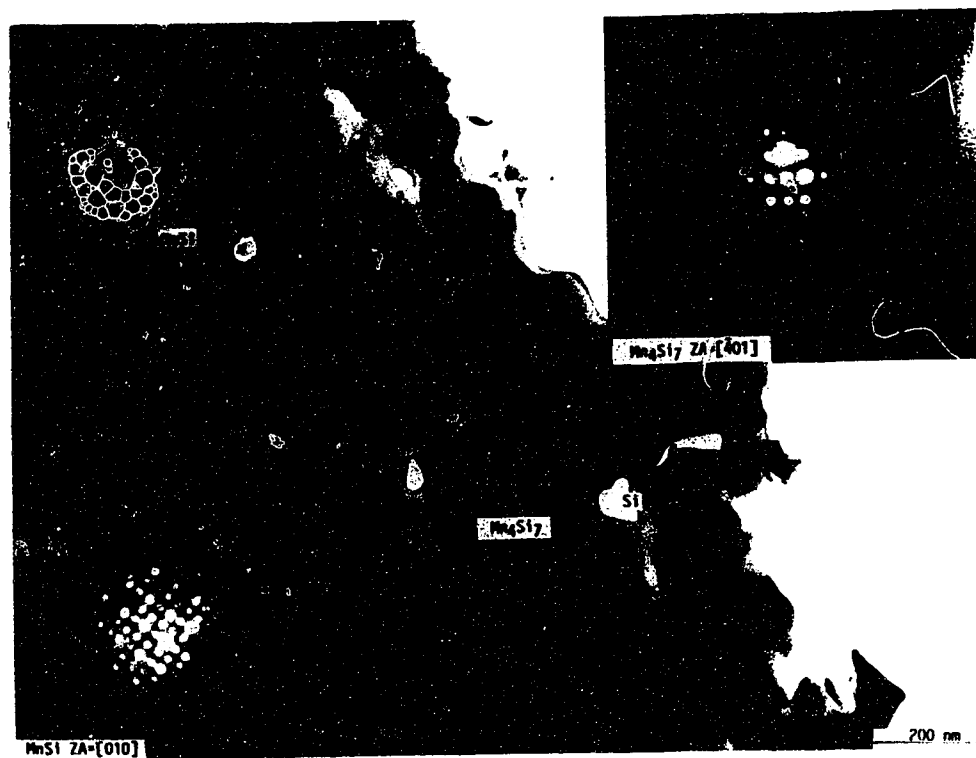


Fig. 4-13. TEM micrograph showing island growth of MnSi_{1.73}. The crystal structure of MnSi_{1.73} matches best with that of Mn₄Si₇.

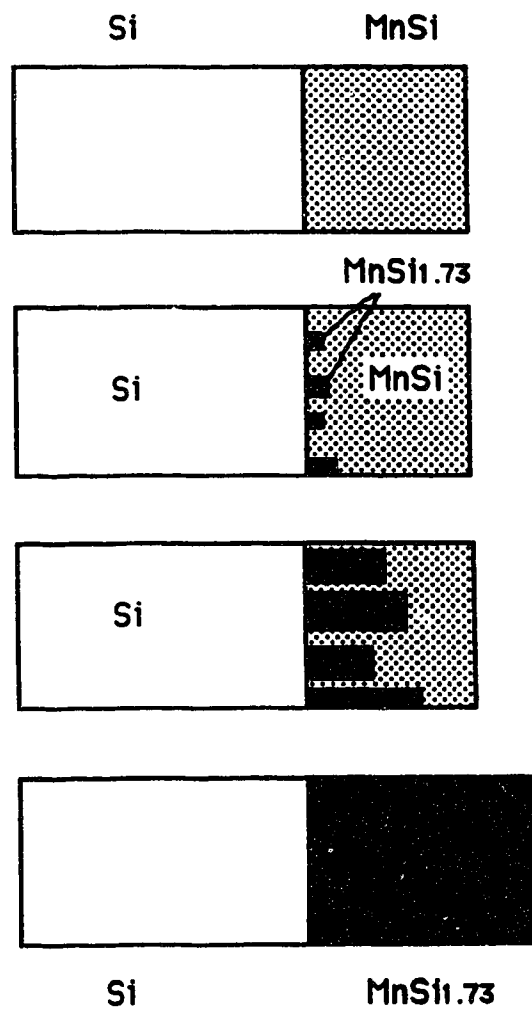
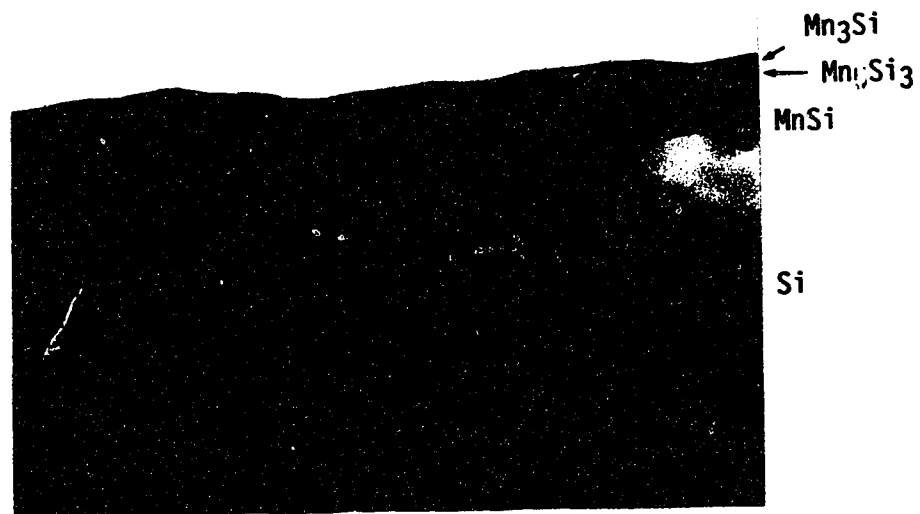


Fig. 4-14. Schematic process of $\text{MnSi}_{1.73}$ nucleation and growth from the interface between Si and MnSi. $\text{MnSi}_{1.73}$ nucleates at some position on the interface and then these nuclei grow in three dimensions.

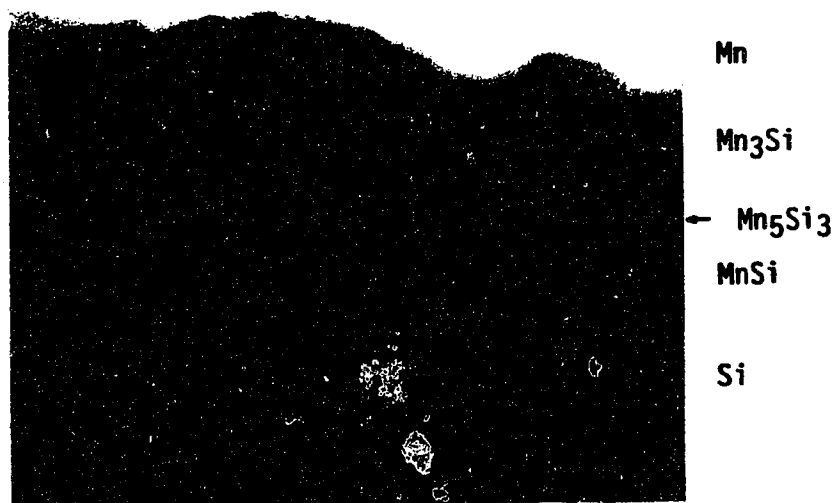


200 nm

Fig. 4-15. Micrograph showing MnSi/Si interface. Neither growth protrusions nor columnar growth can be seen. The wavelength of the undulation along the interface is longer than the diameters of MnSi grains. The specimen is annealed at 430°C for 10 min.



(a)



(b)

100 nm

Fig. 4-16. Micrographs showing the shapes of interfaces. (a) Annealing at 380°C for 40 min. (b) Annealing at 380°C for 60 min. The shape for MnSi/Si interface follows virtually the same pattern as that of Mn₃Si/MnSi interface.



Fig. 4-17. Micrograph showing growth protrusions. The specimen was annealed at 380°C for 40 min. Arrows indicate positions of the protrusions at Mn₃Si/MnSi interface. The protrusions grow toward Mn₃Si.

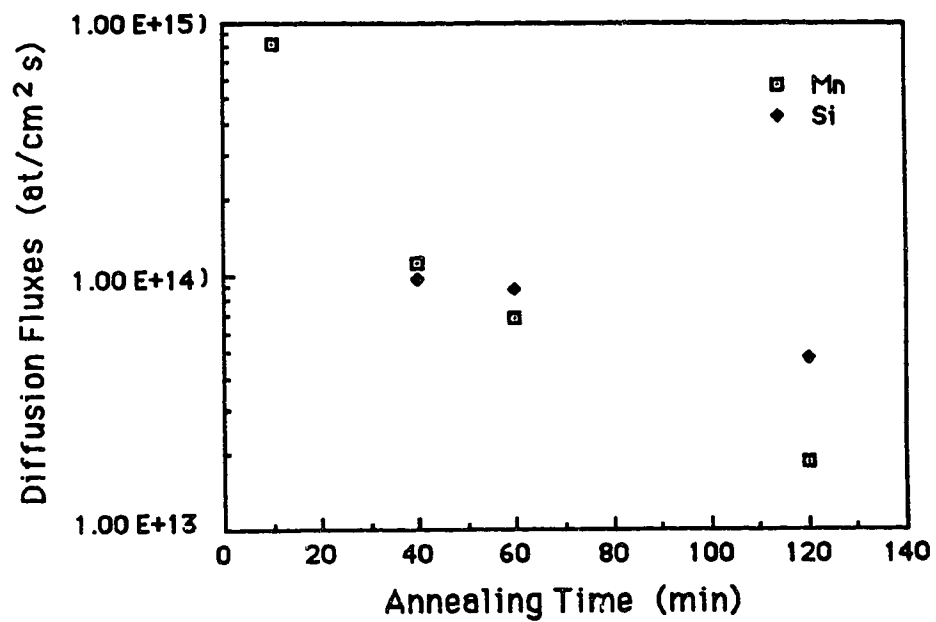


Fig. 4-18. Change in average diffusion fluxes with annealing time. Both fluxes decrease with time, but Mn flux decreases much faster than that of Si.

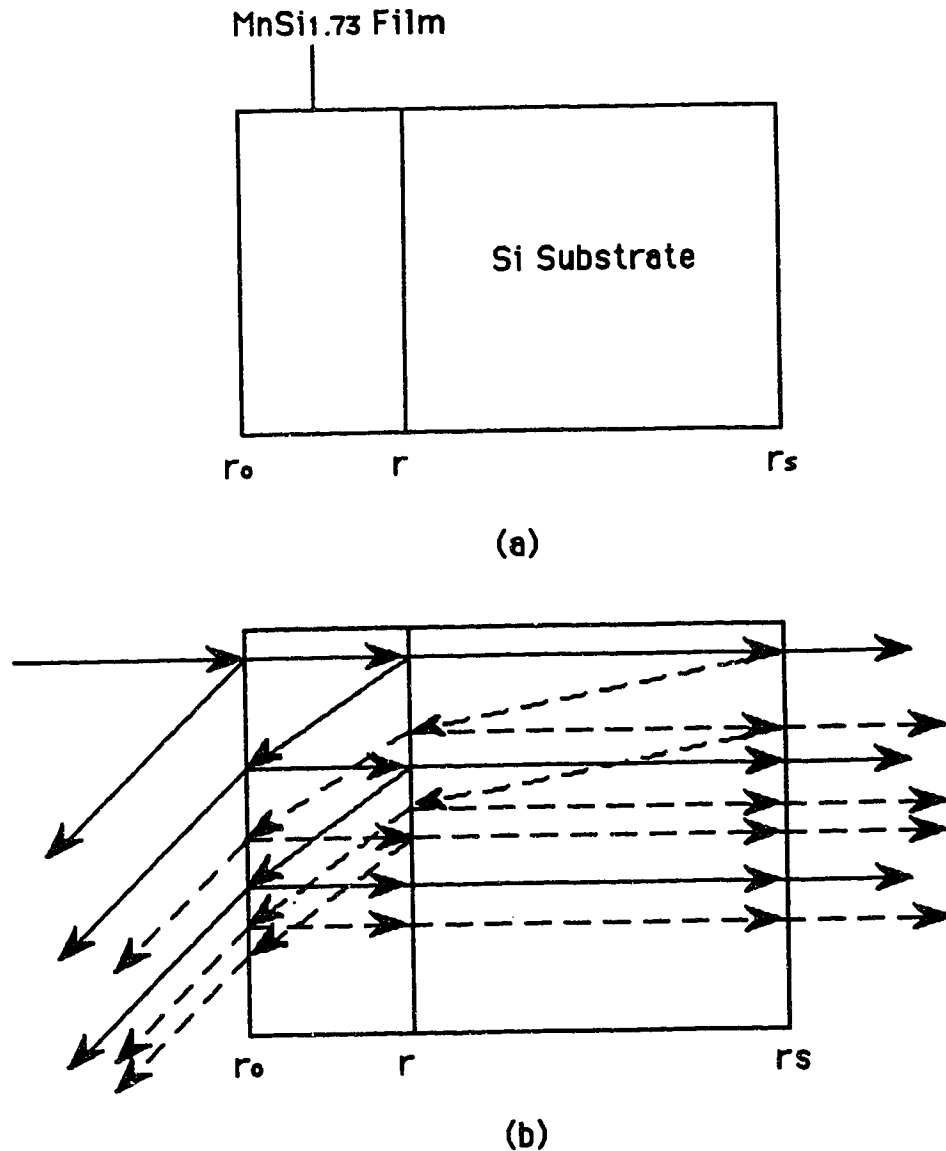


Fig. 4-19. (a) Schematic configuration used in optical property measurements (not to scale). r_0 , r , and r_s are the reflectivities of interfaces air/MnSi_{1.73}, MnSi_{1.73}/Si, and Si/air, respectively. (b) Schematic multiple internal reflections; only first two order reflections are shown. Solid rays represent the reflections involving the multiple reflections in MnSi_{1.73} film only. Dashed rays represents the reflections involving the multiple reflections in both MnSi_{1.73} and Si.

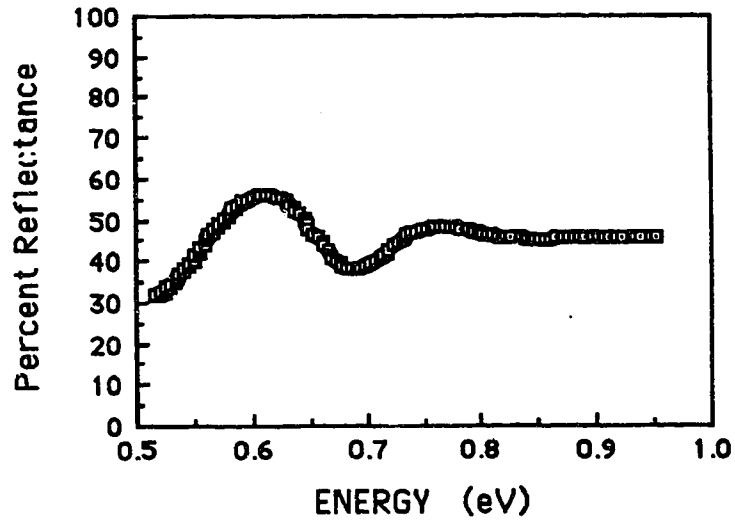


Fig. 4-20a. Plot of percent reflectance vs. photon energy.

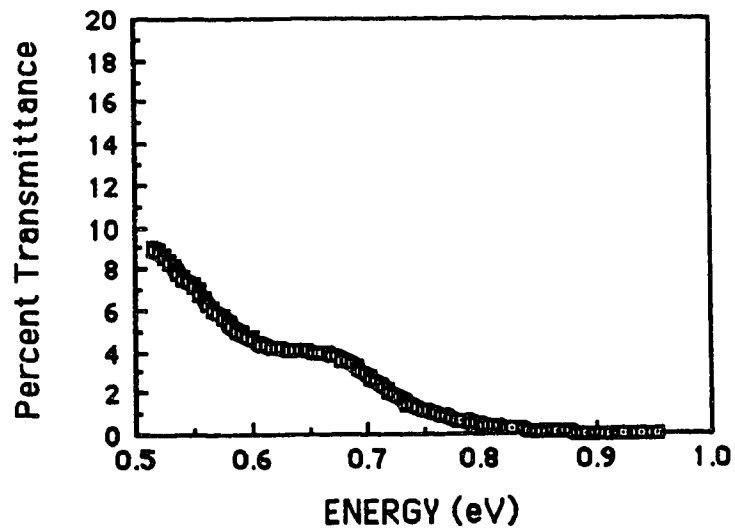


Fig. 4-20b. Plot of percent transmittance vs. photon energy. Both transmittance and reflectance were measured from sample with 550 nm $\text{MnSi}_{1.73}$ film on Si substrate ($400\text{ }\mu\text{m}$).

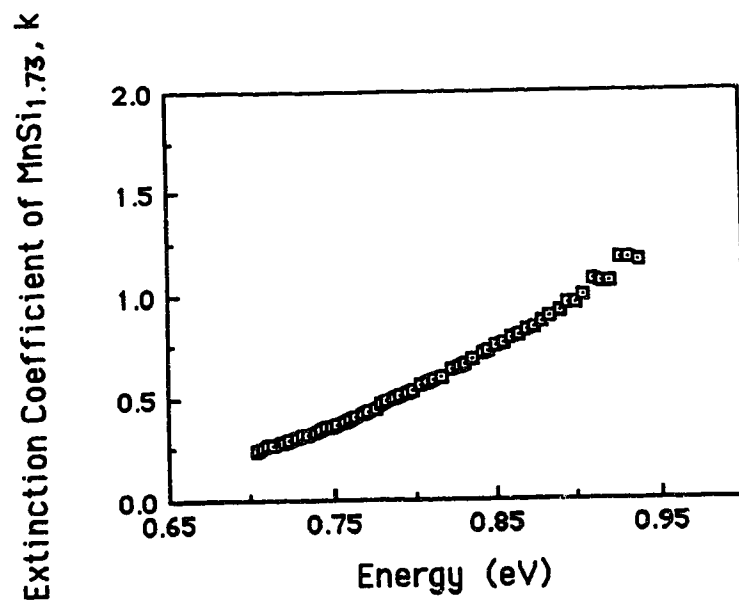


Fig. 4-21a. Plot of extinction coefficient of $\text{MnSi}_{1.73}$ vs. photon energy.

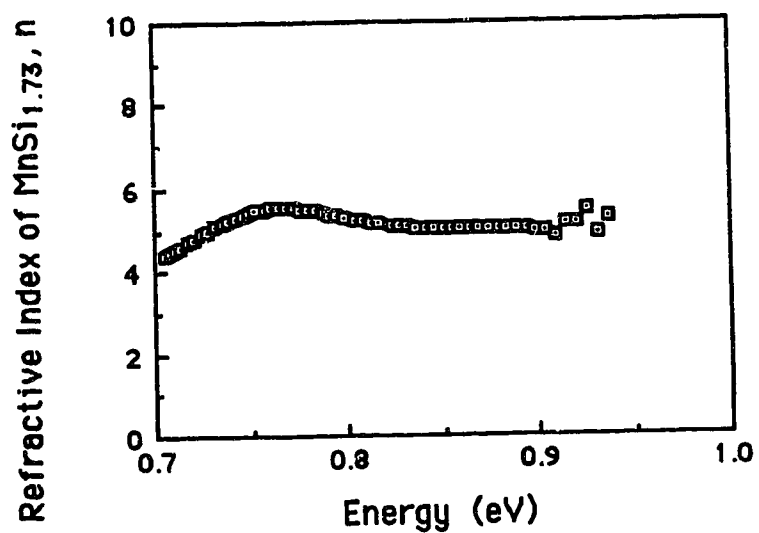


Fig. 4-21b. Plot of refractive index of $\text{MnSi}_{1.73}$ vs. photon energy.

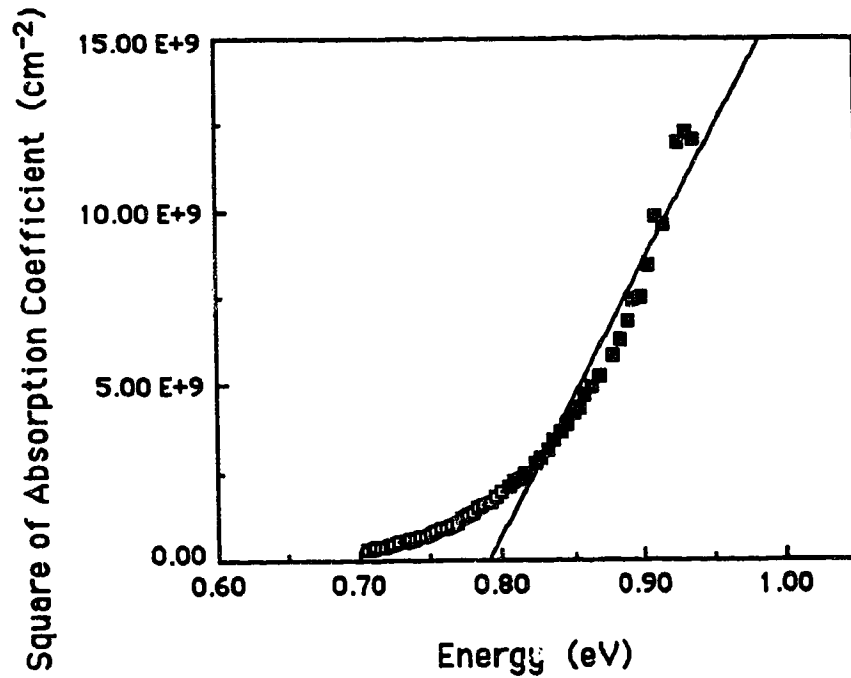


Fig. 4-22. Plot for determination of band gap value of $\text{MnSi}_{1.73}$. Filled squares represent the data points used for curve fitting. The extrapolated intercept of the resulting straight line is around 0.79 eV.

Chapter 5. DISCUSSION

5.1. Mechanisms Of Manganese Silicide Formation

In order to explain the sequence of manganese silicide formation during low temperature annealing, a model has been developed. It is described below:

1) The phase boundary between the growing phase (the product) and contracting phase (the nonmoving reactant) is assumed to be the reaction region (Fig. 5-1).

2) The basic physical process for each reaction can be described as follows: One of the reactants diffuses through the growing phase to arrive at the reaction region and is considered a moving reactant. The other reactant (i.e. the element or compound which makes up the contracting phase) is considered a nonmoving reactant due to its low diffusivity in the growing phase. If the moving reactant does not dissolve in the contracting phase (like the situations met in most silicide formation reactions), some of the nonmoving reactant has to dissolve from its own lattice into reaction region. The two reactants atomically mix together in the reaction region, and then these atoms are rearranged on the lattice of the growing phase.

3) The composition in the reaction region will determine which reaction is kinetically preferred, i.e. the reaction, with its ratio of two reactants closest to that in the reaction region, is kinetically preferred. For example, in reactions



and (2) $nA + mB = pC$.

A is the moving reactant, B is the nonmoving reactant and A does not dissolve in B. Then the equations can be rewritten as

(1) $\frac{a}{b}A + B = \frac{c}{b}C$

and (2) $\frac{n}{m}A + B = \frac{p}{m}C$,

which explicitly indicate that the ratios of reactants A to B are $\frac{a}{b}$ for reaction (1) and $\frac{n}{m}$ for reaction (2). If the composition in the reaction region is $\frac{X_A}{X_B} \approx \frac{n}{m}$ (where X_A and X_B represent the concentrations of A and B in atomic percent), reaction (2) is kinetically preferred. If $\frac{X_A}{X_B} \approx \frac{a}{b}$, then reaction (1) is preferred.

4) Since the amount of dissolved nonmoving atoms in the reaction region is limited, the composition in this region would mainly depend on the diffusivity of the moving reactant. Thus, the faster the moving reactant diffuses, the higher the concentration of moving reactant in the reaction region. Consequently, from 3) above, which reaction will be kinetically preferred is mainly determined by the diffusion of moving reactant.

5) Because the reaction region is essentially an atomic mixture, it is reasonable to apply the thermodynamic criterion for a solution

reaction to the reaction in this region. The criterion is $\Delta G < 0$, where ΔG is Gibbs free energy. For the reaction $\frac{a}{b}A + B = \frac{c}{b}C$,

$$\Delta G = \Delta G^\circ + RT \ln Q \quad (5-1),$$

$$Q = \frac{a_C^{\frac{c}{b}}}{a_A^{\frac{a}{b}} \times a_B} \quad (5-2),$$

where ΔG° is the standard free energy, R is the gas constant, T is the temperature, Q is the activity quotient, and a_A , a_B , and a_C are the activities for each reactant or product, respectively. When reaction equilibrium is established,

$$\Delta G = \Delta G^\circ + RT \ln K = 0 \quad (5-3),$$

where K is the equilibrium constant. Therefore, an alternative equilibrium criterion is $\Delta G^\circ < 0$ and

$$Q = \frac{a_C^{\frac{c}{b}}}{a_A^{\frac{a}{b}} \times a_B} < K \quad (5-4),$$

or

$$\frac{Q}{K} < 1 \quad (5-5).$$

From Eq. (5-3), (5-4), and (5-5), whether a reaction occurs largely depends on the activities. According to assumptions 1) and 2), the reaction region is moving with the growth of the new phase. As soon as, or while, the product is formed, it is rearranged on the lattice of the growing phase. As a result, although reactants are in an atomic mixture, the product is almost in its pure state. For simplicity, then, the activities of the products for all reactions can be approximated as one. The activities of the reactants are influenced by the compositions, the interaction between the components and the annealing temperatures. Under the experimental conditions in this investigation, the change in the interaction is mainly decided by the composition in the reaction region. As a result, the reactant activities and the reaction direction will mostly depend on the composition in the reaction region. Consequently, whether $\frac{Q}{K} < 1$ will mainly depend on the composition in the reaction region, too.

From 4) and 5) above, one can find that, by controlling the composition in the reaction region, diffusion processes can not only determine which reaction is kinetically preferred but they also have important effects on the thermodynamic equilibrium of the reaction.

According to the model described above, some combined criterion are suggested below:

1) If the flux of the moving reactant into the reaction region is constant, and if only one reaction in this region is thermodynamically allowed, this reaction will occur until one of the reactants is completely consumed, or the flux of the moving reactant is changed significantly.

2) If the flux of the moving reactant into the reaction region is kept constant, and if more than one reaction in this region satisfies the thermodynamic criterion, only the reaction, which can best respond to the diffusion flux, will actually occur.

3) If the flux of the moving reactant has changed before one reactant is completely consumed, which has induced a large change in the composition of the reaction region, and if more than one reaction is thermodynamically allowed over the large composition range, the reaction process can be divided into several stages. At different stages, the reaction that occurs may be different. Which reaction actually occurs at each stage can be determined by criterion 1) or 2). In this manner, the reaction sequence can be determined, too.

5.2. Explanation of The Formation Sequence of Manganese Silicides (Low Temperature Annealing)

It has been noted, from the investigation of diffusion phenomena, that the diffusion flux of Mn changed significantly (Fig. 4-18) and hence the composition in the reaction region changed over a large range. According to criterion 3) described above and experimental observation, the manganese silicide formation process can be divided into four stages, i.e. Stage I- Mn_3Si Formation, Stage II- MnSi Formation, Stage III- Mn_5Si_3 Formation, and Stage IV- Phase Transformation From Mn_5Si_3 to MnSi . The reaction process in each stage will be explained below, using the suggested model and criteria.

Stage I. Mn_3Si Formation

At the beginning, Mn diffuses through the oxide layer (Fig. 5-2) to arrive at the oxide/Si interface. Four reactions are thermodynamically possible:



The following facts are important when considering the composition in reaction region:

1) Mn diffuses quite rapidly (see Fig. 4-18). From Table 4-8, the average flux of Mn at Stage I is $8.43 \times 10^{14}/\text{cm}^2\text{s}$.

2) The solubility of Mn in Si is almost zero from the phase diagram of Mn-Si (Fig. 2-1), so that if the mixing process takes place, it must depend on the breaking of silicon bonds.

3) From 1) and 2), if one single Si layer, 0.543 nm thick in an area of 1 cm^2 , is released from the Si lattice into the reaction region, there will be 2.71×10^{15} Si atoms/ cm^2 in the region. In only 10 seconds, this region can reach the composition of Mn_3Si by Mn diffusion.

4) It is not easy to break Si bonds, because of their covalent nature. Thus, the amount of Si in the reaction region is very limited and the concentration of Mn will be much higher than that of Si.

As a result of these facts, the activity of Mn, a_{Mn} , in the reaction region should be close to 1 and must be much larger than that of Si, a_{Si} . The activity quotient for each reaction can be obtained as:

$$Q_a = \frac{1}{a_{Mn}^3 \times a_{Si}} \quad (5-6);$$

$$Q_b = \frac{1}{a_{Mn} \times a_{Si}} \quad (5-7);$$

$$Q_c = \frac{1}{a_{Mn}^{\frac{5}{3}} \times a_{Si}} \quad (5-8);$$

$$Q_d = \frac{1}{a_{Mn}^{\frac{1}{1.7}} \times a_{Si}} \quad (5-9).$$

Since $Q_b/Q_c = (a_{Mn})^{2/3} \approx 1$, $Q_b/Q_d = (a_{Mn})^{-0.7/1.7} \approx 1$ and $Q_a/Q_b = (a_{Mn})^{-2} \approx 1$, Q_a , Q_b , Q_c and Q_d are almost the same. By comparing the equilibrium constants K_i for these four reactions ((a), (b), (c), and (d)) using the formula $\Delta G^\circ \approx -RT \ln K$, it is evident that at 380°C, $K_a \gg K_b > K_c \gg K_d$. As a result, reaction (a) is thermodynamically preferred. In addition, reaction (a) has the highest ratio of Mn atoms to Si atoms, so that of the four possible reactions, only it can best respond to the Mn flux. According to criterion 2), reaction (a) will occur in this stage. After Mn_3Si is first formed, the Mn continues to diffuse through the oxide layer and the growing Mn_3Si layer (Fig. 5-3a). The Mn_3Si/Si interface becomes the reaction region.

Stage II. MnSi Formation.

At the beginning of this stage (Fig. 5-3a), there still are four possible reactions ((a), (b), (c) and (d)). However, the average flux of Mn decreases to $1.13 \times 10^{14}/\text{cm}^2\text{s}$, i.e. only about one eighth of that in stage I. Since the amount of released Si in the reaction region does not change, this implies that the concentration of Mn in this region is decreasing and the concentration of Si is increasing in relative terms. The activities change accordingly.

From formulas (5-6) and (5-8), one would expect the activity quotients Q_a and Q_c to increase rapidly with the change in a_{Mn} and a_{Si} . Eventually the condition will be reached where $Q_a \geq K_a$ and $Q_c \geq K_c$. Under this condition, reaction (a) and (c) can not occur any more.

According to formulas (5-7) and (5-9), one can expect that Q_b and Q_d will decrease with the change in activities. But, since $K_b \gg K_d$, and $Q_b/Q_d = (a_{\text{Mn}})^{-0.7/1.7}$, it can be shown that $\frac{Q_d}{K_d}$ is larger than $\frac{Q_b}{K_b}$, which indicates that reaction (b) is thermodynamically preferred. In addition, reaction (b) has a higher atomic ratio of Mn to Si than reaction (d). This makes reaction (b) respond to the change in diffusion flux better than reaction (d). From criterion 2, reaction (b) will replace reaction (a) in Stage II. As a result, the reaction, $\text{Mn} + \text{Si} = \text{MnSi}$, begins.

As soon as the MnSi layer is formed, Si becomes the major diffuser in MnSi (Fig. 5-3b), which makes the interface region between Mn_3Si and MnSi become the new reaction region. Mn arrives at this region by diffusing through the Mn_3Si layer and Si gets there by diffusing through the MnSi layer. They meet and react with each

other in this region. Therefore, the composition in the reaction region is totally controlled by the two diffusion processes.

Stage III. Mn_5Si_3 Formation

During this stage, $\overline{J_{Mn}}$, the average flux of Mn continues to decrease so that the flux ratio of $\overline{J_{Mn}}$ to $\overline{J_{Si}}$ becomes smaller than 1. The following facts are important:

1) As $\overline{J_{Mn}}$ decreases, the activities will change accordingly to make Q_a and Q_c increase further. Therefore, reactions (a) and (c) are still not allowed by the thermodynamic criterion.

2) A flux ratio smaller than 1 will cause the concentration of the Mn in the reaction region to become smaller than that of Si. Therefore, not all of the Si atoms transported into this region will react with the Mn atoms. Some of them are left in this region. They will diffuse through the reaction region to arrive at the other side of this region next to the Mn_3Si lattice, due to the concentration gradient between the two sides of this region. There, the Si atoms build up and thus a new reaction region (second reaction region) is initialized (Figs. 5-4a and b).

3) There are two reactions in the second reaction region that are thermodynamically feasible. They are:



It is obvious that $K_f \gg K_e$, which implies that reaction (f) is thermodynamically preferred.

4) In the second reaction region, Si is the moving reactant and the Mn_3Si is the nonmoving reactant. Since Si is not soluble in Mn_3Si (from the phase diagram of Mn-Si, see Fig. 2-1), Mn_3Si has to be dissolved from its own lattice into the reaction region. This, according to the suggested model, will limit the amount of Mn_3Si in the reaction region. On the other hand, unlike the Mn flux in stage I and II, the Si flux into the second region is very small at the beginning and will increase gradually. Here, two values for the ratio of the Si to the Mn_3Si are important, i.e. $\frac{4}{5}$ for the reaction (e) and 2 for the reaction (f). Since the concentration of the Si in this region will first increase to a level around $\frac{4}{5}$, and it may take time for Si diffusion to change the concentration to a level around 2, reaction (e) is kinetically preferred.

From these facts and criterion 2, reaction (e) should occur. As soon as Mn_5Si_3 is formed, it lies between the Mn_3Si and MnSi layers (Fig. 5-4c). The two reaction regions are also separated by the Mn_5Si_3 layer. The Mn continues to diffuse through both Mn_3Si and Mn_5Si_3 layers and to react with the Si in first reaction region at the Mn_5Si_3 /MnSi interface. The excess Si, left in reaction region I after the $Mn + Si = MnSi$ reaction, can diffuse through Mn_5Si_3 into the second reaction region at the Mn_5Si_3 / Mn_3Si interface. There, reaction (e) occurs and Mn_5Si_3 grows by consuming Mn_3Si . This process in turn keeps the composition in first reaction region stable, so that MnSi formation can continue at the Mn_5Si_3 /MnSi interface.

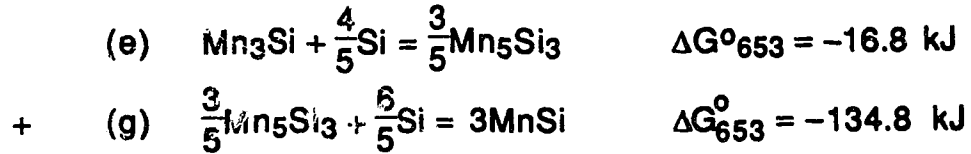
Stage IV. Phase Transformation From Mn₅Si₃ to MnSi

The flux ratio of $\overline{J_{Mn}}$ to $\overline{J_{Si}}$ decreases further (see Table 4-8 and Fig. 4-18). As less and less Mn arrives at the first reaction region at the Mn₅Si₃/MnSi interface (Fig. 5-5a), more and more Si atoms are left in this region after the Mn + Si = MnSi reaction. They will diffuse through the reaction region to arrive at the other side of the region next to the Mn₅Si₃ lattice because of the concentration gradient existing between the two sides of the reaction region. Some of the Si atoms will continue to diffuse into the second reaction region to react with Mn₃Si. The rest of them will build up in front of the Mn₅Si₃ layer (Fig. 5-5b). At this time, only one reaction is both thermodynamically and kinetically allowed, i.e.



From criterion 1, reaction (g), the transformation from the Mn₅Si₃ to the MnSi, will occur, which coincides with reaction (b) (i.e. Mn + Si = MnSi) in the same reaction region. At this point, it is seen that the Mn₃Si layer is contracting while the Mn₅Si₃ layer and the MnSi layer are growing. Actually, the Mn₅Si₃ grows by consuming Mn₃Si while MnSi grows by consuming Mn₅Si₃ as well as by consuming Mn transported to the first reaction region. Both reactions are mainly dependent on Si diffusion. The simultaneous growth phenomenon of two layers is observed because the Mn₃Si/Mn₅Si₃ interface is moving faster than the Mn₅Si₃/MnSi interface.

It is notable that by combining equations for reactions (e) and (g), one gets the same equation as for reaction (f):



This indicates that reaction (f) can not take place in one step due to kinetic limitations. Reaction (f) does occur by two successive steps (reactions (e) and (g)), which are both thermodynamically allowed and kinetically preferred. This provides strong support for the suggested model.

5.3. Comparison of Models

In section 2.3.4, four models for silicide formation through metal/Si thin film reaction were discussed. In this section, the difference between these models and the model suggested in this study will be discussed.

According to Walser and Bene's rule [19], the first phase to form in the Mn/Si system should be Mn_5Si_3 . The rule fails because the experimental results show that the first phase is Mn_3Si . After the formation of Mn_3Si , the next phase to form, from the model of Tsaur et al [21], should be Mn_5Si_3 followed by MnSi . This model fails to predict the right formation sequence for manganese silicides, too. Therefore, Walser and Bene's rule as well as Tsaur et al's model, can not explain the formation process observed in this experiment.

In both of these models, in fact, the effect of interfacial composition on the nucleation of new phases has been considered. The difference between these two models and the one proposed here is discussed below. In Walser and Bene's model, the interfacial composition is previously determined by the deposition of metal and does not change appreciably during the reaction process. In Tsaur et al's model, the concentration profile in the interfacial area does not change at all. Therefore, a common feature of both models is that the effect of diffusion on the interfacial composition and, therefore, on the nucleation and the growth process is ignored. In this model, the interfacial composition will determine which reaction is kinetically preferred and will have an important influence on which reaction is thermodynamically allowed. On the other hand, the interfacial composition is mainly governed by diffusion flux of moving reactant. Thus, the unexpected behavior of manganese silicide formation can be explained as follows: The Mn flux change causes a change in the interfacial composition which, according to the suggested criteria (see section 5.1), "chooses" the next phase to form and, hence, determines the formation sequence of manganese silicides.

In their model, Gösele and Tu [22, 25, 37] have emphasized the effect of diffusion on the silicide formation process, but the model can not explain the manganese silicide formation process very well, either. For example, if one uses the parameter of diffusion flux ratio, r (Eq. 2-30), and assigns Mn as A, β as Mn_3Si , and γ as MnSi , it is evident that

$$r = \frac{J_{\text{Mn}_{\text{Mn}_3\text{Si}}}^{\text{Mn}}}{J_{\text{MnSi}}^{\text{Mn}}} \gg r_2 ,$$

because the diffusion flux of Mn in MnSi is quite small (see section 4.4.2, Si is the major diffuser in MnSi). From Table 2-11 and Fig. 2-15, this condition should result in Mn₃Si growth and MnSi shrinkage. This prediction from Gösele and Tu's theory is just opposite to experiment observations, i.e. Mn₃Si stops growing and MnSi grows (see 4.2.2). The failure of Gösele and Tu's model lies in that the model does not consider the key effect of interfacial composition and the possibility of changing the moving reactant from one element to another element during new phase formation.

In some sense, Ottaviani's model [24] is similar to the present model. For instance, both models emphasize the key effect of interfacial composition on the silicide formation sequence, and the composition is, in turn, mainly controlled by diffusion. In Ottaviani's model, as in my model, the thermodynamic criterion, $\Delta G < 0$, is also applied to the interfacial reaction. However, the differences between the two models are significant.

Firstly, in Ottaviani's model, the relation between diffusion and interfacial composition is not clear. In the present model, the terms of moving reactant and nonmoving reactant are introduced, which is helpful when inferring which reaction is kinetically preferred (see, for example, section 5.2, explanation for Stage II-MnSi formation and Stage III-Mn₅Si₃ formation).

Secondly, an important consideration in this model is that the moving reactant can switch from one element to another (such as Mn

during Mn_3Si formation and Si during MnSi formation). The change in moving reactant can cause a change in kinetic and thermodynamic conditions for interfacial reactions.

Thirdly, in Ottaviani's model it is assumed that the reaction which actually occurs is both kinetically and thermodynamically preferred (see section 2.3.4.4 and Fig. 2-16). This is not always true. In my model, it has been indicated (criterion 2) that if a reaction is kinetically preferred and thermodynamically allowed ($\Delta G < 0$), it will actually occur, i.e. this reaction does not have to be thermodynamically preferred. Using Ottaviani's model, Stage III of manganese silicide formation can not be explained because reaction (f) is thermodynamically preferred while reaction (e) is kinetically preferred (see section 5.2, Stage III). However, this stage can be explained using the proposed model and criterion 2.

From the discussion above, it can be realized that the basic principle of the suggested model and the criteria for manganese silicide formation is as follows: Only the reaction which is both thermodynamically allowed and kinetically preferred can actually occur. The composition in the reaction region will determine which reaction is kinetically preferred and will have an important influence on which reactions are thermodynamically allowed. The composition is mainly controlled by the diffusion flux of the moving reactant.

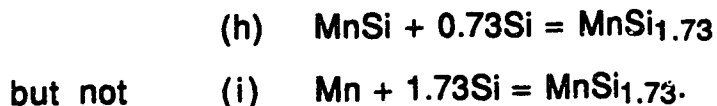
Using this principle, the difference between the formation processes of manganese silicides and that of most other silicides (i.e. single layer growth process) can be attributed to the large change (about two orders of magnitude, see section 4.4.2) in

diffusion flux of Mn in Mn/Si thin film couples used in this experiment. As for the cause of the rapid decrease of the Mn flux, there has been no experimental work conducted yet, so that the reason for the flux change is unknown at this time. However, from the discussion of impurity effects on silicide formation in section 2.3.2.4, the presence of oxygen resulted in similar phenomena (diffusion flux decrease and multiple layer growth) in Pt/Si [20, 63], Ni/Si [20], and Mo/Si [64] thin film couples. It is quite likely that oxygen exists in both the deposited Mn film and the annealing environment due to the experimental conditions. Therefore, at this time, it is reasonable to attribute the rapid flux change to impurity (mainly oxygen) effects, although further experimental work needs to be done.

5.4. Explanation for Nucleation Controlled Process

Experimental results have shown that $\text{MnSi}_{1.73}$ formed (during annealing reactions at 485 to 570°C) through an island growth process (section 4.2.3). This type of growth process may be explained by the theory of nucleation controlled processes. As discussed in section 2.3.3.2, a nucleation controlled process will occur if the activation energy, ΔG^* , for a new phase to nucleate is large and the reaction temperature is relatively low. This is the case encountered during the annealing reaction of $\text{MnSi}_{1.73}$.

From the XRD data in Table 4-4, it is obvious that before $\text{MnSi}_{1.73}$ formation, the growth of MnSi has finished. Therefore, the formation process of $\text{MnSi}_{1.73}$ is (see Fig. 4-14):



For reaction (h), the standard Gibbs free energy at 485°C has been calculated. If the data from reference [5] are used, the resulting value is 24.1 kJ/mol; and if the data from reference [83] are used, the calculated value is -12.2 kJ/mol. There exists some discrepancy between the two calculated values, which arises from the discrepancy in reported ΔH_{298}° and ΔS_{298}° values for MnSi. In either case the absolute values of ΔG° are rather small, and since the reaction actually does occur, it follows that the standard free energy for this reaction is small.

In addition, by evaluating the ratio of the molar volumes for MnSi and MnSi_{1.73} using Eq. 5-10, one can find that if reaction (h) takes place, the volume increase will be about 40 per cent.

$$\begin{aligned} & \frac{\text{Molar Volume of MnSi}_{1.73}}{\text{Molar Volume of MnSi}} & (5-10) \\ &= \frac{N_{\text{MnSi}} \times n_{1\text{Mn}}}{N_{\text{MnSi}_{1.73}} \times n_{2\text{Mn}}} \\ &= \frac{4.226 \times 10^{22} \times 1}{2.729 \times 10^{21} \times 11} \\ &\cong 1.4. \end{aligned}$$

N_{MnSi} and $N_{\text{MnSi}_{1.73}}$ are the numbers of formula units of MnSi and MnSi_{1.73} in a unit volume (formula units/cm³), respectively; $n_{1\text{Mn}}$ and $n_{2\text{Mn}}$ are the atom numbers of Mn in one formula unit of MnSi and

MnSi_{1.73} (Mn₁₁Si₁₉). As a result of the large change in volume, the value of ΔH_d (energy change due to deformation) will be relative high. According to Eq. 2-13,

$$\Delta G^* \propto \frac{\Delta \sigma^3}{(|\Delta G_o| - \Delta H_d)^2} \quad (2-13),$$

the activation energy for reaction (h) will be rather high indeed. Thus, the theory of nucleation controlled processes can explain the island growth observed in this experiment.

As for reaction (i), it is still unknown whether it also follows island growth. Because of its relatively high ΔG° value (-69.3 kJ/mol), it is expected that reaction (i) will occur through a layered growth process. Further investigation needs to be done.

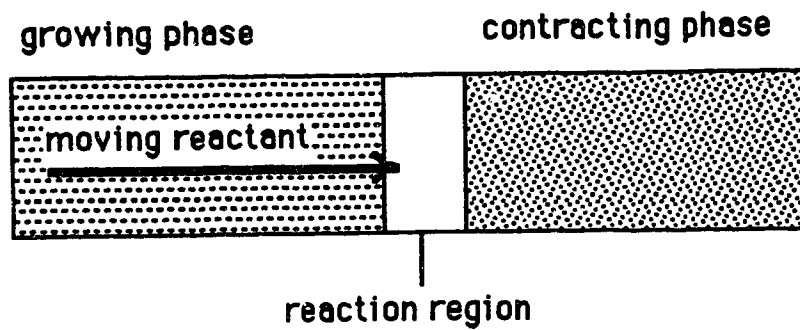


Fig. 5-1. Schematic model for manganese silicide formation. The interface region between growing phase and contracting phase is assumed to be the reaction region (not to scale). See text for the assumptions about the reaction process in this region.

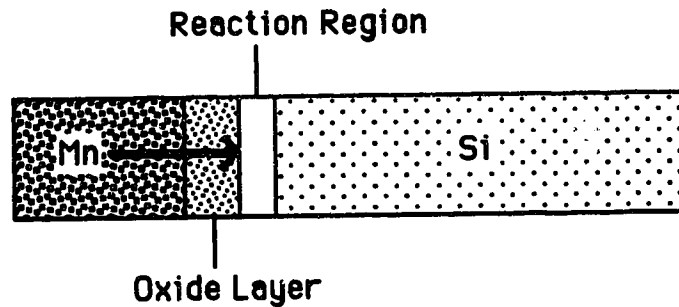
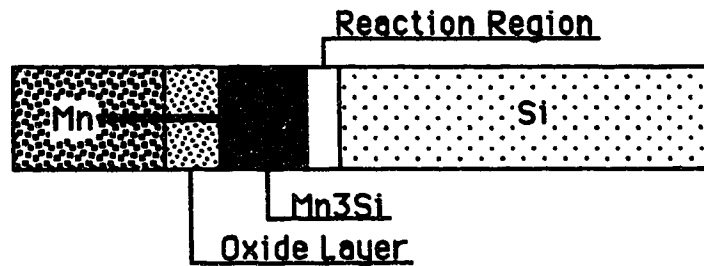
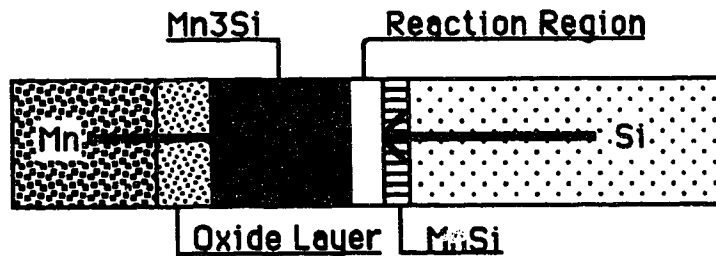


Fig. 5-2. Stage I of manganese silicide formation process (not to scale). The arrow indicates that Mn diffuses through the oxide layer to arrive at the interface between oxide and Si.

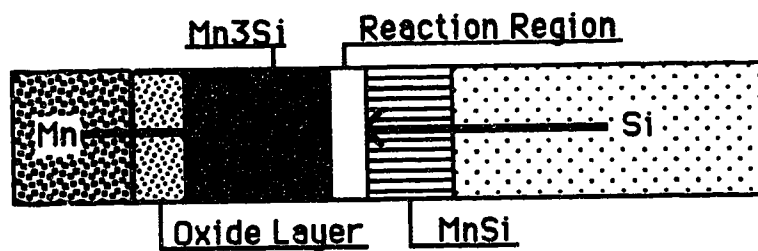


(a)

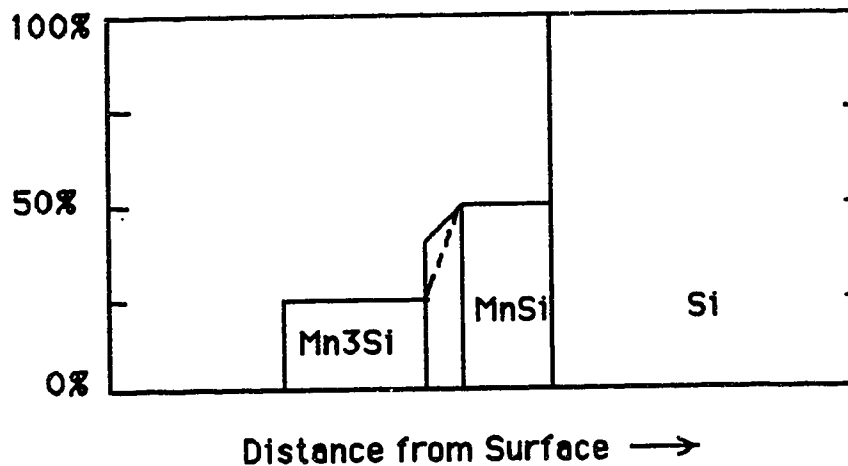


(b)

Fig. 5-3. Schematic of Stage II of manganese silicide formation process. (a) As soon as Mn_3Si forms, it is the growing phase. The arrow indicates that Mn is the moving reactant in Mn_3Si phase. (b) MnSi phase starts to grow at the interface of $\text{Mn}_3\text{Si}/\text{Si}$. The arrow from Mn layer to reaction region indicates Mn is the major diffuser in both oxide and Mn_3Si phase, while the other arrow indicates Si is the major diffuser in MnSi phase (not to scale).

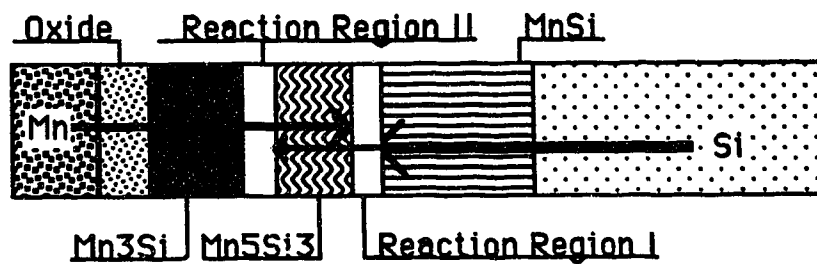


(a)



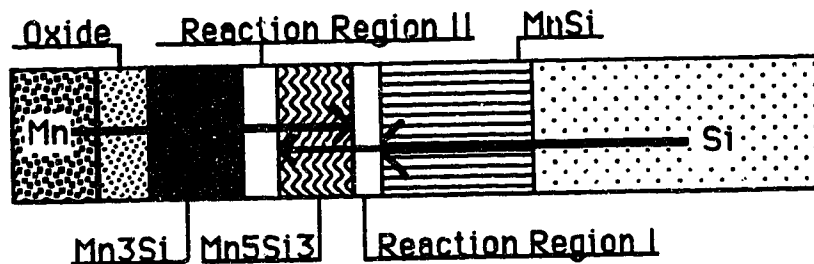
(b)

Fig. 5-4. Schematic diagram for Stage III of manganese silicide formation. (a) The beginning of Stage III. (b) Si concentration profile. The dashed line represents the Si concentration gradient without excess Si. The solid line in the reaction region indicates the Si concentration gradient when excess Si builds up in front of Mn_3Si . (see next page for Fig. 5-4c)

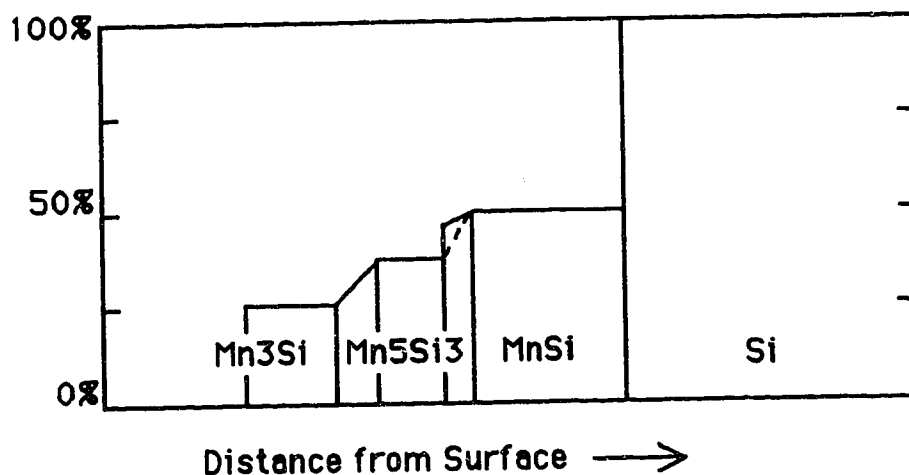


(c)

Fig. 5-4c. After Mn_5Si_3 formation, two reaction regions are separated by Mn_5Si_3 layer. The arrow from Mn towards the first reaction region indicates Mn flux, while the arrow from Si to the first reaction region represents Si flux through MnSi phase. The small arrow indicates that excess Si diffuses through Mn_5Si_3 to arrive at the second reaction region.



(a)



(b)

Fig. 5-5. Schematic diagram for Stage IV of manganese silicide formation. (a) The beginning of Stage IV. (b) Si concentration profile in samples. The dashed line in the first reaction region represents the concentration gradient just after Mn_5Si_3 formation from Mn_3Si and Si. The solid line in the first reaction region indicates Si concentration gradient when excess Si builds up in front of Mn_5Si_3 .

Chapter 6. CONCLUSIONS AND RECOMMENDATIONS

6.1. Conclusions

Manganese silicide formation by thermal reaction and the optical properties of $\text{MnSi}_{1.73}$ have been investigated. The following conclusions can be drawn from the experimental results:

1. During low temperature annealing (380°C to 430°C), three manganese silicides are formed, i.e. Mn_3Si , Mn_5Si_3 , and MnSi . During high temperature annealing (485°C to 570°C), two silicides are formed, i.e. MnSi and $\text{MnSi}_{1.73}$.

2. The silicides that form at low temperatures grow by a layered growth manner. The formation sequence for them is Mn_3Si , MnSi , and then Mn_5Si_3 . The unusual phenomena of the co-existence of these three phases has also been observed.

3. $\text{MnSi}_{1.73}$, formed at higher temperatures, grows by an island growth manner.

4. Mn is the major diffuser in the Mn_3Si phase, while Si diffusion predominates in the MnSi phase.

5. A model for manganese silicide formation has been suggested. The silicide formation sequence and the unusual phenomena can be explained by this model.

6. Island growth of $\text{MnSi}_{1.73}$ can be explained by a nucleation controlled growth process.

7. The band gap for $\text{MnSi}_{1.73}$ has been evaluated from optical property measurements. It has a value approximately between 0.78 and 0.83 eV.

6.2. Recommendations

1) In this study, a model for the formation process of manganese silicides was suggested and the model can explain the formation process (during low temperature annealing) quite well. Since there is not any restriction for the types of the components of the thin film couple in the assumptions of the model, it is possible to apply this model to other metal-Si thin film couples. Therefore, further research, to find whether the model has general applicability for other thin film systems, is recommended for further investigations.

2) In this study, the determined band gap value of $\text{MnSi}_{1.73}$ is in a narrow range (0.78 to 0.83 eV), but not an exact value. In addition, it is a little higher than that optically determined by Bost and Mahan (0.68 eV) [16]. It is noteworthy that both results determined by optical property measurements (Ref. 16 and this study) are from polycrystalline $\text{MnSi}_{1.73}$ film. At this point, it is impossible to obtain an exact value of the band gap unless optical determinations of band gap values are done on an epitaxial $\text{MnSi}_{1.73}$ thin film. Thus, research aimed at growing epitaxial $\text{MnSi}_{1.73}$ on Si is recommended.

3) From experimental observations, both by Eizenberg and Tu [6] and in this study, it is obvious that $\text{MnSi}_{1.73}$ can form only through the following reaction under the experimental conditions used in these two investigations:



Because the reaction is nucleation controlled and MnSi is polycrystalline, the MnSi_{1.73} layer that forms should have a polycrystalline structure, too. Thus it is almost impossible for MnSi_{1.73} to grow epitaxially through this process. However, epitaxial growth is still possible, due to the small difference between the lattice parameter of Si (a = 0.543 nm) and that of MnSi_{1.73} (a = 0.5525 nm, b = 1.746 nm) if the following reaction can occur, without previous formation of other manganese silicides, by a diffusion controlled process:



Therefore, it is recommended that research be conducted to try and promote the formation of MnSi_{1.73} through the above reaction, without the formation of MnSi. Also, knowledge of the reaction kinetics would be beneficial.

4) It has been noted that the unusual formation process of manganese silicide is caused by the rapid decrease of Mn flux. In section 5.3, it has also been pointed out that the change in diffusion flux of Mn was probably induced by the presence of oxygen in deposited Mn film and the annealing environment as well. Therefore, it will be helpful for us to confirm the suggested model for manganese silicide formation and the assumption about oxygen effect on Mn flux, if the deposition of Mn and the annealing process can be done in much cleaner environments. Further research, on manganese silicide formation during low temperature annealing under cleaner experimental conditions, is recommended.

BIBLIOGRAPHY

- [1] M-A Nicolet and S. S. Lau, Chap.6 in *VLSI Electronics Microstructure Science*, V6, ed. Norman G. Einsprunch and Graydon B. Larrabee (1983), Academic Press, New York, 329.
- [2] S. P. Murarka, *Silicides for VSLI Applications*, Academic Press, New York, (1983).
- [3] O. Schwomma, A. Preisinger, H. Nowotny, and A. Wittman, *Mh. Chem.*, **95**, (1964), 1527.
- [4] H. W. Knott, M. H. Mueller, and L. Heaton, *Acta Cryst.*, **23**, (1967), 549.
- [5] G. V. Samsonov and I. M. Vinitskii, in *Handbook of Refractory Compounds*, (1980), IFI/Plenum.
- [6] M. Eizenberg and K. N. Tu, *J. Appl. Phys.*, **53**, (1982), 6885.
- [7] F. A. Shunk, *Constitution of Binary Alloys, Second Supplement*, McGraw-Hill, Inc., (1969), 507.
- [8] J. D. M. Donnay and H. M. Ondik, in *Crystal Data-Determinative Table V2*, U.S. Department of Commerce, National Bureau of Standards and the Joint Committee on Powder Diffraction Standards, (1973), PT-171.
- [9] P. Villars and L. D. Calvert, *Pearson's Handbook of Crystallographic Data for Intermetallic Phases V1*, (1985), American Society for Metals, Metal Park, 471.
- [10] H. Q. Ye and S. Amelinckx, in *Modulated Structure Materials*, ed. T. Tsakalakos, (1984), Martinus Nijhoff Publishers, 173.
- [11] I. Kawasuni, M. Sakata, I. Nishida, and K. Masumoto, *J. Mater. Sci.*, **16**, (1981), 355.

- [12] I. Nishida, *J. Mater. Sci.*, **7**, (1972), 435.
- [13] Ch. Krontiras, K. Pomoni, and M. Roilos, *J. Phys. D: Appl. Phys.*, **21**, (1988), 509.
- [14] K. E. Sundstrom, S. Petersson, and F. A. Tove, *Phys. Status Solidi.*, **A20**, (1973), 653.
- [15] G. V. Samsonov, in *No.2 Properties Index*, (1964), Plenum, New York, 161.
- [16] M. C. Bost and J. E. Mahan, *J. Electr. Mater.*, **16**, (1987), 389.
- [17] C. Calandra, in *Springer Series in Materials Science-Semiconductor Silicon*, V13, ed. G. C. Harbeke and M. J. Schultz, (1989), Springer-Verlag Berlin Heidelberg, 252.
- [18] R. W. Balluffi and J. M. Blakely, *Thin Solid Films*, **25**, (1975), 363.
- [19] R. M. Walser and R. W. Bene, *Appl. Phys. Lett.*, **28**, (1976), 624.
- [20] G. Ottaviani, *J. Vac. Sci. Technol.*, **16**, (1979), 1112.
- [21] B. Y. Tsaur, S. S. Lau, J. W. Mayer, and M.-A. Nicolet, *Appl. Phys. Lett.*, **38**, (1981), 922.
- [22] K. N. Tu, *Ann. Rev. Mater. Sci.*, **15**, (1985), 147.
- [23] F. M. d'Heurle and P. Gas, *J. Mater. Res.*, **1**, (1986), 205.
- [24] G. Ottaviani, *Thin Solid Films*, **140**, (1986), 3.
- [25] K. N. Tu, Chap.7 in *Advances in Electronic Materials*, ed. B. W. Wessels and G. Y. Chin, (1986), American Society for Metals, 147.
- [26] G. Ottaviani and C. Nobili, *Thin Solid Films*, **163**, (1988), 111.
- [27] L. Borucki, R. Mann, G. Miles, J. Slinkman, and T. Sullivan, "1988 *IEEE International Electron Devices Meeting*, San Francisco, Dec. 14-16, (1988), 348.

- [28] Chang-joo Youn, Kenneth Jungling, and W. W. Grannemann, *J. Vac. Sci. Technol.*, **A6**, (1988), 2474.
- [29] Billyl Crowder and Stanley Zirinsky, *IEEE Trans. Electron. Devices*, **ED-26**, (1979), 369.
- [30] H. J. Geipe, Jr., N. Hsieh, M. H. Ishaq, C. W. Koburger, and F. R. White, *IEEE. Trans. Electron Devices*, **ED-27**, (1980), 1417.
- [31] B-Y. Tsaur, C. K. Chen, and C. H. Anderson, Jr., *J. Appl. Phys.*, **57**, (1985), 1890.
- [32] T. Paul Chow and Andrew J. Steckl, *IEEE Trans. Electron Devices*, **ED-30**, (1983), 1480.
- [33] Bing-Zong Li, Shi-Fang Zhou, Jia Li, and Ting-Ao Tang, *J. Vac. Sci. Technol.*, **B5**, (1987), 1667.
- [34] M. C. Bost and J. E. Mahan, *J. Appl. Phys.*, **58**, (1985), 2696.
- [35] M. C. Bost and J. E. Mahan, Unpublished data, (1987).
- [36] R. G. Long, M. C. Bost, and J. E. Mahan, Unpublished data, (1988).
- [37] U. Gosele and K. N. Tu, *J. Appl. Phys.*, **53**, (1982), 3252.
- [38] G. V. Kidson, *J. Nucl. Mater.*, **3**, (1961), 21.
- [39] C. Wagner, *Acta Metall.*, **17**, (1969), 99.
- [40] A. J. Hickl and R. W. Heckel, *Metall. Trans.*, **6A**, (1975), 431.
- [41] S. R. Shatynski, J. P. Hirth, and R. A. Rapp, *Acta Metall.*, **24**, (1976), 1071.
- [42] K. N. Tu and J. W. Mayer, Chap.10 in *Thin Film-Interdiffusion and Reactions*, ed. J. M. Poate, K. N. Tu, and J. W. Mayer, (1978), Wiley, New York, 359.
- [43] K. N. Tu, G. Ottaviani, U. Gosele, and H. Foll, *J. Appl. Phys.*, **54**, (1983), 758.

- [44] K. N. Tu, G. Ottaviani, R. D. Thompson, and J. W. Mayer, *J. Appl. Phys.*, **53**, (1982), 4406.
- [45] L. R. Zheng, L. S. Hung, and J. W. Mayer, *J. Vac. Sci. Technol.*, **A1**, (1983), 758.
- [46] M. Natan and S. W. Duncan, *Thin Solid Films*, **123**, (1984), 69.
- [47] M. Natan, S. W. Duncan, and N. E. Byer, *J. Appl. Phys.*, **55**, (1984), 1450.
- [48] P. A. Psaras, R. D. Thompson, S. R. Herd, and K. N. Tu, *J. Appl. Phys.*, **55**, (1984), 3536.
- [49] K. N. Tu, E. I. Alessandrini, W. K. Chu, H. Krautle, and J. W. Mayer, *Japan. J. Appl. Phys. Suppl.* **2**, Pt.1, (1974), 669.
- [50] H. Foll, P. S. Ho, and K. N. Tu, *Phil. Mag. A* **45**, (1982), 31.
- [51] R. Anton and U. Neukirch, *Appl. Surf. Sci.*, **29**, (1987), 287.
- [52] M. Del Giudice, J. J. Joyce, F. Boscherini, C. Capasso, and J. H. Weaver, *Mat. Res. Soc. Symp. Proc.*, **77**, (1987), 277.
- [53] J. H. Weaver, Chapter 2 in *Analytical Techniques for Thin Films*, ed. K. N. Tu and R. Rosenberg, (1988), Academic Press, New York.
- [54] G. Ottaviani, G. Majni, and C. Canali, *Appl. Phys.*, **18**, (1979), 285.
- [55] R. D. Thompson, and K. N. Tu, *Thin Solid Films*, **93**, (1982), 265.
- [56] R. Pretorius, W. Strydom, and J. W. Mayer, *Phys. Rev.*, **B22**, (1980), 1885.
- [57] A. P. Botha, and P. Pretorius, *Thin Solid Films*, **93**, (1982), 127.
- [58] W. K. Chu, S. S. Lau, J. W. Mayer, H. Muller, and K. N. Tu, *Thin Solid Films* **25**, (1975), 393.
- [59] T. G. Finstad, *Phys. Status. Solid.*, **A63**, (1981), 223.

- [60] M. Bartur and M.-A. Nicolet, *J. Appl. Phys.*, **54**, (1983), 5404.
- [61] J. Baglin, J. Dempsey, W. Hammer, F. d'Heurle, S. Petersson, and C. Serrano, *J. Electron. Mater.*, **8**, (1979), 641.
- [62] F. M. d'Heurle, *Thin Solid Films*, **151**, (1987), 41.
- [63] G. Ottaviani and J. W. Mayer, in *Reliability and Degradation Semiconductor Device and Circuits*, ed. M. J. Howes and D. V. Morgan, (1981) Wiley, New York, 105.
- [64] F. Nava, S. Valeri, G. Majni, A. Cembali, G. Pignatelli, and G. Queirolo, *J. Appl. Phys.*, **52**, (1981), 6641.
- [65] K. N. Tu, W. N. Hammer, and J. O. Olowolafe, *J. Appl. Phys.*, **51**, (1980) 1663.
- [66] F. Nava, S. Mantovani, G. Pignatelli, G. Queirolo, and G. Celotti, *Thin Solid Films*, **89**, (1982), 381.
- [67] M. Eizenberg and K. N. Tu, *J. Appl. Phys.*, **53**, (1982), 1577.
- [68] B. E. Deal and A. S. Grove, *J. Appl. Phys.*, **36**, (1965), 3770.
- [69] H. H. Farrell, G. H. Gilmer, and M. Suenga, *Thin Solid Films*, **25**, (1975), 253.
- [70] F. M. d'Heurle, in *Solid State Devices 1985*, ed. P. Balk and O. G. Folberth, Elsevier Science Publishing Inc., (1986), 213.
- [71] J. Lajzerowicz, Jr., J. Torres, G. Goltz, and R. Pantel, *Thin Solid Films*, **140**, (1986), 23.
- [72] G. Goltz, J. Torres, J. Lajzerowicz, Jr., and G. Bomchil, *Thin Solid Films*, **124**, (1985), 19.
- [73] E. Ma, B. S. Lim, and M.-A. Nicolet, *J. Electron. Mater.*, **17**, (1988), 207.
- [74] J. E. Baglin, F. M. d'Heurle, and C. S. Petersson, *Appl. Phys. Lett.*, **36**, (1980), 594.

- [75] R. D. Thompson, B. Y. Tsaur, and K. N. Tu, *Appl. Phys. Lett.*, **38**, (1981), 535.
- [76] J. E. E. Baglin, F. M. d'Heurle, and C. S. Petersson, *J. Appl. Phys.*, **52**, (1981), 2841.
- [77] C. S. Peterson, R. Anderson, J. E. Baglin, J. Dempsey, W. Hammer, F. M. d'Heurle, and S. J. Laplaca, *J. Appl. Phys.*, **51**, (1980), 373.
- [78] *Powder Diffraction Files* , JCPDS–International Cenetr for Diffraction Data.
- [79] D. B. Williams, Chap.4 and 6 in *Practical Analytical Electron Microscopy in Materials Science*, by D. B. Williams, (1984), Philips Electronic Instruments, Electron Optics Publishing Group, Mahwah.
- [80] M. Raghavan, J. C. Scanlon, and J. W. Steeds, *Metall. Trans.* **15A**, (1984), 1299.
- [81] R. C. Weast, *Handbook of Chemistry and Physics*, 56th Ed., CRC Press, Inc., (1975-1976).
- [82] M. J. Brett, *PhD Thesis*, University of British Columbia, (1985), 117.
- [83] T. G. Chart, *High Temp.-High Pressures*, **5**, (1973), 241.
- [84] D. G. Ivey and G. R. Piercy, *J. Electron Microscopy Technique*, **8**, (1988), 233.
- [85] J. C. Bravman and R. Sinclair, *J. Electron Microscopy Technique*, **1**, (1984), 53.
- [86] J. I. Pankove, Chap.4 in *Optical Processes in Semiconductors*, (1971), Prentice Hall, Englewood Cliffs.
- [87] A. J. Moses, *Optical Materials Properties*, by A. J. Moses, (1971), New York, IFI/Plenum, 70.

Appendix 1. X-Ray Diffraction File Cards Used to Identify Silicide Phases

A.1.1. X-Ray Diffraction File for $Mn_{15}Si_{26}$ from JCPDS Powder Diffraction File [78]

d	2.15	1.91	1.70	3.43	(Mn ₁₅ Si ₂₆) ₁₁					
I/I ₁	100	80	80	70	Manganese Silicide					
Rad. CuKα A 2.2909 Filter Dia.					d Å	I/I ₁	hkl	d Å	I/I ₁	hkl
Cut off 1/I ₁ Visual					3.43	70	1015			
Ref. Fliether et al., Monatsh. Chem., 92 2173 (1967)					2.762	40	200			
					2.284	60	2111			
					2.151	100	2115			
Sys. Tetragonal S.G. 142d (122)					2.116	50	1126			
a ₀ 5.525 b ₀ c ₀ 65.55 A C 11.864					1.952	70	220			
a β γ Z D ₂					1.940	20	224			
Ref. Ibid.					1.906	80	1130			
					1.698	80	3015			
					1.508	10	3122			
ca nwβ εγ Sign					1.445	20	3215			
2V D mp Color					1.409	35	1045			
Ref.					1.382	30	400			
					1.364	60	3135			
					1.342	50	2141			
					1.307	40	4111			
					1.282	80	4115			
					1.255	80	2145			
					1.235	90	420			
					1.232	30d	424			
Other compounds near MnSi _{1.7} have been reported as tetragonal with a near above value, but smaller values of Co. See Pearson, Vol. 2, p. 1083.										

A.1.2. X-Ray Diffraction File for Mn_5Si_3 from JCPDS Powder Diffraction File

3561 d 3-1044	2.04	2.25	1.97	3.43	Mn ₅ Si ₃					
I/I ₁ 3-1039	100	80	80	40	MANGANESE SILICIDE					
Rad. CuK α	λ 2.28962		Filter							
Dia.	Cut off		Coll.							
I/I ₁			d corr. abs.?							
Ref. AMAR, BOREN, AND WESTGREN, SVENSK KEM. TIDN. 48, 273 (1938)										
Sys. Hexagonal	S.G. D_{6h}^3 - $P6_3/mmc$									
a ₀ 6.898	b ₀	c ₀ 4.902	A	C 0.696						
a	β	γ	Z							
Ref. See ABOVE										
ts	nw β	$\epsilon\gamma$	Sign							
2V	D	mp	Color							
Ref.										
					d Å	I/I ₁	hkl	d Å	I/I ₁	hkl
					3.43	40	110	1.49	40	400
					2.98	80	200	1.45	20	113
					2.79	40	111	1.40	80	222
					2.40	60	002	1.37	20	320
					2.25	80	210	1.36	40	312
					2.22	60	102	1.32	60	321
					2.04	100	211	1.31	80	213
					1.99	60	300	1.30	60	410
					1.97	80	112	1.27	80	402
					1.87	40	202	1.20	80	004
					1.72	20	230	1.19*	60	500
					1.65	40	310	1.19	40	322
					1.62	40	221	1.17	40	223
					1.57	40	311			
					1.52	20	302			

**A.1.3. List of the Most Intense X-Ray
Diffraction Peaks for Mn₁₅Si₂₆***

d (nm)	I/I ₁	h	k	l
0.1907	100	1	1	30
0.3427	80	1	0	15
0.2118	40	1	1	26
0.2151	35	2	1	15

**A.1.4. List of the Most Intense X-Ray
Diffraction Peaks for MnSi***

d (nm)	I/I ₁	h	k	l
0.2038	100	2	1	0
0.1861	40	2	1	1
0.3223	30	1	1	0
0.2632	10	1	1	1
0.2279	10	2	0	0

* All these data were estimated from Ref. [6]

Appendix 2. Procedure for Specimen Preparation

The preparation of cross-section specimens requires considerable skill and patience. The techniques for specimen preparation have been well documented in the literature [84, 85]. The procedure used here is based on these reported techniques.

The cross-section specimens were made from slabs both from annealed samples, with silicide films on the silicon substrates, and from plain silicon wafers. The procedure listed below was followed during preparation:

- 1) An annealed sample was sectioned into rectangular slabs, 1.5 mm × 5mm. Fig. A-1a shows a schematic of a slab cut from a silicide sample. Some silicon slabs were also cut from a plain silicon wafer.

- 2) Two of the sample slabs were glued face to face using a silver loaded epoxy. These made up the centre pieces of the cross-section specimen (Fig. A-1b). Plain silicon slabs were glued to each side of the centre pieces.

- 3) The composite was fixed in a small vise and squeezed gently to produce thin glued layers that were bubble free. The vise, with the composite, was heated in a furnace at 90°C for one hour.

- 4) After curing, the composite was polished with 600 grit SiC paper down to a thickness of about 400 μm . 3mm discs were cut from the composite using a Gatan ultrasonic disc cutter. The composite disc was further polished down to a thickness less than 200 μm on 600 grit SiC.

5) One side of the disc was dimpled using a Gatan dimple grinder, with 2-4 μm diamond polishing paste, until about half of the disc thickness was removed. This side of the disc was then polished with the polishing wheel of the dimple grinder, with 1 μm diamond polishing paste, until a shiny surface was obtained.

6) The other side of the disc was dimpled until a very small hole appeared in the centre of the specimen (Fig. A-1c). This side of the disc was also polished by the same method as above. The specimen was then ready for ion milling.

7) The ion milling was conducted using an Ion Tech ion mill. After the specimen was loaded into a cold stage, the chamber was pumped down to a vacuum of 10^{-6} Torr. At the same time, liquid nitrogen was circulated through the cold stage in order to cool the specimen. The cold stage is necessary because manganese, silicon, and the silicides have different sputtering rates. Specimen cooling can minimize preferential sputtering effects, allowing electron transparent specimens to be obtained.

The sputtering was carried out using two Ar^+ ion guns working at 5 kV and 0.6 mA for one hour. The angle between the ion gun and the surface of the specimen could be altered, and the specimen was rotated during the whole process to obtain a relative large, thin, and flat foil of the desired area.

The steps from 4) to 7) were also followed during preparation of plan view TEM specimens.

Appendix 3. Derivation of Equations for Evaluating Optical Constants

A.3.1. Modification of Brett's Model [82]

Fig. A-2 schematically accounts for the energy flowing through both configurations that are used in Brett's model and in this experiment. In both cases, only first order internal reflections were taken into account. The higher order reflections are neglected. According to Brett [82], this approximation introduces a maximum absolute error of 0.003 in T (transmission) or R (reflection).

From Fig. A-2a (Brett's model, i.e. an absorbing film on a transparent substrate [82]), the expression for T and R can be built up as below:

$$\begin{aligned}
 T &= \frac{I_t}{I_o} \\
 &= \frac{I_o [\exp(-\alpha d)(1-r_d)] (1-r_1)(1-r_2)}{I_o} \\
 &= \exp(-\alpha d)(1-r_d)(1-r_1)(1-r_2) \quad (A-1).
 \end{aligned}$$

$$\begin{aligned}
 R &= \frac{I_r}{I_o} \\
 &= \frac{I_o r_o + I_o (1-r_d)^2 r_1 \exp(-2\alpha d) + I_o (1-r_d)^2 (1-r_1)^2 r_2 \exp(-2\alpha d)}{I_o}
 \end{aligned}$$

$$=r_o + \exp(-2\alpha d) \left[(1-r_o)^2 r_1 + (1-r_o)^2 (1-r_1)^2 r_2 \right] \quad (\text{A-2}).$$

I_o is the intensity of the incident light; I_t and I_r are the total transmitted intensity and total reflected intensity, respectively; α is the absorption coefficient of the absorbing thin film; d is the thickness of the film; r_o , r_1 , and r_2 are the reflectivities at each interface, as shown in Fig. A-2a.

From Fig. A-2b (the configuration used in this experiment), since the Si substrate is not completely transparent due to its relatively large thickness, the absorption of Si has been considered. Therefore, the expressions for T and R are modified:

$$\begin{aligned} T &= \frac{I_t}{I_o} \\ &= \frac{I_o \left[\exp(-\alpha d) (1-r_o) \right] \left[\exp(-\alpha_s d_s) (1-r) \right] (1-r_s)}{I_o} \\ &= \exp(-\alpha d) \exp(-\alpha_s d_s) (1-r_o) (1-r) (1-r_s) \end{aligned} \quad (\text{A-3}).$$

$$\begin{aligned} R &= \frac{I_r}{I_o} \\ &= \frac{I_o r_o + I_o (1-r_o)^2 r \exp(-2\alpha d) + I_o (1-r_o)^2 (1-r)^2 r_s \exp(-2\alpha d) \exp(-2\alpha_s d_s)}{I_o} \\ &= r_o + \exp(-2\alpha d) \left[(1-r_o)^2 r + (1-r_o)^2 (1-r)^2 r_s \exp(-2\alpha_s d_s) \right] \end{aligned} \quad (\text{A-4}).$$

I_o , I_t , and I_r have the same meaning as they do in Eq. (A-1) and (A-2); α and α_s are absorption coefficients of $MnSi_{1.73}$ and Si, separately; d and d_s are the thickness of the $MnSi_{1.73}$ film and Si substrate; r_o , r_1 , and r_2 represent the reflectivities of each interface, shown in Fig. A-2b.

A.3.2. Derivation of Equations 4-15, 4-16, and 4-17

The energy flowing, total transmission and reflection, in a system allowing multiple internal reflections are schematically shown in Fig. A-3 [86]. If the Si specimen has a reflectivity r_s , an absorption coefficient α_s , and a thickness d_s , the total transmission, T , can be expressed by the following equation [86]:

$$T = \frac{(1 - r_s)^2 \exp(-\alpha_s d_s)}{1 - r_s^2 \exp(-2\alpha_s d_s)} \quad (A-5).$$

The total reflection, R , is a sum of all multiple reflections, as shown in Fig. A-3.

$$\begin{aligned} R &= \frac{I_r}{I_o} \\ &= r_s + r_s(1 - r_s)^2 \exp(-2\alpha_s d_s) + r_s^3(1 - r_s)^2 \exp(-4\alpha_s d_s) + r_s^5(1 - r_s)^2 \exp(-6\alpha_s d_s) + \dots \\ &= r_s + (1 - r_s)^2 \left[r_s \exp(-2\alpha_s d_s) + r_s^3 \exp(-4\alpha_s d_s) + r_s^5 \exp(-6\alpha_s d_s) + \dots \right] \\ &= r_s + (1 - r_s)^2 S \end{aligned} \quad (A-6).$$

S in the last line is a sum of the power sequence i.e.

$$S = r_s \exp(-2\alpha_s d_s) + r_s^3 \exp(-4\alpha_s d_s) + r_s^5 \exp(-6\alpha_s d_s) + \dots \quad (\text{A-7}).$$

The first term is $r_s \exp(-2\alpha_s d_s)$ and the ratio is $r_s^2 \exp(-2\alpha_s d_s)$ so that the sum is

$$S = \frac{r_s \exp(-2\alpha_s d_s)}{1 - r_s^2 \exp(-2\alpha_s d_s)} \quad (\text{A-8}).$$

By inserting S into Eq. A-6, one obtains

$$R = r_s + \frac{(1 - r_s)^2 r_s \exp(-2\alpha_s d_s)}{1 - r_s^2 \exp(-2\alpha_s d_s)} \quad (\text{A-9}).$$

From Eq. A-8 and A-9, the explicit form for r_s and $\exp(-\alpha_s d_s)$ can be obtained by the following derivation:

Let $A = \exp(-\alpha_s d_s)$, then Eq. A-9 becomes

$$R = r_s + \frac{(1 - r_s)^2 r_s A^2}{1 - r_s^2 A^2} \quad (\text{A-10}).$$

so that

$$A = \sqrt{\frac{R - r_s}{R r_s^2 + r_s - 2 r_s^2}} \quad (\text{A-11}).$$

Eq. A-11 is inserted into Eq. A-5:

$$T = \frac{(1-r_s)^2 \sqrt{\frac{R-r_s}{Rr_s^2+r_s^2-2r_s^2}}}{1 - \frac{r_s^2(R-r_s)}{Rr_s^2+r_s^2-2r_s^2}} \quad (\text{A-12}).$$

From Eq. A-12, r_s can be expressed as (i.e. Eq. 4-15):

$$r_s = \frac{-(R^2-2R-1-T^2) + \sqrt{(R^2-2R-1-T^2)^2 - 4(2-R)R}}{2(2-R)} \quad (\text{A-13}).$$

In Eq. A-13, T and R can be obtained from optical measurements and r_s can be evaluated. Once r_s , R , and T are known, the extinction coefficient of Si (k_s) can be expressed by the following equation (i.e. Eq. 4-17), by combining the definition of A , Eq. A-11 and Eq. 4-10 (i.e. $\alpha = \frac{4\pi k}{\lambda}$):

$$k_s = \frac{-1}{2} \left\{ \log \left[\frac{R-r_s}{Rr_s^2+r_s^2-2r_s^2} \right] \right\} \times \frac{\lambda}{4\pi d_s} \quad (\text{A-14}).$$

The refractive index for Si (n_s) can also be solved using $r_s = \frac{(1+n_s)^2}{(1-n_s)^2}$ to obtain Eq. 4-16, since k_s is negligible in this equation:

$$n_s = \frac{1 + \sqrt{r_s}}{1 - \sqrt{r_s}} \quad (\text{A-15}).$$

The calculated results for k_s and n_s , using Eq. A-14, Eq. A-15 (i.e. Eq. 4-17 and Eq. 4-16), and R , T , and r_s , are shown in Fig. A-4a and b. The results for n_s were compared with those in the literature [87]. The difference between these two sets of data, in the range of wavelength used in this experiment, was less than 6%. As for the results of k_s , since no exact values of k_s data can be obtained from the documented results (which were published in plots [87]), no comparison can be done at this time.

Appendix 4. BASIC Program for Calculation of Optical Constants

In order to simplify the program, all the equations involved in the calculations are explicitly expressed. Therefore, the calculation steps followed are:

- 1) Input L (wavelength), R_s (measured reflection of Si), T_s (measured transmission of Si), R (measured reflection from sample with $\text{MnSi}_{1.73}$ on Si), and T (measured transmission from sample with $\text{MnSi}_{1.73}$ on Si);
- 2) Calculate r_s from Eq. A-15;
- 3) Calculate n_s from Eq. A-16;
- 4) Calculate k_s from Eq. A-17;
- 5) Calculate k using the following formula (derived from Eq. A-11);

$$k = \frac{-\lambda}{4\pi d} \log \left[\frac{T}{\exp\left(-\frac{4\pi k_s d_s}{\lambda}\right)(1-r_o)(1-r)(1-r_s)} \right] \quad (\text{A-16});$$

6) Calculate r_o from the following formulas (derived from Eq. A-12);

$$\text{let } C = \exp\left(-\frac{8\pi k d}{\lambda}\right) r + \exp\left(-\frac{8\pi(k d + k_s d_s)}{\lambda}\right) (1-r)^2 r_s \quad (\text{A-17}),$$

$$\text{then } r_o = \frac{(2C-1) \pm \sqrt{(2C-1)^2 - 4C(C-R)}}{2C} \quad (\text{A-18});$$

7) Calculate n from the following formula (derived from Eq. A-13)

$$n = \frac{2(r_o+1) \pm \sqrt{4(r_o+1)^2 - 4(1-r_o)^2(1+k^2)}}{2(1-r_o)} \quad (\text{A-19});$$

8) Calculate r using Eq. A-14 from k , n , k_s , and n_s ;

9) Repeat step 5 using new r_o and r to obtain new $k=k_1$;

10) Compare k_1 from step 9) with k from step 5). If the absolute difference between them is smaller than 0.0001, stop, otherwise repeat step 5) to step 10) using new r_o and r .

The program is listed below:

```

100 PRINT "Value of L, Tsi,Rsi,Tms,Rms"
110 INPUT L,T1,R5,T,R6
120 LET R7=SQR(R5)
125 LET R=SQR(R6)
130 LET A=R7*R7-2*R7-1-T1*T1
140 LET B2=2-R7
160 LET R8=(-A-SQR(A*A-4*B2*R7))/(2*B2)
180 LET N2=(SQR(R8)+1)/(1-SQR(R8))
200 LET A3=-.5*(LOG((R7-R8)/(R7*R8*R8+R8-2*R8*R8)))
220 LET K3=A3*L/(4*3.14159*400)
227 LET E0=(6.626E-34)*(3E+08)/(L*.0001*(1.602E-19))
230 GOSUB 530
250 LPRINT "W=";L,"Tsi=";T1,"Rsi=";R7,"Tms=";T
260 LPRINT "Rms=";R,"R0=";R0,"R1=";R1,"R2=";R2
266 LPRINT "Nsi=";N2,"Nms=";N,"Ksi=";K3,"Kms=";K1
267 LPRINT "AXsi=";A3,"SQ(Ams)=";A4,"E=";E0
270 END
530 LET D1=.55
540 LET R2=((N2-1)^2+K3*K3)/((N2+1)^2+K3*K3)
550 LET A1=EXP(-A3)
560 LET R0=R
570 LET R1=0
580 LET B=LOG(T/(A1*(1-R0)*(1-R1)*(1-R2)))
590 LET K=-L*B/(4*3.14159*D1)
600 LET C=EXP(-8*3.14159*K*D1/L)
610 LET D=C*(R1+R2*(1-R1)^2*A1^2)
620 LET R3=(-(1-2*D)+SQR((1-2*D)^2-4*D*(D-R)))/(2*D)
630 LET N=(2*(1+R3)+SQR(4*(1+R3)^2-4*(1-R3)^2*(1+K*K)))/(2*(1-R3))
640 IF N>1 GOTO 660
650 LET N=(2*(1+R3)-SQR(4*(1+R3)^2-4*(1-R3)^2*(1+K*K)))/(2*(1-R3))
660 LET R4=((N-N2)^2+(K-K3)^2)/((N+N2)^2+(K+K3)^2)
670 LET B1=LOG(T/(A1*(1-R3)*(1-R4)*(1-R2)))
680 LET K1=-(L*B1)/(4*3.14159*D1)
690 IF ABS(K1-K)<.00001 GOTO 730
700 LET R0=R3
710 LET R1=R4
720 GOTO 580
730 LET A2=4*3.14159*K1/(L*.0001)
740 LET A4=A2*A2
750 RETURN

```

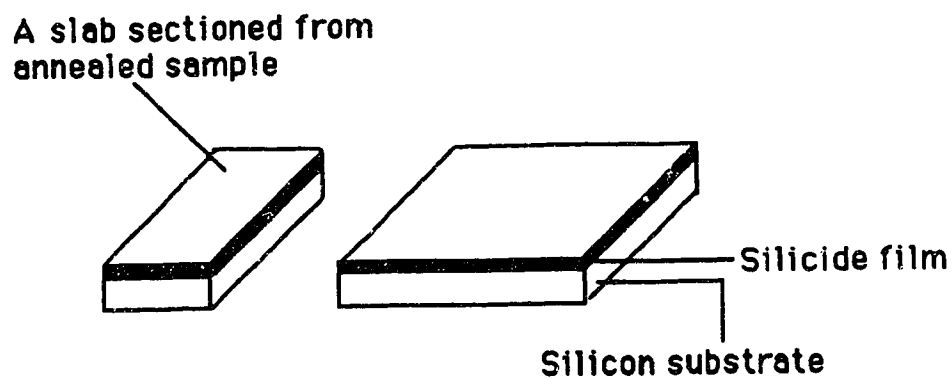


Fig. A-1a. Schematic showing a slab cut from an annealed sample. The thicknesses for both the silicide film and Si substrate are not to scale.

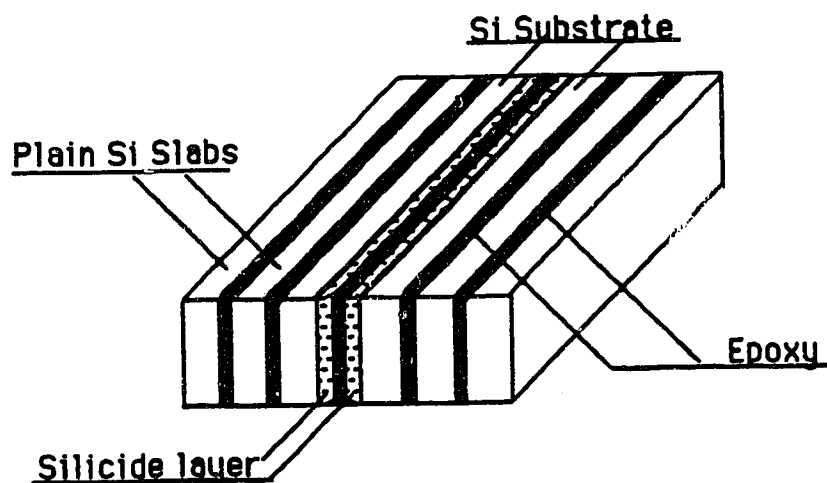


Fig. A-1b. Composite of specimen slabs, plain Si slabs, and epoxy. The dimensions are not to scale.

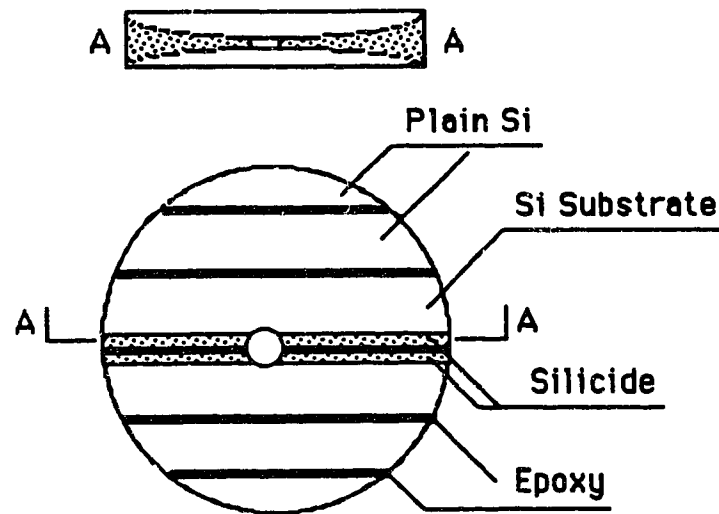


Fig. A-1c. Schematic showing the dimpled and polished composite disc (not to scale).

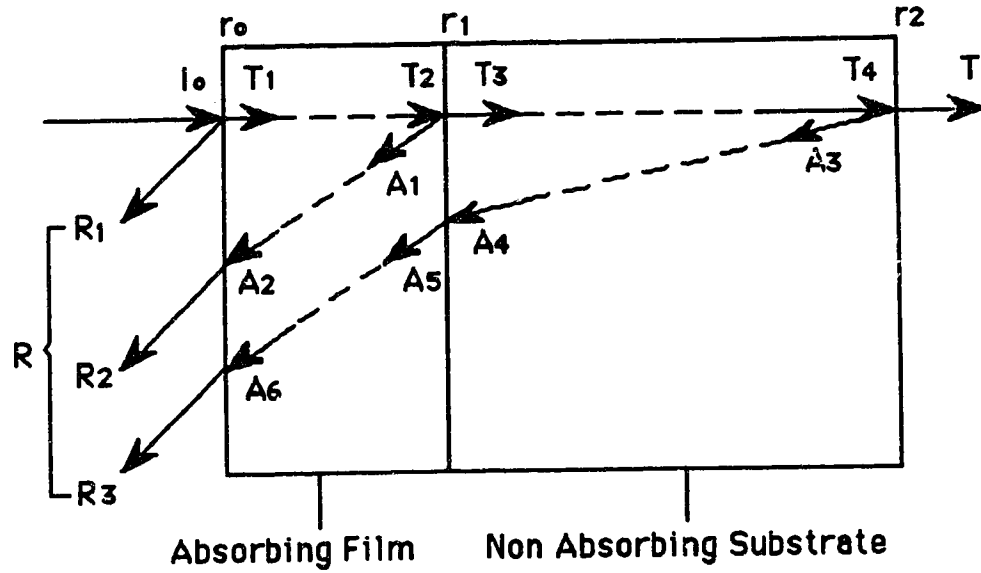


Fig. A-2a. Schematic accounting for energy flow in Brett's model. I_0 is intensity of incident light. T_i , A_i , and R_i represent the light energies as follows:

$$\begin{aligned}
 T_1 &= (1-r_0)I_0, & T_2 &= \exp(-\alpha d)(1-r_0)I_0, \\
 T_3 &= T_4 = \exp(-\alpha d)(1-r_0)(1-r_1)I_0, \\
 A_1 &= \exp(-\alpha d)(1-r_0)r_1I_0, & A_2 &= \exp(-2\alpha d)(1-r_0)r_1I_0, \\
 A_3 &= \exp(-\alpha d)(1-r_0)(1-r_1)r_2I_0, & A_4 &= \exp(-\alpha d)(1-r_0)(1-r_1)r_2I_0, \\
 A_5 &= \exp(-\alpha d)(1-r_0)(1-r_1)^2r_2I_0, & A_6 &= \exp(-2\alpha d)(1-r_0)(1-r_1)^2r_2I_0, \\
 R_1 &= r_0I_0, & R_2 &= A_2(1-r_0) = \exp(-2\alpha d)(1-r_0)^2r_1I_0, \\
 R_3 &= A_6(1-r_0) = \exp(-2\alpha d)(1-r_0)^2(1-r_1)^2r_2I_0,
 \end{aligned}$$

From the figure and the expressions of T_i , A_i , and R_i , as well as the definition of transmission and reflection, one obtains

$$\begin{aligned}
 T &= T_4(1-r_2)/I_0 = \exp(-\alpha d)(1-r_0)(1-r_1) \\
 R &= (R_1 + R_2 + R_3)/I_0
 \end{aligned}$$

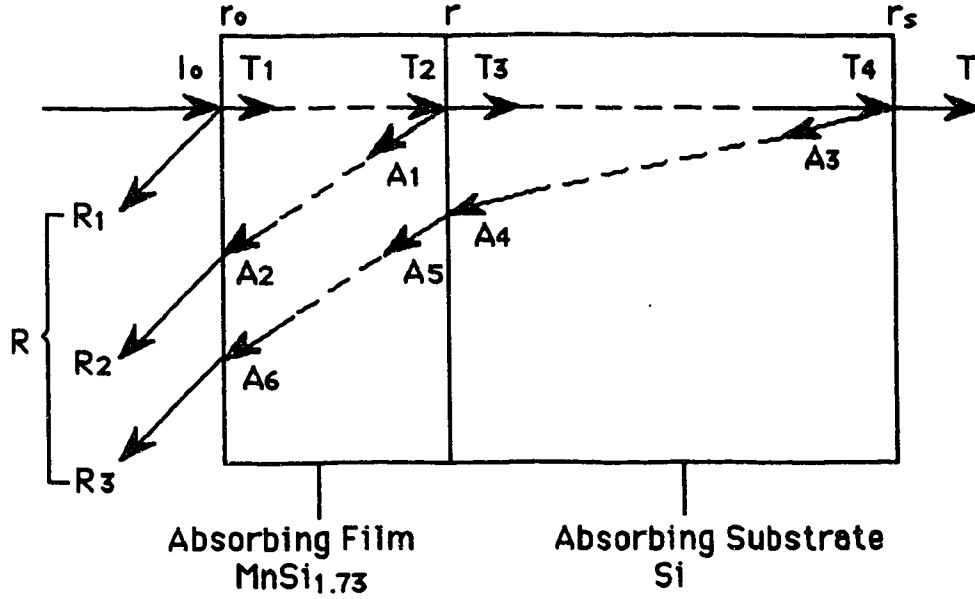


Fig. A-2b. Schematic accounting for energy flow in $\text{MnSi}_{1.73}/\text{Si}$ system. I_0 is intensity of incident light. T_i , A_i , and R_i represent the light energies as follows:

$$\begin{aligned}
 T_1 &= (1-r_0)I_0, & T_2 &= \exp(-\alpha d)(1-r_0)I_0, \\
 T_3 &= \exp(-\alpha d)(1-r_0)(1-r)I_0, & T_4 &= \exp(-\alpha d)\exp(-\alpha_s d_s)(1-r_0)(1-r)I_0 \\
 A_1 &= \exp(-\alpha d)(1-r_0)rI_0, & A_2 &= \exp(-2\alpha d)(1-r_0)rI_0, \\
 A_3 &= \exp(-\alpha d)\exp(-\alpha_s d_s)(1-r_0)(1-r)r_s I_0, \\
 A_4 &= \exp(-\alpha d)\exp(-2\alpha_s d_s)(1-r_0)(1-r)r_s I_0, \\
 A_5 &= \exp(-\alpha d)\exp(-2\alpha_s d_s)(1-r_0)(1-r)^2 r_s I_0, \\
 A_6 &= \exp(-2\alpha d)\exp(-2\alpha_s d_s)(1-r_0)(1-r)^2 r_s I_0, \\
 R_1 &= r_0 I_0, \\
 R_2 &= A_2(1-r_0) = \exp(-2\alpha d)(1-r_0)^2 r I_0, \\
 R_3 &= A_6(1-r_0) = \exp(-2\alpha d)\exp(-2\alpha_s d_s)(1-r_0)^2(1-r)^2 r_s I_0.
 \end{aligned}$$

From the figure and the expressions of T_i , A_i , and R_i , as well as the definition of transmission and reflection, one obtains

$$\begin{aligned}
 T &= T_4(1-r_s)/I_0 = \exp(-\alpha d)\exp(-\alpha_s d_s)(1-r_0)(1-r)(1-r_s) \\
 R &= (R_1 + R_2 + R_3)/I_0 \\
 &= r_0 + \exp(-2\alpha d)(1-r_0)^2 r + \exp(-2\alpha d)\exp(-2\alpha_s d_s)(1-r_0)^2(1-r)^2 r_s \\
 &= r_0 + \exp(-2\alpha d)\{(1-r_0)^2 r + \exp(-2\alpha_s d_s)(1-r_0)^2(1-r)^2 r_s\}.
 \end{aligned}$$

Figs. A-3 has been removed due to copyright restriction. Please refer to the literature [86].

Fig. A-3. Accounting of energy flow when multiple reflection takes place in a Si wafer [86].

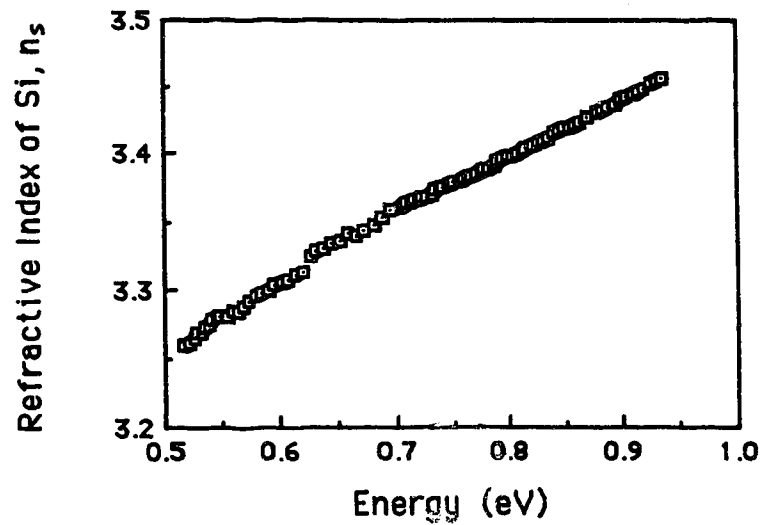


Fig. A-4a. Plot of refractive index of <100> oriented single crystal Si wafer vs. photon energy.

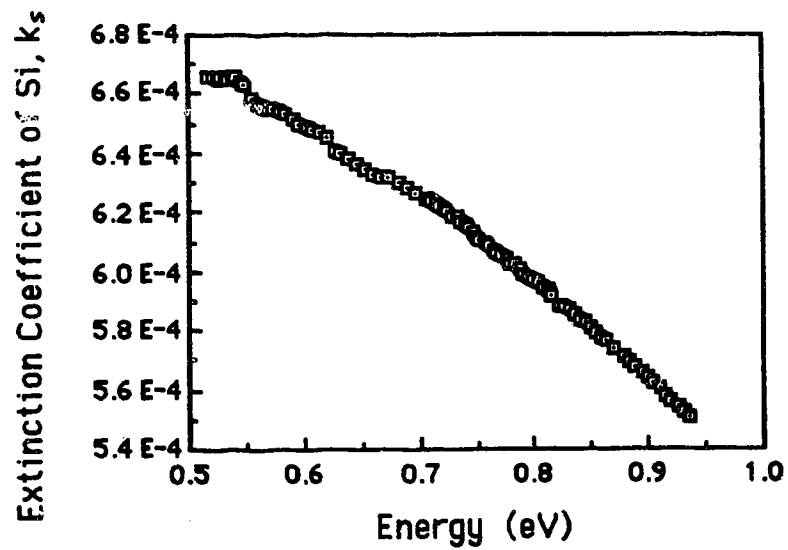


Fig. A-4b. Plot of extinction coefficient of <100> oriented single crystal Si wafer vs. photon energy.